NUCLEATION AND GROWTH OF HETEROEPITAXIAL DIAMOND

By

Connie Rebecca Bednarski-Meinke

A DISSERTATION

Submitted to
Michigan State University
in partial fulfillment of the requirements
for the degree of

DOCTOR OF PHILOSOPHY

Department of Physics and Astronomy

2002

ABSTRACT

NUCLEATION AND GROWTH OF HETEROEPITAXIAL DIAMOND

By

Connie Rebecca Bednarski-Meinke

This thesis describes the growth of single crystal diamond by low-pressure microwave plasma-enhanced chemical vapor deposition (CVD). Although diamond in the form of polycrystalline thin films has been deposited by CVD methods in the past, it has proven difficult to devise methods that induce the diamond crystallites to align and to coalesce into a single crystal. The method adopted here is based on heteroepitaxy, the single crystal growth of a desired material on a chemically distinct substrate. Two heteroepitaxial steps, carried out in sequence, were required. Epitaxial films of metallic iridium (Ir) metal were grown on lattice-matched single crystal oxides, principally $SrTiO_3$ and α-Al_2O_3 (sapphire). Heteroepitaxial diamond was then grown on Ir, which provides a good match to the lattice parameter of diamond and is resistant to the high temperature methane-hydrogen plasma.

Since diamond does not nucleate spontaneously at high densities, methods were used to stimulate its nucleation on Ir. Low-energy ions, attracted to the substrate from the plasma by a voltage bias, produced conditions favorable for diamond nucleation with densities approaching 10^{12} cm^{-2} across the entire substrate. By terminating the biasing at a series of time intervals, the sample temperature was quenched and the evolution of diamond film formation could be followed. Scanning electron microscopy was used to

image individual diamond nuclei and crystallites, their pattern formation, and coalescence on scales from 10 nm to 10 μm.

After 60 minutes of growth, extremely smooth, continuous films of single crystal diamond were obtained with dimensions the size of the substrate growth region, an area 3.5 mm in dia. By growing for extended periods, to a maximum of 48 hr, diamond plates of thickness 35 μm were produced. Freestanding crystals exhibited (111) cleavage surfaces, the same as natural diamond, and were transparent in visible light. Characterization of the material by x-ray diffraction, electron backscattering diffraction, and Raman scattering confirmed the presence of (001) oriented single crystal diamond.

By optimizing the CVD reactor geometry, this research has led to the highest density of oriented nuclei yet reported. Coalescence therefore occurs at an early stage, leading to greatly improved crystalline perfection and homogeneity. The discovery that sapphire can be used as a substrate to grow (001) epitaxial Ir and diamond promises to lead to improvements in diamond quality. Sapphire has high thermal stability coupled with remarkably good crystalline perfection, and is available as large area substrates.

This thesis encompasses studies of substrates, epitaxial growth of electron-beam evaporated Ir, systematic optimization of biasing procedures, exploration of the vast parameter space of the CVD reactor, description of characterization tools, and the results of more than 300 diamond growth experiments. Some new ideas, presented as a model of diamond nucleation and early growth, may help explain the major improvements obtained here.

To my parents, Daniel and Reinhild Bednarski

In memory of Opa

ACKNOWLEDGMENTS

I am grateful to my advisor, Brage Golding, for the opportunity to work on this project, and learn what it takes to do real science. His patience and enthusiasm helped me to focus on a sometimes murky road. I am indebted to our postdocs, Zhongning Dai and An-Ping Li. Zhongning spent long hours working on the iridium deposition, key to the success of the diamond films. An-Ping did much of the Raman and EBSD analysis. Our group shared every frustration and triumph equally.

I learned that no project of this scope is possible without the aid of knowledgeable people. Baokang Bi, competent in many techniques, was an invaluable source of information and encouragement. Reza Loloee helped with EBSD analysis, and encouraged me in my writing and presentations. A. Refik Kortan is thanked for his excellent x-ray diffraction work. Professor Jes Asmussen helped in the critical early stages of the project. Brian Wright taught me how to run a CVD system, and the finer points of university politics. The "machine shop guys": Tom Palazzolo, Jim Muns and Tom Hudson cannot be thanked enough for their patience in getting a job done just right, on a tight schedule, with a willingness to work with whatever material we needed. Ann Kirchmeier and Darla Conley were a great help in ordering those materials and tracking things down, as well as giving an encouraging word.

My labmates, Ryan Kruse and Mahdokht Behravan, set excellent examples of hard work and focus. Ryan is thanked for sitting through countless lunchtime diamond discussions, and his help and enthusiasm with the Fourier analysis. Mahdokht, one of few who truly understood the difficulty of this project in all aspects, is thanked for her

unending supply of encouragement and positive feedback. I also want to thank Lowell McCann for teaching me valuable lab techniques, and useful discussions.

Finally, I never would have attempted a Ph.D. without the love and support of my family. My sister, Melinda, never doubted I could do it, and was never shy of telling me so. My parents have been behind me the entire way, and my brothers, Dan and Michael, warmed a competitive streak in me early on. My husband, Jan, my rock and my shoulder, was with me at every step.

Table of Contents

List of Tables

List of Figures

Chapter 1 Introduction

Heteroepitaxial growth of advanced electronic materials depends on the development of suitable lattice-matched substrate systems. Diamond is of particular interest since, as a wide bandgap semiconductor, it may prove advantageous in devices. Progress in diamond heteroepitaxy was instigated by the growth of highly-oriented crystallites of diamond on silicon, despite the existence of a large lattice parameter mismatch *(1-3)*. A significant advance occurred with the discovery that epitaxial iridium films, grown as a buffer layer on magnesium oxide (MgO), could serve as a substrate for the nucleation and growth of chemical vapor deposition (CVD) diamond *(4-6)*. With a lattice parameter 7.5% larger than diamond, Ir appears to have the requisite long-term chemical and physical stability in the high-temperature environment of the CVD hydrogen plasma. Recently, the use of strontium titanate ($SrTiO_3$) as a replacement for MgO has proven useful in decreasing the mosaic spread of the epitaxial Ir and the resultant heteroepitaxial diamond *(7, 8)*.

In parallel with heteroepitaxial growth efforts, the conditions for achieving high diamond nucleation densities on various substrates have been extensively examined. The bias-enhanced nucleation process *(9)*, in which a negative voltage applied to the substrate results in its bombardment by low-energy positive ions extracted from the plasma, is a key step for inducing the formation of diamond nuclei. It is important that the nuclei

adopt the underlying orientation of the substrate and that their density be maximized, so as to lead to rapid coalescence of crystallites during the early stages of growth. Although the conditions that lead to effective nucleation are well known in principle, there is little agreement on the physical mechanisms that underlie the process. The process is also system-specific to some degree, depending on details of reactor geometry and a multitude of processing parameters.

This thesis details the results of a series of investigations of nucleation and growth of CVD diamond grown on epitaxial Ir with a (001) oriented surface. The oxide substrates utilized for Ir growth included (100)$SrTiO_3$ and $(11\bar{2}0)\,Al_2O_3$, although (100)MgO and (100)$LaAlO_3$ were also studied. Prior to Ir deposition, special emphasis was placed on the preparation and characterization of the low-index substrate surfaces. A bias-assisted step was developed and optimized to produce high densities, of order 10^{12} cm^{-2} across the Ir surface, irrespective of the underlying oxide substrate. High nucleation densities resulted in growth of (001) single crystal diamond films exhibiting homogeneity on a scale of mm.

In the course of the investigation, a significant advance was made in observing the very early stages of growth of epitaxial diamond. This will lead to an understanding of the mechanisms behind single crystal growth and nucleation as they apply to diamond as well as other lattice mismatched systems. This in turn will lead to the realization of superior materials properties of diamond.

The outline of this thesis is as follows:

Chapter 2 covers the crystal structure and bonding of diamond as well as the analytical tools used for studying iridium and diamond films. Chapter 3 provides a

background for understanding nucleation and growth of diamond. Microwave plasma CVD is described, as well as basic properties of glow discharge plasmas. Chapter 4 reviews the current status of diamond heteroepitaxy, and places the present work in the context of previous investigations. Chapter 5 describes the biased-enhanced nucleation method for diamond, and the physical mechanisms that lead to nucleation. The "secondary plasma" is discussed and its role in creating conditions for enhanced nucleation. Chapter 6 describes our methods for substrate preparation and epitaxial Ir with results for $SrTiO_3$ and a-plane Al_2O_3 substrates. Chapter 7 discusses the microwave CVD reactor configuration and procedures used to grow heteroepitaxial diamond on Ir. Chapter 8 describes our nucleation results, showing the relationship to bias current density, and provides a rationale for our high nucleation densities. We also present a model for the nucleation and early growth of heteroepitaxial diamond. Chapter 9 presents results of diamond growth, characterization of thick diamond films, and a comparison with previous reports. Chapter 10 summarizes the major findings and makes suggestions for further work.

Chapter 2 Diamond: structural properties and characterization methods

2.1 Diamond crystal structure

The diamond crystal structure is face-centered cubic (FCC) with lattice parameter a_0=0.3567 nm with a (0,0,0) and (1/4,1/4,1/4) basis, Figure 1. It can be viewed as two superimposed FCC lattices, one displaced by $a_0/4$ along the body diagonal of the other (Figure 2). It belongs to the space group Fd3m.[1]

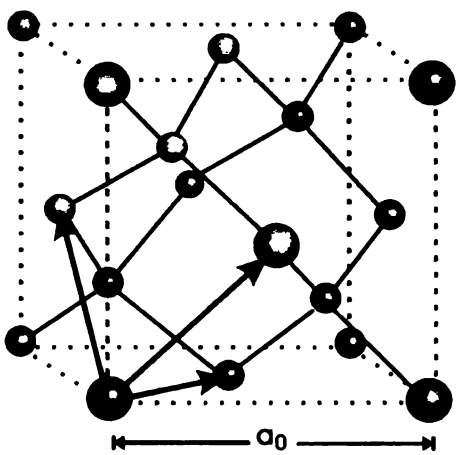

Figure 1 Diamond lattice structure. The arrows show the primitive translation vectors. Nearest neighbor bonds are shown by the solid lines with bond length 0.154 nm. a_0=0.3567 nm

[1] Space groups: The combination of all available symmetry operations that generate space-filling periodic lattices. There are 230 total space groups. Fd3m is a cubic space group. *(10)*

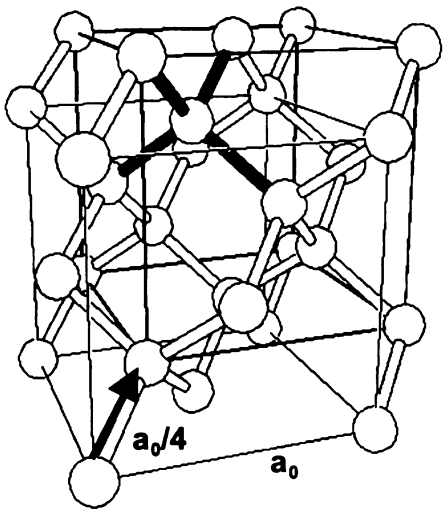

Figure 2 Diamond structure as two superimposed FCC lattices displaced by $a_0/4$ along the body diagonal. Dark lines show tetrahedral bonding.

2.2 Carbon bonding in diamond leads to unique properties

Carbon is a group IV element and in the diamond form is the prototypical and eponymous structure for silicon, germanium and gray tin. Its four valence electrons hybridize to form tetrahedral sp^3 bonds with a C-C interatomic distance of 0.154 nm. With the exception of the sp^2 C-C bond, with 0.142 nm e.g., the basal plane of graphite, it has the shortest bond of any known element, resulting in a highly compact and rigid three-dimensional crystal.

The electronic band structure of diamond is somewhat similar to silicon. The conduction band minima occur along the six <100> directions near, but not at, the edge of the Brillouin zone. Thus, diamond is an indirect band gap material. Whereas silicon and germanium have bandgaps of 1.12 eV and 0.67 eV respectively, the gap for diamond is 5.5 eV. This can be compared to other wide bandgap semiconductors, such as IV-IV silicon carbide (2.9 eV) and III-V gallium nitride (3.4 eV). The strong sp^3 bonding and

the short bond lengths in diamond lead directly to the large bandgap. Although the indirect bandgap does not allow strong band to band luminescence, the unusual physical properties of diamond (high thermal conductivity, hardness, high carrier mobility and breakdown voltage) have made it extremely attractive as a potential replacement for silicon in specific electronic applications.

Diamond has few carriers excited into the conduction band, even at relatively high temperatures, due to its wide bandgap. At temperatures as low as 200° C, intrinsic carrier levels in silicon, rather than dopant levels, begin to dominate the conductivity. Furthermore, silicon devices typically fail by high temperature degradation due to electric field induced diffusion. For these reasons, as well as its high thermal conductivity, diamond is viewed as an attractive material to realize high temperature and high frequency devices.

The wide bandgap and strong covalent bonding of diamond also contribute to another unusual property: negative electron affinity (NEA) of the hydrogen-terminated diamond surface *(11)*. NEA implies that the energy of the lowest conduction band state (conduction band minimum) lies above the vacuum level, i.e., the continuum of unbound electron states outside the semiconductor. Therefore, the electrons at the surface can, in principle, easily escape into the vacuum, an attractive property for an electron emitter. Presently, difficulties exist in realizing this idealized picture for diamond. For example, attempts to introduce significant amounts of donors (electrons) into diamond have been somewhat unsuccessful, although acceptor doping with boron leads to a level 0.38 eV above the valence band maximum. Finding suitable substitutional dopants is difficult in diamond because incorporating foreign atoms into the dense diamond lattice introduces

large strain. This, in turn, may lead to dopant energy levels that lie deep in the energy gap, far from the band extrema.

2.3 Epitaxial film structural analysis tools

The methods and equipment used to analyze the iridium and diamond films produced in this investigation are:

1. Scanning Electron Microscopy – This method yields 2-D images of the surfaces of films at scales from mm to 10 nm. This allows rapid visualization of the microstructure of the films. We use SEM for initial analysis of grain coalescence, measuring film thickness, determining cleavage planes, nucleation sites and densities, and combined with EBSD for crystal orientation determination.
2. Raman Spectroscopy – Analysis of high-energy vibrational modes provides "chemical" information, principally on the C-C bond type, and the effect of stress.
3. X-ray Diffraction – Yields basic structural information of the films, and the influence of stress.
4. Atomic Force Microscopy – Produces topographic scans of surfaces with a lateral scale of a few μm, but a vertical scale as small as 0.1 nm. Combined with SEM, AFM can distinguish between topographic and other constrast mechanisms.

These techniques are explained in more detail below. In addition, we used optical microscopy with Normarski differential interference contrast (DIC) to characterize diamond, iridium, and oxide substrates at length scales >10 μm.

2.3.1 Scanning electron microscopy

A scanning electron microscope forms an image of a sample surface using a beam of electrons swept across the surface of a solid sample in a raster pattern. The electron beam is focused with a system of electromagnetic lenses and a pair of magnetic scan coils control the position of the beam. A schematic of a SEM is shown in Figure 3.

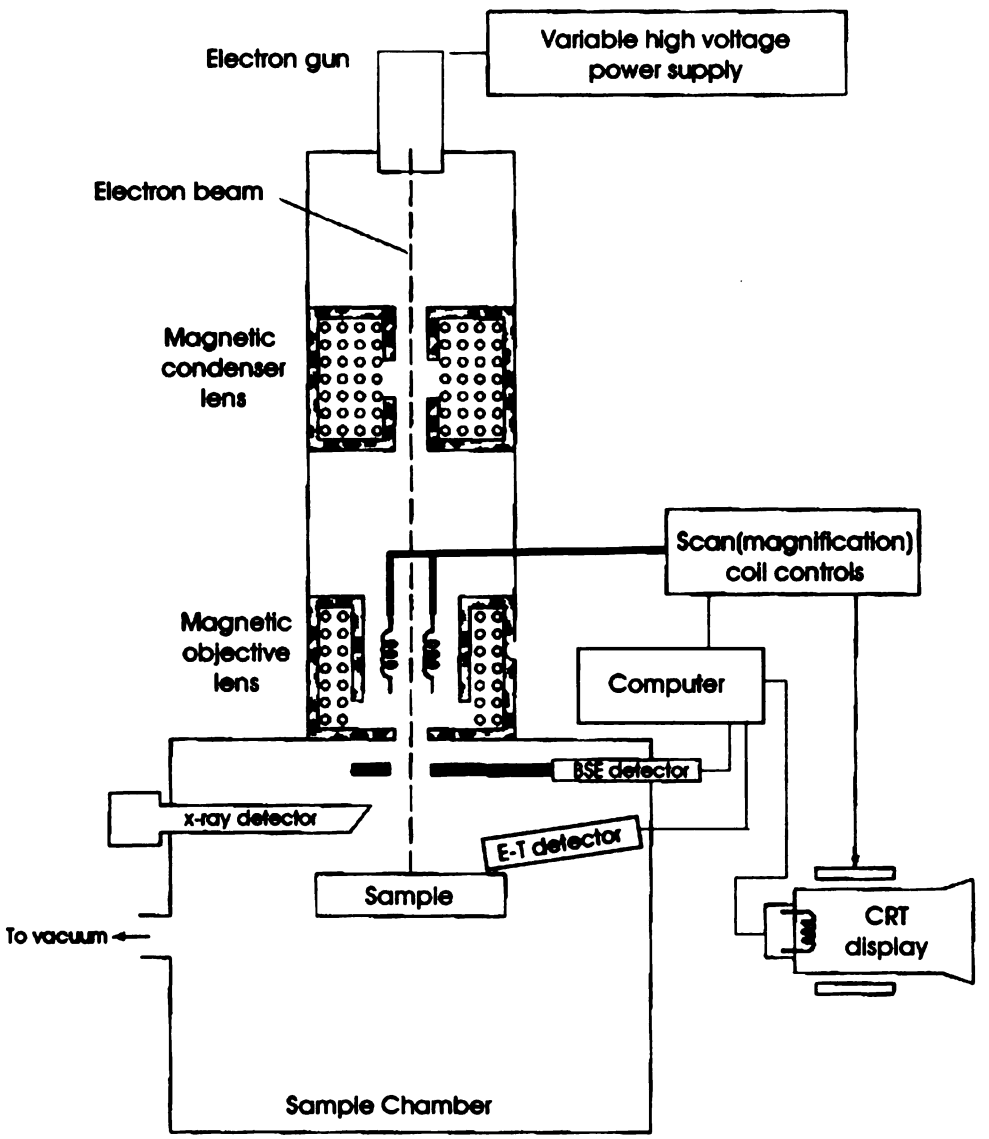

Figure 3 Schematic of a scanning electron microscope.

The Hitachi 4700 II Field Emission microscope (FESEM) used for the imaging work in this thesis has a cold field emission source as opposed to a hot thermionic one found in standard SEMs. The gun is a tungsten cathode shaped to a very sharp point of <100 nm radius. The tip is held at a high potential, so the electric field at the tip is $>10^7$ V/cm. This allows the electrons at the Fermi level to penetrate the potential barrier by tunneling, rather than thermionic emission, giving a field emission source a beam crossover diameter of 10 nm compared to 10 μm for thermionic guns used in conventional SEMs. A FESEM requires less magnetoptics to demagnify the beam before it reaches the sample, allowing for greater beam brightness, and sharper resolution. The Hitachi 4700 II FESEM has three electromagnetic objective lenses that can focus the beam to achieve a maximum resolution of 1.5 nm at an acceleration voltage of 15 kV under ideal conditions.

Electron-solid interactions produce a large number of particles and photons. The most important of these are: Secondary electrons (SE), backscattered electrons (BSE), Auger electrons (AE) and characteristic x-rays *(12)*. The penetration depth and origin of these are represented in Figure 4.

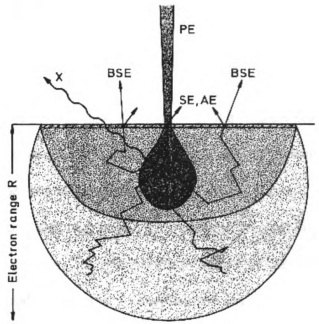

Figure 4 Penetration depth of various electrons and photons produced by electron beam interaction with the sample. PE is the incident electron beam. R~10^2 nm, but is dependent on the incident electron beam energy as well as the nature of the material.

For imaging with the SEM, the most important of these are the secondary electrons and the backscattered electrons *(12, 13)*. With incident beam energies ~10 keV, secondary electrons have energies <50 eV sharply peaked at 3-5 eV that are produced by inelastic scattering from weakly bound conduction electrons in the solid. They are detected using a positively biased collector grid that accelerates them into a scintillator and they are emitted as photons, recorded by a photomultiplier. The device is called an Everhart-Thornley detector. The number of secondary electrons depends on the sample tilt angle. Enhanced emission comes from edges and small particles. This allows the sample topography image to be formed. The signal that rasters the electron beam across the sample also scans a beam across a CRT. The output of the E-T detector modulates

the intensity of the spot on the CRT, producing an image map. The magnification M of the SEM image is:

$$M = W / w$$

where W is the width of the CRT and w is the width of a single x-scan across the sample. The Hitachi 4700 II has two SE detectors, one placed above the sample near the last objective lens, the other at a low angle with respect to the sample.

BSE are electrons that exit the sample after undergoing multiple elastic and inelastic collisions at large angles. BSE have a broad energy spectrum between 50eV and E=eU and may also produce secondary and Auger electrons as they propagate through the sample. BSE move in linear trajectories that are not affected by the Everhart-Thornley detector because of their high energies. They are instead detected with a semiconductor detector that gives a signal proportional to the BSE energy. BSE images have a lower resolution than SE images due to the larger volume of interaction. However the contrast mechanism for imaging back-scattered electrons is sensitive to the atomic number (Z) of the sample. With a wide-angle detector below the objective lens where only BSE with high take-off angles are detected, image contrast is produced mostly by Z-differences, and topographic contributions are suppressed.

2.3.2 Electron backscatter diffraction (EBSD)

Backscattered electron yield is also dependent on the sample crystallographic orientation. For a crystalline surface, BSE that are scattered at low angles with respect to the sample surface will be scattered according to the Bragg condition. Electron backscatter patterns (EBSP) are formed when the BSE from a crystal undergo diffraction

as they re-emerge from the surface *(14)*. Instead of Bragg spots, the diffracted electrons emerge in a pattern of lines called Kikuchi bands[2].

For EBSD analysis, we mount the samples in a CamScan 44FE SEM at a tilt angle of 70° with respect to an incident 25 keV electron beam. The backscattered electrons are detected on a fluorescent screen mounted in the vacuum chamber producing the Kikuchi pattern. A high gain CamScan Ortex CCD camera transmits the image from the screen to a computer via a video digitizing board. The diffraction image is analyzed using the Channel4 software package[3] to index the pattern and obtain the orientation of the crystal lattice. The sample stage is translated, or scanned, by computer-controlled movement of the stage in the SEM to obtain a spatial-orientation map of the sample.

A pole figure may be obtained from the series of point-by-point orientation measurements. A pole figure, a standard measure of the texture of a polycrystalline sample, is a plot that shows the density distribution of orientations for a selected set of crystal planes as a stereographic projection *(14)*.

2.3.3 Raman spectroscopy

Raman spectroscopy is frequently used for characterizing diamond and other carbon films *(15-17)*. The Raman effect is the inelastic light scattering from internal excitations, phonons here. Incident light of energy $\hbar\omega$ is scattered by a polarizable sample. This process causes a frequency shift in the scattered light of $\omega = \omega' \pm \frac{\Delta E}{\hbar}$, where ΔE corresponds to the phonon energy – the so-called Raman shift. In a Raman

[2] The Bragg condition is fulfilled for all directions of incidence where the wave vector **k** lies on a Kossel cone.
[3] HKL Technology, 1997.

spectrometer, the scattered light is dispersed by a grating, which allows peaks in the spectrum to be resolved, and assigned to vibrational modes of the crystal *(18)*.

In crystals, Raman selection rules allow only near zone-center optic vibrational modes to participate in first-order Raman scattering[4] *(19)*. For diamond, the characteristic first order peak that corresponds to the temperature dependent C-C stretching mode appears at 1332 cm^{-1} with a linewidth of 1-2 cm^{-1} *(15, 20-22)*. The intensity of the Raman peak depends on a Raman tensor derived from the crystal symmetry and the polarization directions of the incident and scattered light. For diamond (point group O_h) oriented in the <001> direction, the Raman line in the (001) backscattering geometry (Figure 5) is a function of the azimuthal angle of the incident light polarization $\vec{e}_i$ relative to the crystallographic axes.

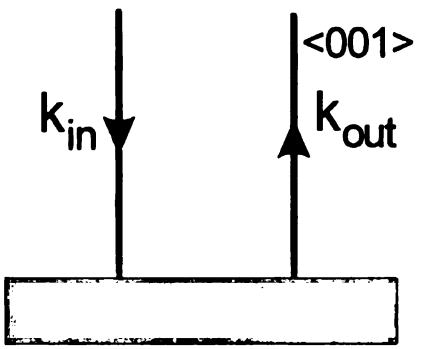

Figure 5 Raman scattering geometry. For a (001) crystal surface in the backscattering geometry, the incident, $\vec{k}_{in}$, and scattered, $\vec{k}_{out}$, wavevectors are in the <001> direction. $\vec{k}_{out}$ is polarized according to the Raman selection rules for O_h point group crystals.

[4] Zone-center optic: those phonon vibrations that retain the full crystal symmetry with non-zero energy at the zone center ($\vec{k}$ =0).

The scattered intensities, $I_{\parallel}$ and $I_{\perp}$, are either parallel or perpendicular, respectively, to the incident polarization $\vec{e}_i$. The scattered intensity is related to the Raman tensor ($\boldsymbol{R_j}$) and the polarization vectors $(\vec{e}_i, \vec{e}_j)$ by

$$I = c \cdot \sum \left| e_i \cdot R_j \cdot e_j \right|^2 \qquad i,j = 1,2,3$$

The Raman selection rules for this case reduce to:

$I_{\parallel} = 0$ and

$I_{\perp} = c \cdot d^2$, for $\vec{e}_i \parallel [100]$ and

$I_{\parallel} = c \cdot d^2$

$I_{\perp} = 0$, for $\vec{e}_i \parallel [110]$

where c is a constant, d is a parameter proportional to the intensity of the incident light and the Raman scattering cross section, and $\vec{e}_i$ is the incident light polarization.

For the Raman measurements described here, a Kaiser Optical Systems HoloProbe Raman spectrograph coupled to an Olympus BX-60 optical microscope was used with the 532 nm line of a frequency doubled Nd:YAG laser source. The polarization measurements used a fixed polarization of the incident beam and a $\lambda/2$ plate to rotate the scattered beam polarization. A 100X objective was used on the microscope for all measurements; this allowed the incident light to be focused to a spot approximately 1μm in diameter. As a result, both lateral (x,y) as well as depth (z) spatial resolution was possible. A natural type IIa diamond single crystal was used as a reference, with a single peak at 1332.3 cm^{-1} and linewidth 2.1 cm^{-1}. With a high-

resolution grating, the instrumental resolution of the Raman spectrometer used here is 1 cm^{-1}.

2.3.4 X-ray diffraction

X-ray diffraction measurements are done by placing a sample in a collimated, nearly monoenergetic x-ray beam at an angle, ω, to the surface of the sample, and detecting the diffracted x-ray intensity as a function of the scattering angle 2θ (Figure 6).

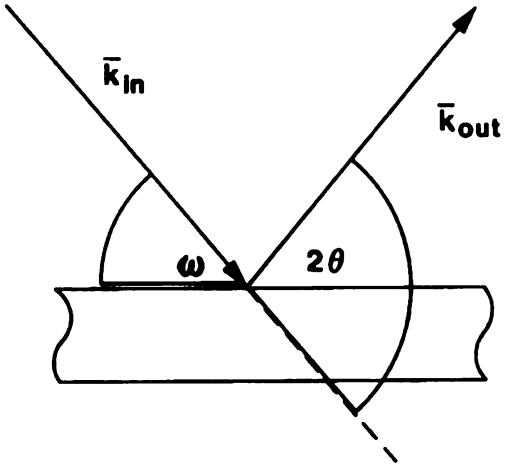

Figure 6 X-ray scattering geometry

The Bragg condition, $n\lambda = 2d\sin\theta$, corresponds to constructive interference and a peak in the scattered intensity, where λ is the wavelength of the incoming x-rays, d is the lattice spacing of the crystal, and n is an integer index corresponding to the scattering order. See Figure 7.

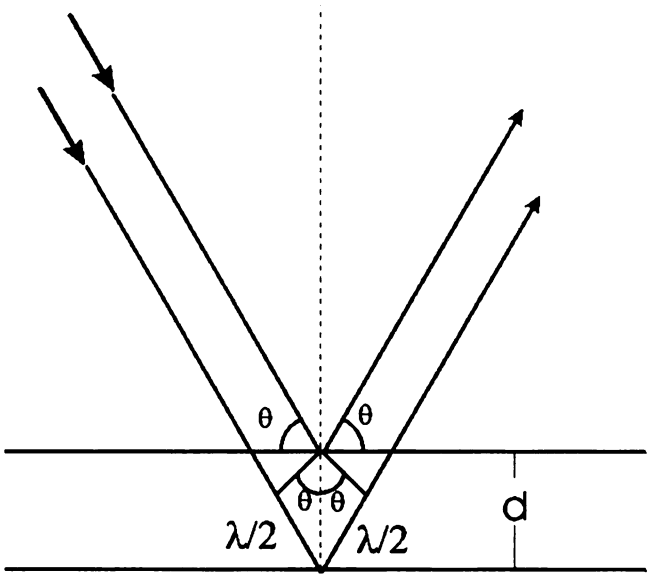

Figure 7 The Bragg condition for constructive interference

The Ewald construction is useful for understanding the geometry of x-ray diffractometers. In an Ewald construction, Figure 8, the incident x-ray $\vec{k}_{in}$ has an angle of incidence θ with respect to the hkl plane. A circle is drawn around the origin of $\vec{k}_{in}$ with a radius of $|\vec{k}_{in}| = \frac{2\pi}{\lambda}$.

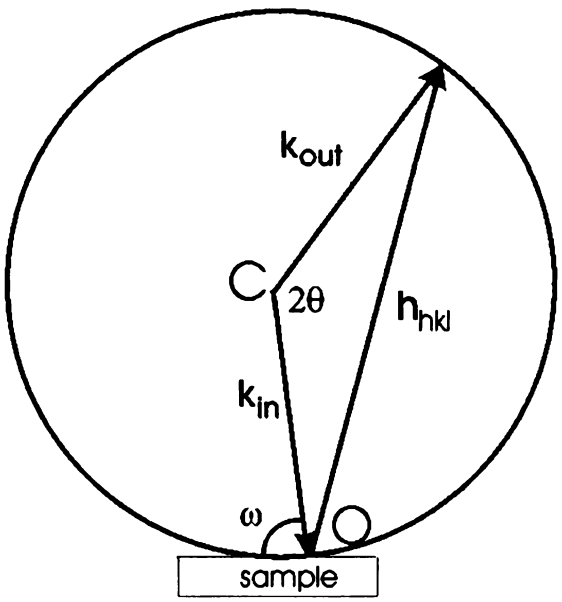

Figure 8 Ewald construction

Diffraction results along $\vec{k}_{out}$ only if $\Delta\vec{k} = \vec{k}_{out} - \vec{k}_{in} = 2\pi\vec{h}_{hkl}$ where $\vec{h}_{hkl}$ is the reciprocal lattice vector having length *1/d*. This can be restated as the Bragg condition:

$$\frac{k_{out} - k_{in}}{2\pi\lambda} = \frac{2\sin\theta}{2\pi\lambda} = \mid 2\pi\vec{h}_{hkl} \mid = 1/d \Rightarrow \lambda = 2d\sin\theta$$

The Ewald circle defines the Ewald sphere of radius $2\pi/\lambda$ about C in 3-D.

An x-ray diffractometer is used for precise measurement of the Bragg angles of diffraction of a crystal. A typical x-ray diffractometer with a 4-circle Eulerian-cradle is shown in Figure 9.

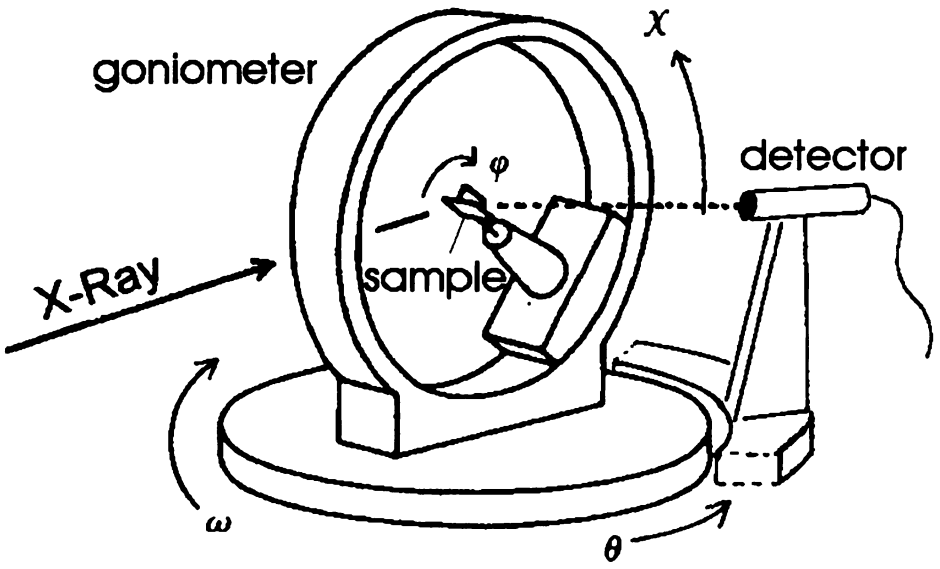

Figure 9 X-ray diffractometer geometry

The goniometer (a sample mount with three mutually perpendicular axes of rotation that allows very accurate centering of the sample in the diffractometer) is mounted on a ω-circle on a horizontal plane with a vertical rotation axis. A χ-circle is perpendicular to the ω-circle with a horizontal axis. The head of the goniometer is mounted on a third circle – the ϕ-circle inside of χ. The detector for the diffracted x-rays is on a fourth circle, θ, concentric with ω, but decoupled from the other three circles. The zeros of the circles are defined such that $\chi=0$ when the ϕ-axis is vertical, and $\omega=0$ when the χ-axis is parallel to the incident x-ray beam.

2.3.4.1 The ω-scan or rocking curve

For an ω-scan, the x-ray source and detector remain stationary. ϕ, χ, ω and 2θ positions are set to a calculated reflection position (i.e. (004) for the diamond structure). The crystal is rotated a few degrees through the reflecting position about ω, and the

intensity of the signal is recorded as a function of the angle. In the Ewald sphere representation, the ω-scan rotation is perpendicular to $\vec{h}_{hkl}$.

2.3.4.2 The θ-2θ scan, or ω-2θ scan

For the θ-2θ scan, both crystal and the detector are moved. The crystal is rotated by Δω as for the ω-scan, while the detector is rotated in the 2θ circle at 2 times the angular velocity of the crystal rotation, Δ2θ=2Δω at all times. In the Ewald sphere representation, the θ-2θ scan is in the direction of $\vec{h}_{hkl}$.

2.3.5 Atomic force microscopy (AFM)

An atomic force microscope uses a very sharp tip of radius <30nm to map the morphology of a sample surface on a scale of a few 100 nm to roughly 10 μm. The tip is at the end of a cantilever with a spring constant of the order 1 Newton/m. We use a Digital Instruments model 3100 in tapping mode with a Si tip to image the samples. In tapping mode, the tip is oscillated in air near the resonant frequency of the cantilever using a piezoelectric crystal *(23)*. The oscillating tip is brought near enough to the surface of the sample to touch. Changes in the topography as the tip rasters across the surface causes damping of the oscillations. The oscillation amplitude is maintained by a constant feedback loop in the system controller that interprets changes in signal amplitude as changes in topography. The movement of the tip is tracked by a photodetector that captures the light signal of a laser focused on the backside of the cantilever as it moves across the surface. A schematic of the system is shown in Figure 10.

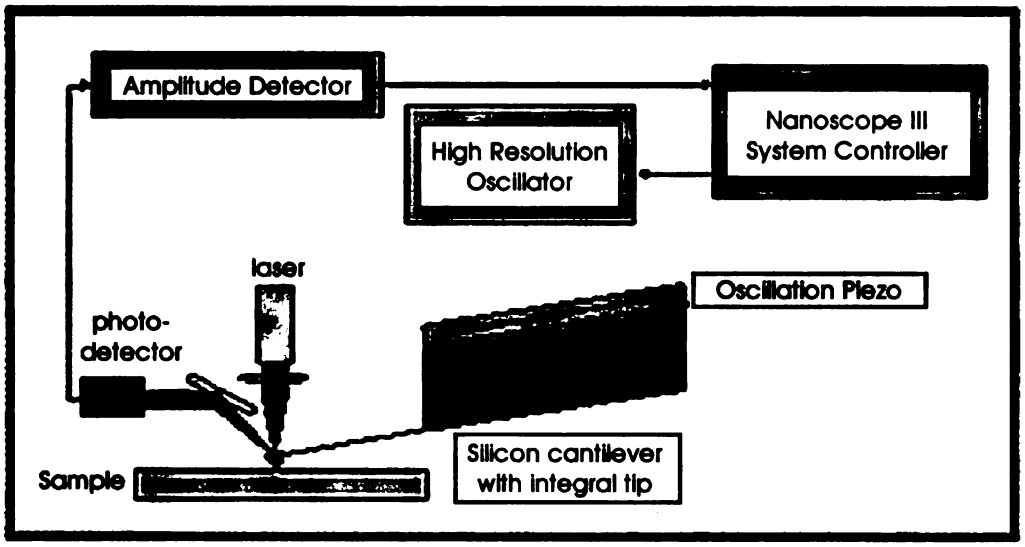

Figure 10 Schematic of an AFM in tapping mode *(23)*.

Chapter 3 Basics of crystal nucleation, epitaxy and plasma deposition

This chapter presents a brief description of crystal nucleation, the principle of epitaxial growth and crystal growth methods that were used in this work, particularly chemical vapor deposition (CVD). The nucleation and growth of diamond is discussed in this context. A description of DC glow discharges is given, as it will be used in Chapter 5 to explain the phenomenon of the secondary discharge during bias.

3.1 Nucleation: qualitative ideas

The process by which a substance "tries out" another phase is the essence of nucleation. In any medium, there are thermodynamic fluctuations. In the water-ice transition, as the temperature of water approaches 0°C, molecules slow down and occasionally a few attach in a way resembling ice crystals. Most of these "nuclei" break apart again into liquid phase, but as temperature decreases, attachment becomes more favorable. Eventually a nucleus reaches a critical size and growth of the crystal is thermodynamically favored over breaking apart again. Molecules will add to the nuclei and the transition from water to ice proceeds.

Nucleation can be broadly divided into two regimes, homogeneous and heterogeneous. Homogeneous nucleation describes a phase transition that is driven by

thermodynamics. Heterogeneous nucleation, on the other hand, can be compared to a catalytic process. Formation of a crystalline film on a surface is a heterogeneous process if the presence of the substrate activates the nucleation. Heterogeneous nucleation is essential for epitaxial thin film growth, as the growing film uses the substrate as a template for crystal growth.

3.2 Epitaxy

A crystalline substance (deposit) that grows on a crystalline substrate is said to be epitaxial if one crystal plane of the deposit crystal and one of the substrate are parallel. This can be described in terms of the Miller indices of the crystal planes and directions. For example, $(001)_d\langle 110\rangle_d \| (001)_s\langle 110\rangle_s$ means that a (001) plane of the deposit resides on a (001) plane of the substrate, with the deposit <110> direction parallel to the <110> substrate direction. In most epitaxial systems, the coincident growth planes are identical and of low index. Common growth planes are (001) and (111) for cubic systems or (0001) for hexagonal systems. The coincidence of high index dissimilar planes is also feasible. If a matching of two high index planes lowers the interface free energy, then such an arrangement will be favored in equilibrium. The *lattice mismatch, f,* between deposit and substrate is defined as

$$f = \frac{(a_{0D} - a_{0S})}{a_{0S}}$$

where a_{0S} and a_{0D} are the lattice parameters or atom unit spacings of the deposit and the substrate, respectively. A smaller lattice mismatch is possible if the relative difference becomes smaller at integer intervals of unit atom spacings, i.e. na_{0D}, ma_{0S}.

Homoepitaxy or *autoepitaxy* describes epitaxial systems where the deposit and substrate are the same substance. By including dopants in the epitaxial layer, one can produce thin layers of electronically modified materials on generic, low-cost substrates, for example, B-doped Si on Si. Growth of diamond on diamond substrates will be referred to as *diamond homoepitaxy*. *Heteroepitaxy* describes deposit-substrate systems where the epitaxial deposit and substrate are dissimilar and generally lattice mismatched. *Diamond heteroepitaxy* will be referred to as the epitaxial growth of diamond on another material.

3.2.1 Crystal growth modes

Following nucleation, crystal growth generally proceeds by one of three different modes: island growth, layer by layer, and layer plus island *(24)*. In some cases a combination of modes may occur. In 3-D island growth, also called Volmer-Weber growth, islands of deposit first form then coalesce after reaching a critical thickness. Islands then form on top of this deposit, and again coalesce. Here, the atoms of the deposit are more strongly attracted to each other than to the substrate. This is expressed as $\gamma_D + \gamma^* > \gamma_S$, where γ^* is the interface energy, and γ_D and γ_S are the surface energies of deposit and substrate *(25)*. In 2-D layer by layer, or Frank-van der Merwe growth, single layers form initially and grow mostly laterally along the substrate surface. For layer growth to proceed, the atoms in the deposit must be more strongly attracted to the substrate then each other, i.e., $\gamma_D + \gamma^* < \gamma_S$. The intermediate case – layer plus island, or Stranski-Krastanov growth, occurs if the interface energy increases with increasing deposit thickness. Usually this is the case for strained layer-growth. In SK mode, the first

2 to 3 monolayers grow in a layer type mechanism, and then islands grow on the layers. The three modes are shown schematically in Figure 11.

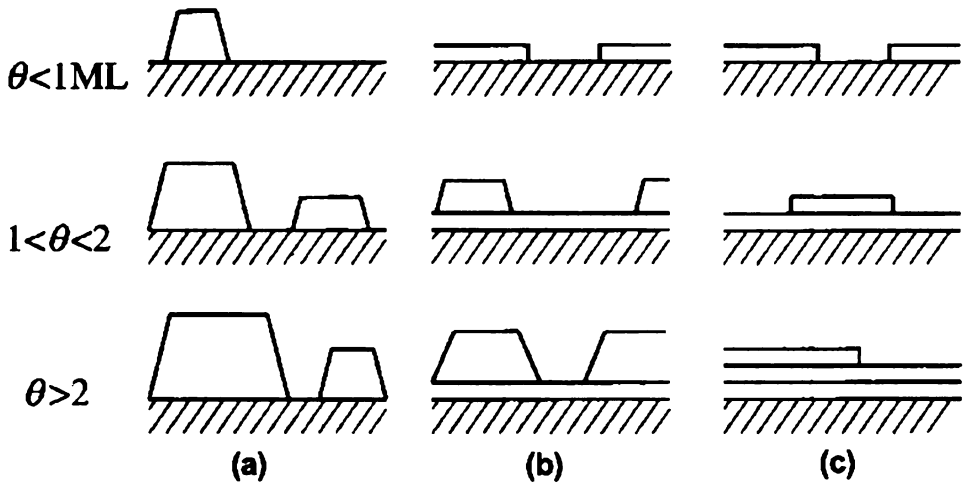

Figure 11 The three growth modes as a function of surface coverage, θ, in monolayers (ML): (a) island, or Volmer-Weber; (b) layer-plus-island, or Stranski-Krastanov; (c) layer-by-layer, or Frank-van der Merwe growth.

3.2.2 Substrates for diamond epitaxy

For heteroepitaxy, the choice of substrate is dictated by the following considerations:

(1) Similar structure as the deposit. For diamond this is the diamond, face-centered-cubic (FCC), or zinc-blende structure.

(2) One, or more, similar lattice parameters. The diamond lattice parameter is 0.3567 nm. Since the C-C sp^3 bond is 0.154 nm, most substrates will have larger lattice parameters than diamond.

(3) Stability of physical properties. The substrate should have a melting point much greater than the deposition temperatures. For diamond CVD, the substrate needs to be stable in a hot hydrogen plasma. Matching thermal

expansion coefficients (α) are preferred to minimize stress during cooling. See Table 1.

Material	$\alpha (10^{-6} K^{-1})$
Diamond	0.8
Silicon	2.3
Iridium	6.4
$SrTiO_3$	9
Sapphire	7.5
Platinum	8.8
Nickel	13.4
β-SiC	2.5

Table 1 Coefficient of thermal expansion for various substrate materials used in diamond heteroepitaxy (at 300 K).

(4) Surface energy match. Epitaxy is more likely if the surface energies of the two materials are similar, as is often the case for materials with similar lattice parameter and chemical bonding. Differences in surface energies lead to the different growth modes. For epitaxy, layer by layer growth is the preferred mode because fewer defects are introduced during growth.

In practice, it can be difficult to find substrates that satisfy the above criteria. For diamond, the small lattice parameter is only one of a number of hurdles that must be overcome in finding suitable substrates. CVD plasma temperatures are generally 800-1000°C, leading to rapid etching or decomposition of many substances. Table 1 indicates that materials used for diamond growth have thermal expansion coefficients much greater

than diamond. In addition, diamond has an extremely high surface energy, 5.3 J/m^2 for the (111) plane, 9.2 J/m^2 for the (100) plane *(26)*, compared to the substrate materials used for diamond growth. Large differences in surface energy between substrate and deposit inhibit formation of nuclei. Consequently homogeneous diamond nucleation occurs spontaneously only on other diamond surfaces.[5]

In the absence of an ideal economically attractive substrate, ways to circumvent the above requirements must be found. Diamond has already been demonstrated to grow with highly preferred orientation on silicon despite a 52% lattice mismatch, and a large difference in surface energy (1.5 J/m^2 for Si(100)). This indicates that diamond epitaxy on highly mismatched substrates may yet prove feasible. As will be shown in this thesis, single crystal diamond growth is possible on substrates that provide only a reasonably good match.

3.2.3 Other substrate criteria

Substrates should maintain phase stability over the span of temperatures encountered in diamond growth. Furthermore for diamond growth chemical stability, namely, carbide formation and carbon solubility need to be considered. The role of carbide formation is unclear and will be discussed below. It is also unclear whether carbon solubility should be a factor in substrate selection. The two above conditions are not necessarily mutually exclusive *(27)*. Diamond can form epitaxially on a substrate that 1) forms a flat, well-crystallized, carbide layer under diamond growth conditions, or 2) forms no carbide, but chemically bond with carbon, and has a small carbon solubility. In either case, the above criteria limit the choice for substrates in diamond growth.

[5] {111} c-BN with surface energy 4.8 J/m^2 and lattice parameter 0.3612 nm is an exception.

3.3 Thermodynamics and kinetics of diamond nucleation

In contrast to the ice-water nucleation, the multitude of condensed carbon phases greatly complicates diamond nucleation and growth. At CVD temperatures and pressures, graphite is the ground state of carbon. Diamond is a metastable state of carbon. At room temperature and pressure, the free energy difference between graphite and carbon is 0.03 eV per atom *(28-30)*. However, there is a large activation barrier between the two phases, thus graphite is the thermodynamically favored state.

There are in general, two ways to create diamond under laboratory conditions. With the high pressure, high temperature (HPHT) methods, graphite is compressed and heated in the presence of a catalyst to thousands of atmospheres and over 2000 K. Chemical vapor deposition methods, on the other hand, operate at sub-atmospheric pressures (10^{-3} to 10^{1} Torr) and temperatures near 1000 K.

3.3.1 Chemical vapor deposition

Chemical vapor deposition (CVD) is a crystal growth technique that involves chemical reactions at a substrate surface. CVD is related to PVD (physical vapor deposition) and belongs to the subset of deposition techniques that includes molecular beam epitaxy (MBE), sputtering, evaporation (including electron beam evaporation) and laser ablation. Physical deposition processes involve only a state change at a substrate of the depositing species. Chemical deposition processes proceed using a chemical reaction, or set of reactions, at the surface. The rate of deposition depends on the reaction rates and the fluid dynamics of the system *(31)*. Generally, the exact chemistry that takes place is usually very difficult to elucidate experimentally, as the system may be far from equilibrium (kinetically controlled) rather than thermodynamically dominated (at

equilibrium) *(32)*. CVD may be classified into two general categories: thermal and activated. In thermal CVD, gas flows past a substrate that is heated to high temperatures to initiate surface reactions. In activated plasma CVD, energy to ionize gas species is provided by an external source, such as a plasma or hot filament. Surface reactions are controlled or strongly modified by the plasma properties. This allows the substrate to remain at a lower temperature. However, energy from the plasma also leads to heating of the substrate, blurring the distinction between the two categories. The diamond for this work was grown using an activated plasma CVD process.

3.3.2 Development of vapor growth methods for diamond growth

CVD methods have a long history of usage for semiconducting film growth *(33, 34)*. For diamond growth, CVD methods were initially complicated by the concurrent formation of graphite and diamond *(28, 35)*. The realization that preferential etching of graphite by atomic hydrogen in methane-hydrogen gas mixtures provided the basis for interest in hydrogen plasma CVD *(28, 36, 37)*. The report of {110} faceted homoepitaxial diamond growth from mixtures of hydrocarbon-hydrogen gases appeared in 1981 *(30)*. The process involved a thermal CVD process in a closed system by carbon transport from a solid graphite source to a diamond substrate using methane, ethane, ethylene, acetylene, and atomic hydrogen. The growth rate was 1 μm/hr at 1000° C. All other reported methods used before this point, suffered from a slow growth rate of 0.1 μm/hr or less *(28)*. Shortly after, a growth rate of several micrometers per hour was achieved using microwave and hot filament methods of gas decomposition *(38-40)*.

3.3.3 Diamond chemical vapor deposition methods

Diamond CVD methods use gas dissociation of hydrogen and carbon into atomic hydrogen and carbon and methyl radicals. A good review of various gas activation methods is given in *(33)*. Hot filament CVD (HFCVD) uses a DC filament to ionize the gases, whereas plasma torches are powered by DC arc discharges. Plasma torch deposition achieves some of the highest deposition rates recorded – in excess of 60 μm/hr *(41-43)*. Combustion methods are similar, using a highly exothermic reaction, e.g. acetylene-oxygen, to heat the gas species. ECR (electron cyclotron resonance) uses an applied magnetic field chosen so the resulting electron gyration frequency is equal to the microwave frequency. This allows increased plasma densities by enhanced microwave absorption *(33)*. RF (radio frequency) and microwave plasmas use electromagnetic radiation to heat and dissociate the gases to form a plasma. We use the last method. Microwaves travel from the power source via a waveguide into a reactor where they energize and dissociate the gases in a bell jar or other confined volume. A ball-like plasma forms a few centimeters above the substrate. The plasma is confined by the electromagnetic fields and the physical surfaces of the reactor.

3.4 Plasmas and chemical vapor deposition of diamond

The next section contains a brief introduction to glow discharge plasmas. The understanding of the regions of a plasma, and the current-voltage behavior is important for describing the bias-enhanced method we used for diamond nucleation. This is put into context of microwave plasma chemical vapor deposition – the method used for diamond growth in this study.

3.4.1 Properties of plasma

A plasma is a collection of positive and negative charge carriers with overall charge neutrality *(44)*. The charge neutrality condition gives plasmas some of their unique properties and distinguishes them from a neutral gas. For instance, electric and magnetic fields strongly influence plasmas. Charged particles of plasma will rearrange themselves to shield external and internal electrostatic fields to preserve charge neutrality. Charge neutrality, however, is only true on a macroscopic scale. At distances less than λ_D, the Debye length, fluctuations of local charge densities can exist. λ_D (in cm) is given by: $\lambda_D \approx 743 * \left(\frac{T_e}{N_e}\right)^{1/2}$ where T_e is the electron temperature (eV), and N_e is the number density of electrons (cm^{-3}). For a typical microwave plasma discharge, $T_e \approx 5$ eV and $N_e \approx 10^{12}\,cm^{-3}$, gives $\lambda_D \approx 0.02$ mm. This is typically much smaller than the system size, so the plasma is "quasineutral". The electrons and ions arrange themselves within the Debye length so that charge neutrality is preserved for distances greater than λ_D.

Plasmas differ due to pressure, particle density and temperature – see Figure 12.

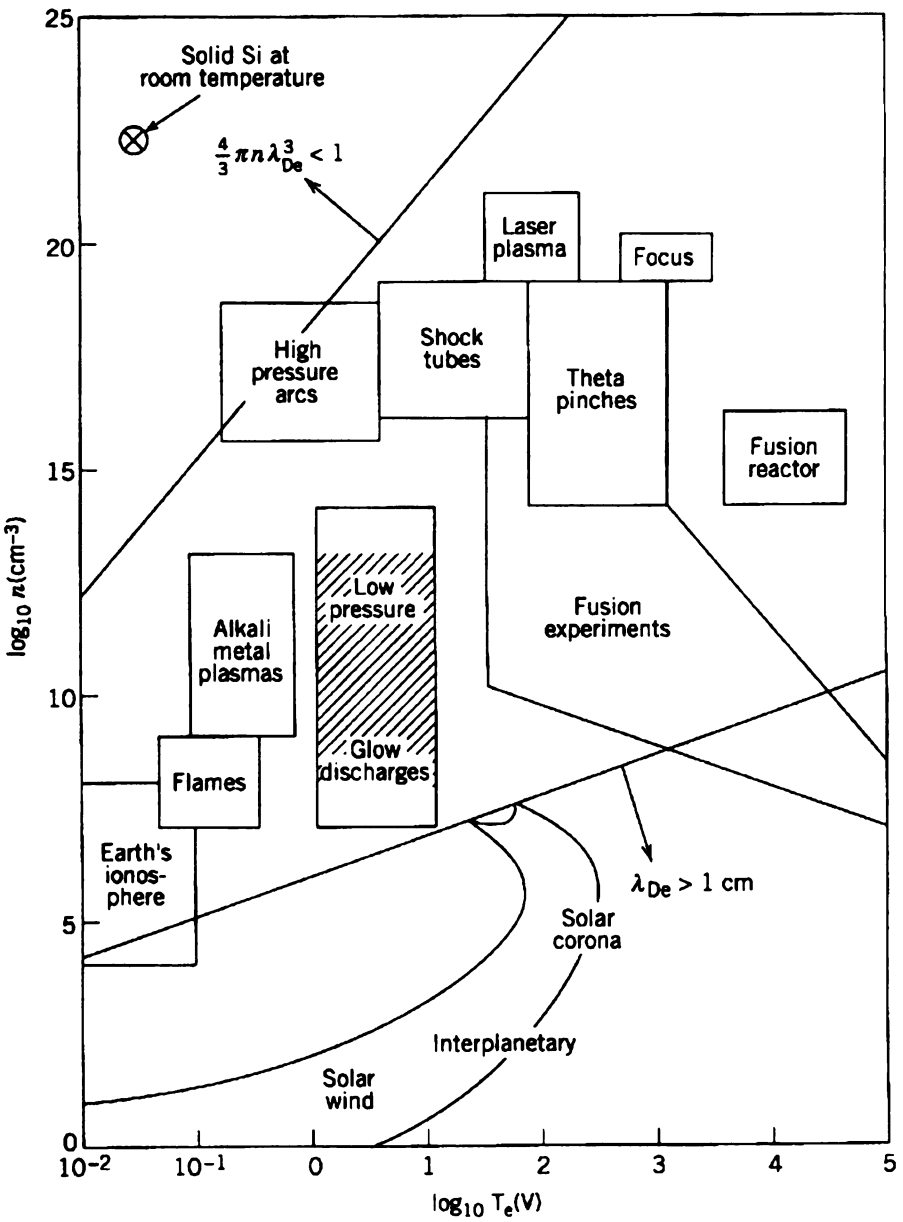

Figure 12 Laboratory and space plasmas on a density (n) vs. electron temperature (T_e) log-log plot. λ_D is the Debye length *(45)*.

Stars, for instance, are in thermal equilibrium, meaning all the species are completely ionized and $T_e \approx T_i$, where T_e and T_i are the temperatures of the electrons and ions. The electrons and ions are extremely mobile *(34)*. In the laboratory, gas discharge plasmas

occur when an electric potential applied across a gap "breaks down" the gas species to form a weakly ionized plasma *(45)*. Glow discharges generally have particle densities of 10^8-10^{12} cm^{-2}. These plasmas are not in thermal equilibrium because the electrons tend to be much hotter than the ions i.e., $T_e \rangle\rangle T_i$, and thus the plasma temperature is normally given by T_e. The electrons are colliding with gas molecules, dissociating them at temperatures much lower than in a thermal plasma *(34)*. This allows plasma processes in activated plasmas to occur at much lower temperatures than in thermal plasmas. Ionization occurs by electron collisions in the gas, rather than by thermal means, and the plasma is called a glow discharge.

Glow discharges can be formed at reduced pressures (P<atmosphere) by DC or AC electric fields applied across electrodes and AC current or radio or microwave frequencies passed through a coil around a tube. A DC plasma glow discharge and its main features are illustrated in Figure 13.

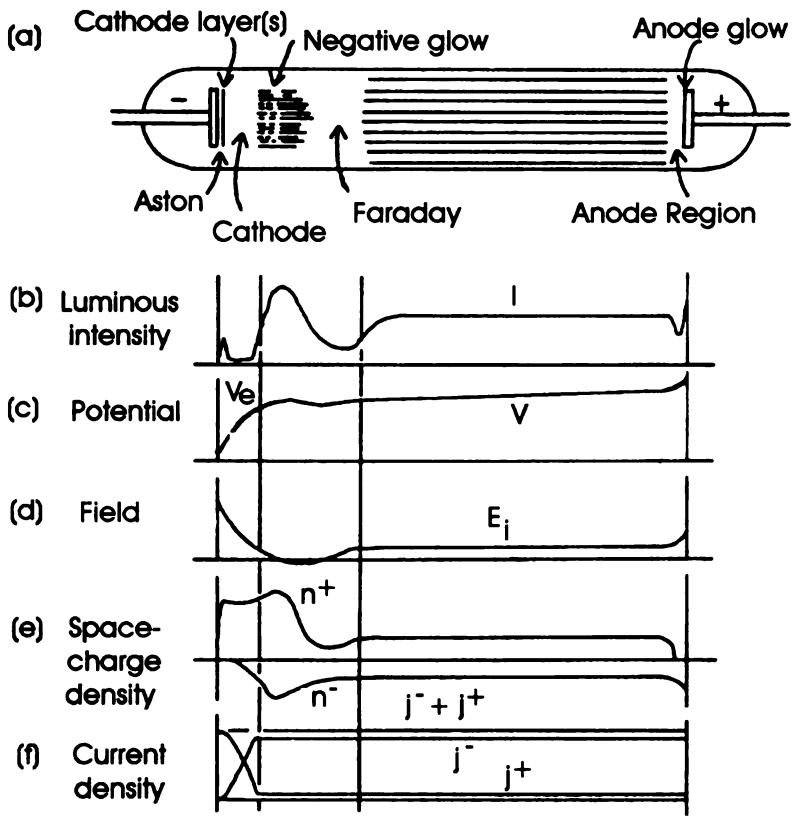

Figure 13 A DC Plasma glow discharge between two parallel plates *(44)*.

The glow discharge contains regions that are defined according to their luminosity, potential, field strength, space charge density and current density. Starting from the cathode the first three regions, the Aston dark space, the cathode glow and the cathode (or Crooke Hittorf) dark space comprise the cathode region. Most of the voltage drop in the discharge occurs in this region. The cathode glow has a relatively high ion density, and depending on the voltage will mask the dark spaces and cover the cathode. Next, come the negative glow region, the Faraday dark space, and the positive column. The positive column is often considered the main discharge, because it generally expands to occupy most of the volume. The negative glow has the brightest intensity, and electrons carry most of the current in this region. Last the anode dark space and the anode glow

comprise the anode region.

3.4.2 Microwave plasma discharges

At excitation frequencies >1MHz, direct contact of the plasma with electrodes is not needed. Electrodeless discharges can either be RF (radio frequency) or microwave discharges. Commonly used frequencies in commercial apparatus for microwave plasma chemical vapor deposition (MWPCVD) are 2.45 GHz and 915 MHz *(33)*. Some properties of typical microwave plasmas used for deposition are given in Table 2.

Power P (W)	500-5000
Pressure p (Torr)	0.1-10
Plasma density n (cm^{-3})	10^{10}-10^{12}
Electron temperature T_e (eV)	2-7
Ion acceleration energy E_I (V)	20-500
Fractional ionization	10^{-7}-10^{-4}

Table 2. Properties of a typical microwave plasma discharge *(45)*.

A microwave plasma discharge does not typically exhibit the different regions described for a DC discharge in the previous sections. Microwave plasma chemical vapor deposition uses a glow discharge plasma formed at reduced pressure by microwave excitement of the reactant gases.

3.5 Models of diamond nucleation for vapor phase growth

Most models of low pressure chemical vapor deposition of diamond consider it an activated process of reactants: hydrogenated carbon radicals, and atomic and molecular

hydrogen. The basic ideas are shown in Figure 14 for methane and hydrogen gases. The primary chemical reactions are summarized *(32)*:

$$H_2 \rightarrow 2H^0 \tag{1}$$

$$CH_4 + XH^0 \rightarrow CH_{4-X} + XH_2 \tag{2}$$

$$\begin{array}{c} | \\ -C-H \\ | \end{array} + CH_{4-X} \rightarrow \begin{array}{c} | \quad | \\ -C-C-H \\ | \quad | \end{array} + YH_2 \tag{3}$$

Equation (1) illustrates the dissociation of molecular hydrogen into atomic hydrogen; (2) shows the reaction of the atomic hydrogen to "abstract" a hydrogen radical from a methane molecule, forming a hydrogen molecule and a methyl radical, (3) shows the attachment of the methyl radical to a surface hydrogen terminated carbon atom, and subsequent detachment of a hydrogen molecule.

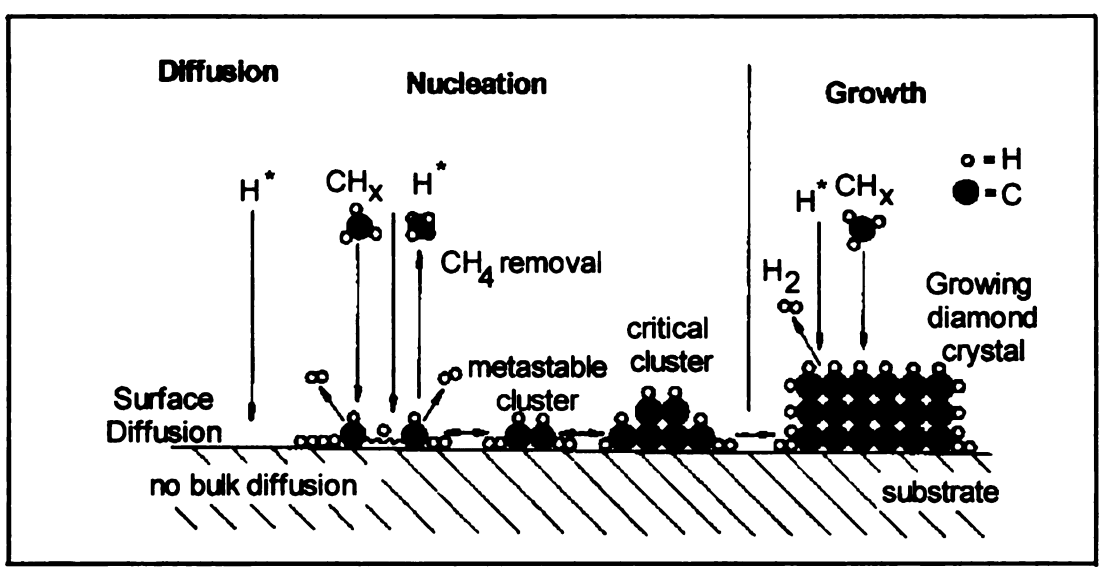

Figure 14 Nucleation and growth model of diamond growth on a substrate *(32)*.

Chapter 4 Prior studies of epitaxial diamond growth

4.1 Definition of diamond heteroepitaxy

As a working definition of diamond heteroepitaxy, we adopt the following criteria:

(1) **Size** - Growth over areas of order 1mm^2 or larger. This is necessary because it has long been possible to grow single crystals of diamond on substrates, including Si, that are facetted, but whose size rarely exceeds 10 μm on a side. Diamond heteroepitaxy implies that large scale coalescence of such oriented grains must occur over substantial regions of a substrate.

(2) **Chemical** – A Raman peak at 1332 ±10cm^{-1}, the C-C stretch in diamond, that obeys the diamond selection rules for polarization as discussed in section 2.3.3.

(3) **Structural** - X-ray, EBSD, or other diffraction confirming epitaxial alignment of diamond with the substrate. The linewidths provide a qualitative measure of coalescence, the distribution of orientations of crystallites and their grain boundaries. Epitaxial diamond is expected to have x-ray linewidths <1°.

We contrast these criteria with those describing highly ordered diamond (HOD); films that demonstrate some degree of epitaxial alignment, but still exhibit visible grain

boundaries. Thus, HOD can be viewed as epitaxial growth with significantly relaxed requirements of homogeneity.

This chapter presents the progress that has been made towards diamond heteroepitaxy on various substrates. To date, the following non-diamond substrates have been reported for diamond heteroepitaxial growth: Si, β-SiC, Cu, Pt*(46)*, Ni, Mo (and other carbide forming refractory metals), SiO_2, Co, Pd*(46)*, Au*(46)*, c-BN, sapphire, graphite, BeO, and Ir *(47, 48)*. Other than local epitaxy (on a nm scale), reports have been published of diamond epitaxy on Si, β-SiC, c-BN, Pt, Ni, and Ir. It is useful to divide the substrates into two categories: those where diamond is grown on a bulk crystal, namely, Si, β-SiC, c-BN, Pt, and Ni, and those where diamond is grown on a epitaxially grown thin film deposited on another substrate:β-SiC, Pt, and Ir. Tables 2 and 3 summarize the reports.

Table 3 Summary of diamond epitaxy experiments on bulk crystal substrates

Substrate	Structure, a_0, Mismatch	Diamond thickness, Area	Film texture	Epitaxial relationship	Rocking curve (FWHM)	Raman Linewidth (FWHM)	Nucleation Density (cm^{-2})	Reference
c-BN $(111)_B$ Single crystal	Zinc-blende, 0.3612 nm 1.5%	0.1-0.2 μm 100-200 μm	Single crystal	$(111)_{Di}<110>_{Di}\|\|$ $(111)_{c\text{-}BN}<110>_{c\text{-}BN}$		1325 cm^{-1}, 12.9 cm^{-1} *	10^{11}	*(49, 50)*
c-BN (100) Single Crystal	Zinc-blende, 0.3612 nm 1.5%	1-2 μm 100-200 μm	HOD	$(100)_{Di}<110>_{Di}\|\|$ $(100)_{c\text{-}BN}<110>_{c\text{-}BN}$				*(51)*
Ni (100)‡ Ni (111)	FCC, 0.352 nm 1.3%	30 μm NA	Textured			1334 cm^{-1}, 5 cm^{-1} (100) 8 cm^{-1} (111)	~10^8	*(52, 53)*
Pt (111) Single crystal	FCC, 0.392 nm 9%	3 μm 12 mm Ø	HOD	$(111)_{Di}<110>_{Di}\|\|$ $(111)_{Pt}<110>_{Pt}$	4°	†		*(54)*
Si (100) Single crystal	Diamond 0.543nm 52%	16 μm 2" Ø	HOD	$(100)_{Di}<110>_{Di}\|\|$ $(100)_{Si}<110>_{Si}$	2.1°			*(55)*

* Polarized Raman showed it to obey the Raman selection rules.
‡ Polycrystalline substrate that exhibited (100) and (111) grains.
† Peak at 1440 cm^{-1} is dominant (Diamond-like carbon – mix of sp^2 and sp^3 C-C bonds.

Table 4 Summary of epitaxy on thin film single crystal substrates

Substrate	Structure, a_0, Mismatch	Film thickness	Diamond thickness, Area	Film texture	Epitaxial relationship	Rocking Curve (FWHM)	Raman Linewidth (FWHM)	Nucleation Density	Reference
$(100)_{\beta\text{-SiC}}\|\|$ $(001)_{Si}$	Zinc-blende 0.436 nm 22%	320-500nm	20 μm 4x3mm^2	HOD - single crystal		0.92-1.5°		$5x10^{10}$-$1x10^{11}$	*(56, 57)*
$(111)_{Pt}\|\|$ $(111)_{SrTiO_3}$	FCC, 0.392 nm 11%		3 μm 5x5mm^2	HOD		4.0°			*(58)*
$(111)_{Pt}<110>_{Pt}$ $\|\|(0001)_{Al_2O_3}$ $<10\bar{1}0>_{Al_2O_3}$	FCC, 0.392 nm 11%	0.4 μm	1.5 μm 5x10mm^2	HOD	$\{111\}_{Di}\|\|$ $\{111\}_{Pt}$	2.0°	1334 cm^{-1}, 15 cm^{-1}		*(59)*
Pt/Ir/Pt(111)$\|\|$ $(0001)_{Al_2O_3}$	FCC, 0.392 nm 11%	2/1/2 μm 3-5μm total	1.5μm 10x10mm^2	HOD		1.1°			
$(100)_{Ir}\|\|$ $(100)_{MgO}$	FCC, 0.3840nm 7.5%	500nm	1.5-8 μm 2x2mm^2	Single crystal	$(100)_{Di}<110>_{Di}$ $\|\|(100)_{Ir},<110>_{Ir}$		1332 cm^{-1} 18cm^{-1}	10^8	*(4, 5)*
$(100)_{Ir}\|\|$ $(100)_{MgO}$	FCC, 0.3840nm 7.5%	500nm ? from *(5)*	* 4x4mm^2	HOD	$(100)_{Di}<110>_{Di}$ $\|\|(100)_{Ir},<110>_{Ir}$	0.16°	1333 cm^{-1} †	>1.5x10^8	*(6)*
$(100)_{Ir}\|\|$ $(100)_{SrTiO_3}$	FCC, 0.3840nm 7.5%	3-200nm	8 μm 4mm Ø	Single crystal	$(100)_{Di}<110>_{Di}$ $\|\|(100)_{Ir},<110>_{Ir}$	0.34°		10^9	*(7, 8, 60)*

* The film was grown for 2.5hrs; no thickness is given. 4x4 mm^2 is the substrate size. There is no indication of the diamond area.
† Plus non-diamond peaks

Where multiple reports exist, the results are either combined (for work within the same group), or the best example is chosen. Examples with thinner diamond films showing epitaxy are given preference as being more representative. Blank fields in the above tables indicate the value was not given or could not be deduced from the report. The following sections explain the data in the tables in more detail.

4.2 Diamond epitaxy on bulk substrates

4.2.1 Cubic boron nitride

Cubic boron nitride was an early choice for diamond heteroepitaxy because it has a similar lattice constant of 0.3612 nm (mismatch 1.5%), a similar structure (zinc blende), and a similarly high surface energy (4.8 J/m^2 for the (111) surface). Diamond has been grown heteroepitaxially on c-BN, with a growth process similar to diamond homoepitaxy *(49, 61, 62)*. Reflection high-energy electron diffraction (RHEED) showed twinned epitaxial diamond grew on {111}c-BN with the epitaxial relation: $(111)_{Di}<110>_{Di}||(111)_{c\text{-}BN}<110>_{c\text{-}BN}$ using DC-plasma CVD with 0.5% CH_4 in H_2 at 180 Torr, and substrate temperature of 900° C. A continuous film formed at 0.2 μm thickness *(49)*. Polarized Raman scattering obeyed selection rules for a 0.1-μm film, but with a C-C peak at 1325 cm^{-1}, having a linewidth of 12.9 cm^{-1} that was attributed to tensile stress in the film. This study utilized substrate areas of only 100-200 μm. Although important as an early demonstration of the feasibility of diamond heteroepitaxy, the limited substrate size of c-BN, itself difficult to grow, means it has limited applicability. The largest c-BN single crystals available are only 1-3 mm, and they often have many impurities *(63, 64)*.

4.2.2 Nickel

Diamond (111) and (100) was reported to grow on nickel (100) and (111) epitaxially *(65)*. Ni (FCC) has a lattice parameter close to diamond, 0.352 nm (1.3% mismatch). 49 hr of growth at 900-950° C in a 0.5% CH_4 plasma in a HFCVD system produced a coalesced, oriented diamond film 30 μm thick. Raman peaks appeared at 1334 cm^{-1} for (100) and (111) diamond on (100) and (111) Ni, with linewidths of 5 cm^{-1} and 8 cm^{-1} respectively. The processing for seeding the Ni substrates increased the density and growth rate of the epitaxial particles, leading to some coalescence. But roughening due to the high carbon solubility of nickel served to limit the final film quality. The work was done on a polycrystalline Ni substrate with no mention of the grain sizes, nor the total area of growth. Diamond crystals were reported as 3 μm after 7 hrs of growth, with a density of 10^8 cm^{-2}.

4.2.3 Platinum

Platinum (FCC) has a lattice parameter 0.392 nm (9% mismatch with diamond). Diamond (111) deposited on Pt(111) bulk substrates has been demonstrated on a 12 mm diameter circular region by Tachibana et al *(54, 66)*. They used microwave plasma CVD in a quartz-tube reactor to grow diamond with 0.2-0.3% CH_4 in a balance of H_2 at 50-60 Torr at substrate temperatures of 850°-880° C. These conditions yielded a growth rate of approximately 0.3 μm/hr on (111) Pt. A 3 μm thick film had an X-ray Pt{111) peak with linewidth of approximately 4°. The Raman spectrum showed a small peak at 1330 cm^{-1} with a dominant peak at 1440 cm^{-1} (disordered carbon). SEM showed a <111> textured film. According to the above classification scheme, this film would be HOD.

4.2.4 Silicon

The term highly oriented diamond (HOD) was first used to describe heteroepitaxial growth of diamond on silicon. Si (diamond-structure) has a lattice parameter of 0.543 nm (52% mismatch). Despite this, oriented crystallites on a (100) Si substrate have been grown using microwave plasma CVD *(2, 3)*. X-ray pole figures showed a $(001)_{diamond}$ $<110>_{diamond}$ || $(001)_{Si}$ $<110>_{Si}$ relation, although, grain boundaries are apparent between the crystals from SEM. No quantitative analysis was done to show the degree of orientation. Raman spectroscopy revealed a diamond peak at 1335 cm^{-1}, with a broad weaker peak at 1550 cm^{-1}. All of the techniques for highly oriented diamond growth involve a multi-step bias and growth process, to exploit crystal texture evolution. The best film on Si reported to date has a linewidth of the (004) rocking curve of 2.1° for a 2-in diameter 16 μm thick boron-doped film *(55)*. Raman spectroscopy was not reported for this film.

4.3 Diamond epitaxy on thin films

4.3.1 Pt{111}/sapphire{0001} and Pt{111}/$SrTiO_3${111}

Diamond grown on Pt{111}/ $SrTiO_3${111} gave similar Raman and X-ray results to that grown on single crystals *(67)*. Pt{111} thin films deposited epitaxially on sapphire{0001} exhibited better structural quality than the single crystal Pt or Pt deposited on $SrTiO_3$ *(59)*. Growth conditions were the same as for the bulk Pt substrates. Higher nucleation densities were observed (>$1x10^8$ cm^{-2}) for the same type of seeding process as on bulk substrates. A 1.5 μm thick diamond sample had a (111) x-ray rocking curve with a linewidth of 2.0°. SEM showed a <111>-textured film with grain sizes of

30-50 μm. At 9 μm thickness, the film coalesced, with some remnant grain boundaries, and (111) x-ray rocking curve linewidths of 0.4-1.0°. The Raman spectrum, with 488 nm excitation, showed a peak at 1334 cm^{-1} with linewidth 15 cm^{-1}, and a broad peak around 1550 cm^{-1} (sp^2-bonded carbon). The (111) x-ray rocking curve linewidth of a 1.5 μm thick film decreased to 1.1° when an interlayer of 1μm Ir(111) was deposited between two 1-2 μm Pt(111) layers on sapphire(1000) *(54)*. The film covered an area of 10x10mm^2. A SEM micrograph is shown in Figure 15.

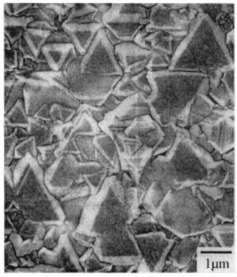

Figure 15 SEM micrograph of a 1.5μm thick diamond film on (111)Pt/Ir/Pt/(0001)sapphire substrate *(54)*.

4.3.2 β-SiC/Si

β-SiC (zinc blende structure) with a_0 = 0.436 nm has a 22% mismatch to diamond. The process for growing epitaxial diamond on SiC began by first depositing 320-500 nm of epitaxial β-SiC (001) on Si(001) substrates *(68)*. Then a four-step process was followed to grow diamond using MWPCVD. Particle density was reported as 0.5-1x10^{11}

cm^{-2} after nucleation. After the initial growth step, reflection high-energy electron diffraction (RHEED) showed a dispersion of approximately 2°. A final growth step yielded smooth films with some visible grain boundaries at a density of 10^4 cm^{-2} in the best 5x5 mm^2 area. Steps appeared on a 20 μm thick sample (grown for 12 hrs) with step height 30-50 nm in <110> and $\langle 1\bar{1}0 \rangle$ directions. A 300 μm thick (240 hrs) sample did not show such steps, but had a surface roughness of 100-150 nm over a 50x50 μm^2 area *(57)*. For a 20 μm film, the x-ray linewidth was 1.5° representing the angular distribution of the crystals, with an intensity due to first-order twins less than 1% of the other (111), (220), (400) reflections. The FWHM of the x-ray rocking curve (ω–scan) of the diamond (004) was 0.92° in the best region. The 300 μm film showed an improvement to 0.62°, over an area larger than 1 mm^2. Improvement in the x-ray rocking-curve linewidth of the thick diamond is due to the high nucleation density of oriented particles, and the effective use of a process to select particles with the correct orientation during growth *(57)*.

4.3.3 Iridium

Iridium, first proposed as a substrate for diamond heteroepitaxy in 1996, *(5)* is a FCC metal with a lattice mismatch of 7.5% to diamond. Iridium has one of the lowest carbon solubilities (by weight) of the platinum metal group *(69)*. It is stable with no known phase transitions. Iridium can be grown epitaxially on other single crystal substrates and used as a substrate for diamond growth, as now demonstrated by several groups *(4-6, 8, 70)*. A comparison of iridium preparation and diamond growth methods reported by these groups is presented in Tables 5 and 6.

Table 5 Sample preparation for Ir and diamond growth system.

	Sawabe et al. *(4, 5, 27, 71, 72)*	**Maeda et al.** *(6, 73)*	**Schreck et al.** *(8, 74)*	**Bednarski et al.** *(70) (75)*
Substrate				
Base material	MgO (cleaved)	MgO (cleaved)	$SrTiO_3$	$SrTiO_3$, $LaAlO_3$,MgO,Al_2O_3
Ir thickness	300-500nm	--	30-200nm	80-300nm
Deposition temperature	650-750° C (950° anneal)	900° C	950° C	800°-850° C
Sample size	10 x 10 mm	4 x 4 mm	10 x 10 mm	5 x 5 – 10 x 10 mm
Deposition method	E-beam, RF sputtering	RF sputtering	E-beam	E-beam
CVD method	HFCVD	MPCVD	MPCVD	MPCVD

Table 6 Growth parameters for groups studying diamond heteroepitaxy on Ir

Parameters	**Sawabe et al.**	**Maeda et al.**	**Schreck et al.**	**Bednarski et al.**
MW power	N.A.	260-380 W	1100 W	1500 W (650 W abs)
Bias voltage	-260V (-150V net)	-150 to –200 V	-250 V	-150 V
Current	70 mA/cm^2	--	10 mA *	30-50 mA
Bias time	5-10 min	15-60 min	25-60 min	50-60 min
Pressure				
Bias	100 Torr	30 Torr	22.5 Torr	18 Torr
Growth	200 Torr	40 Torr	22.5 Torr	18-28 Torr
Geometry				
Gas confinement	Stainless chamber	Quartz tube	Stainless chamber	Quartz bell jar
Distance to sample from bias filament	1mm (needle)	2 – 7 mm (needle)	20 mm * (ring)	32 mm (ring)
System size	Small	Small	--	Large volume
Electrical contact	--	Mo mask/full metallization	Oxygen reduction of substrate	Mo cap
Temperature				
Bias	900° C	800° C	700° C	710-730° C
Growth	840° C	700° C	700° C	665° C
Measurement method	--	O.P. $\varepsilon = 0.3$	Thermocouple	O.P. $\varepsilon = 0.65$
Nucleation density	0.15-1.5x10^8 cm^{-2}	>1.5x10^8 cm^{-2}	10^9 cm^{-2}	3-6x10^{11} cm^{-2}

O.P. = Optical Pyrometer

* From the work on silicon in the same system *(76)*

Diamond growth on Ir was first reported by Ohtsuka et al. in 1996. They grew epitaxial (100) Ir films by RF magnetron sputtering on cleaved (001) MgO surfaces *(5)*. Subsequent diamond deposition used dc-plasma CVD with a 5-10 minute bias at –150V at 900° C, followed by 30 minutes of growth at 840° C. Initial studies revealed only "patchy" dense areas of nucleation that coalesced to form single crystals. After 30 minutes of growth, pyramidal structures with distinct {111} facets appeared with density of order 10^8 cm^{-2}. Single crystal films about 1 mm^2 with mean thickness of 1.5 μm resulted *(4)*. Cross-sectional analysis by SEM indicated residual grain boundaries. The Raman linewidth at 1332 cm^{-1} was 18 cm^{-1} and the film had a average roughness of order 1 nm. This group has since demonstrated an 8 μm thick freestanding film of size 2x2 mm that cleaved along the {111} planes *(71)*. Depth profiles of the Raman spectra were reported, but no quantitative Raman or x-ray linewidth measurements. RHEED showed a streaky spot pattern along <110>. The epitaxial relation reported was $(100)_{diamond}$ $<001>_{diamond}$ $||(100)_{Ir}$ $<001>_{Ir}$. They observed a non-diamond carbon signal in the Raman measurement within 1000 nm of the back surface.

Schreck et al. *(8)* have grown single crystal Ir films on $SrTiO_3$ substrates by electron beam evaporation. Using microwave plasma CVD, they observed epitaxial diamond nucleation with density 10^9 cm^{-2}. Unlike the others, they added 30-50 ppm of N_2 to the gas mixture for the nucleation and growth. For an 8 μm film, they measured a (004) rocking curve and a (311) azimuthal scan with linewidths of 0.34° and 0.65° respectively. Raman spectra from epitaxial areas of a 600 nm film (shown in Chapter 9, Figure 73 (2a)) had a 15 cm^{-1} linewidth with an upward shift of 1340 cm^{-1}, which they attributed to a biaxial stress in the (001) plane *(60)*.

4.4 Comments and perspectives

Although heteroepitaxial growth of diamond has been the goal for many research groups, few efforts have satisfied the criteria outlined in the introduction to this chapter. Perhaps the best example is thick diamond on β-SiC; but no chemical analysis has been reported yet. Pt does not appear to be very promising as grain boundaries persist for large thickness on {111} surfaces. Ir seems to have the greatest potential with several impressive results.

In the present research, we have grown iridium on $SrTiO_3$, MgO, $LaAlO_3$, and Al_2O_3 substrates. We have shown that single crystal diamond is indeed possible on all of these substrates. With nucleation densities two orders of magnitude higher than prior reports, we have produced completely coalesced diamond films of thickness below 1 μm. This thesis describes diamond growth on Ir surfaces that satisfy all the criteria for true heteroepitaxy.

Chapter 5 The bias process

Negative biasing of the substrate in the presence of a hydrogen-hydrocarbon plasma is an important method to achieve high nucleation densities. This chapter describes the method and discusses some of the mechanisms that have been proposed to explain the enhanced nucleation densities. Although of general applicability, biasing is discussed in the context of experiments of diamond growth on silicon, the most carefully studied system. A few remarks on the role biasing plays in nucleation on Ir are also given. Since negative biasing of the substrate leads to low-energy ion bombardment, it is reasonable to suspect implantation (sometimes subplantation) as the cause of the nucleation. The appearance of a cathode sheath or secondary plasma during biasing, however, suggests enhanced electron emission is a component of the process. We discuss the secondary glow observed during biasing and its role on nucleation events and epitaxy.

5.1 Seeding for diamond growth

Inducing a sufficiently high nucleation density is a fundamental problem that must be overcome in growing diamond. Diamond's high surface energy does not allow it to spontaneously nucleate on foreign substrates. Thus, to promote diamond growth, non-diamond substrates must be "seeded". Early experiments employed a scratch-seeding method. The substrate is polished or ultrasonicated with a small grit 10-25 μm diamond powder. This may introduce defects or implant small diamond particles in the

substrate allowing diamond to nucleate *(77, 78)*. This may not promote epitaxy, as defects or roughness in the substrate surface can propagate into the growing film, or the nuclei will not have epitaxial registry with the substrate.

5.2 Biasing

Bias enhanced nucleation (BEN) is a process that accelerates low energy ions towards a substrate in the presence of a dc voltage drop across the plasma. The term ion-enhanced nucleation has also been used. In its first embodiment *(9)*, an increased nucleation density on Si to 10^{10} cm^{-2} was seen when a negative bias was applied to the substrate with respect to the plasma. Using MPCVD, bias voltages between +100 to -200 V were applied to Si (100) with resistivity of several Ω-cm. Biasing for 2-15 min followed by 30 min of unbiased growth revealed increased nucleation densities for voltages lower than -70 V. No oriented nuclei were observed, but the demonstration of an alternative to scratch seeding spurred exploration of heteroepitaxial growth. Using BEN methods, oriented nucleation of diamond on silicon carbide was next demonstrated *(79)*, followed shortly by heteroepitaxy attempts of diamond on silicon and other substrates *(1, 2, 80)*. Why this method increases nucleation density on Si, and how it leads to epitaxy are questions under current debate.

5.3 Models and mechanisms for diamond nucleation due to BEN

Ion bombardment and electron emission have been proposed as mechanisms for the increased nucleation densities due to BEN processing. As a negative bias to the substrate has been shown to increase nucleation densities *(9, 81)*, it seems logical to assume the ion bombardment from dissociated positive ions in the plasma is responsible.

However, the indication that a positive bias is also effective at increasing nucleation *(82, 83)*, that increased densities are also found during biasing with HFCVD, which does not produce large amounts of positive ions *(28, 84)*, and that nucleation densities can be increased by placing diamond surfaces in the vicinity of the substrate during biasing *(85, 86)* led many researchers to suggest electron emission may play a prominent role in biased enhanced nucleation.

5.3.1 Ion bombardment

Based on the experiments described in Section 5.2, Yugo et al. *(9)* first proposed ion bombardment as a nucleation mechanism, claiming the acceleration of positive ions increased the "active" species near the substrate by collisions, thereby enhancing the diamond nucleation rate. The ion bombardment may also preferentially etch amorphous or graphitic carbon. It was inferred that the ion bombardment mechanism is a delicate balance between formation of sp^3 bonds and etching of sp^2 bonds. The following studies clearly indicated ion bombardment plays an active role in the nucleation enhancement.

Schreck et al. *(76)* studied the anisotropy of ion bombardment by using lithography to pattern a silicon wafer with evenly spaced cylindrical columns of 5 μm diameter and 8.5 μm height. The sample was then biased with a BEN process (–200 V at 10-20 mA) that was terminated at the first sign of current increase (after 5-20 min). Subsequent two-hour growth showed the tops of the columns and the intervening surfaces in between covered with a dense diamond film; the sidewalls were almost bare. The conclusion was that anisotropy arising from the nearly ballistic ion flux explained the spatially selective nucleation. Other groups have done similar studies with lithographic

patterned or etched silicon which show nucleation is increased (10^8-10^{10} cm^{-2}) on top surfaces, and negligible at the sidewalls *(87, 88)*.

In a more recent work, similarities were noted between bias-enhanced nucleation on silicon and nucleation on a substrate exposed to a low energy carbon ion-beam *(89) (90)*. Liao et al. *(89)* used a mass-separated ion beam deposition technique to implant Si with 100 eV carbon ions, with reference to suggestions by Robertson et al. *(91, 92)* . The substrate temperature was maintained at 800° C, and the ion dose was $2x10^{18}$ cm^{-2}. Upon examination of the Si using XPS (x-ray photoelectron spectroscopy), AES (Auger Electron Spectroscopy), Raman spectroscopy, X-ray diffraction and AFM, no Si peak was found using XPS and the surface was fully covered by carbon. AES showed a film that was mostly amorphous carbon. The Raman spectrum showed peaks at 1590 cm^{-1} (graphite) and 1352 cm^{-1}, usually attributed to microcrystalline graphite, and a small shoulder around 1173 cm^{-1}, a signature for nanocrystalline diamond. XRD showed characteristics of diamond and graphite grains embedded in an amorphous carbon matrix. With AFM, they observed oriented square 80-100 nm crystallites, believed to be (0002) graphite surrounded by amorphous carbon. Growth of these samples in a HFCVD reactor under conditions for microcrystalline diamond resulted in diamond nanocrystalline films, with a nucleation density comparable those produced by BEN *(93)*.

The suggested mechanisms by which ion-bombardment leads to formation of nucleation sites are: (1) ion subplantation, (2) growth of a carbon non-diamond layer, (3) increased surface diffusion and (4) growth of a SiC buffer layer. These mechanisms are discussed below.

5.3.1.1 Ion bombardment leads to ion subplantation

Lifshitz et al. *(94, 95)* proposed ion subplantation, as the main result of ion bombardment during BEN, based on experimental evidence and molecular dynamic simulations. Ion subplantation is the deposition of hyperthermal (1-10^3 eV) species via a shallow subsurface implantation *(94)*. To understand the role of subplantation, Robertson et al. *(91)* measured the ion energy distribution (IED) using a retarding field probe inserted in a hole in the substrate for samples biased between –150 and –300V. The IED was sharply peaked at 80 eV at the optimal conditions of 2% methane, -250V. In other studies *(96, 97)* it was found that carbon ion subplantation in Si is most efficient around 100 eV. As these energies were in agreement with the Lifshitz model *(94)*, it was concluded that ion subplantation is the dominant mechanism of nucleation in Si, creating "diamond-like carbon" with nanocrystalline diamond features in an ordered graphitic deposit. Other molecular dynamics studies have also suggested an energy window between 40-70 eV for the deposited atoms *(98)*. A few studies have looked at the ion-energy distribution in the plasma to determine the main species bombarding the substrate. Kátai et al. *(99, 100)*, using ion beam mass spectrometry, found that the hydrocarbon radicals C^+, CH^+, CH_2^+, $C_2H_2^+$, and $C_2H_3^+$ with average energies 50-70 eV are the dominant species at the onset of bias. As the current increases (with the appearance of a secondary plasma over the sample) $C_2H_3^+$ species (E=95-105 eV) and H^+ and H_3^+ (E=160-180 eV) become dominant. Kim et al. *(101)* likewise investigated the plasma species during bias using optical emission spectroscopy (OES). Increased levels of atomic hydrogen and hydrocarbon radicals, particularly CH^+ appeared for bias voltages between –100V and –250V. They proposed that subplantation of carbon species leads to

epitaxial formation of SiC and further bias leads to etching of Si atoms with replacement by carbon atoms and forming sp^3 bonded structures *(102)*.

5.3.1.2 Ion bombardment causes growth of a non-diamond carbon layer

McGinnis et al. *(103)* believed a subplantation model was not necessary. The average energy of carbon ions at the substrate was calculated to be around 15 eV, which would correspond to a surface process rather than subplantation *(95, 104)*. Using SEM, Raman microscopy, cross-sectional TEM, and x-ray diffraction, they observed evidence of nanocrystalline diamond in a non-diamond carbon matrix. A nucleation density of 10^{11} cm^{-2} for a sample biased for 1 hr at -250 to -300 V was reported along with the suggestion that a threshold voltage must be exceeded for the ion bombardment mechanism to be effective *(105)*. In two sets of experiments, bias nucleation density enhancements were related directly to ion bombardment. For the first, a series of experiments were run under identical process treatments. They made nine separate runs applying a bias from 0 to –333 V in 2% CH_4. Bias duration lasted from 12 min (333V) up to 300 min (0V). The application time for the bias was calculated to keep the time-integrated bias current approximately equal for all samples. Higher bias voltage caused a sharper increase in bias current, which meant a shorter bias time was necessary for the total current flux to the substrate to remain constant. The plot of nucleation density with applied bias is shown in Figure 16.

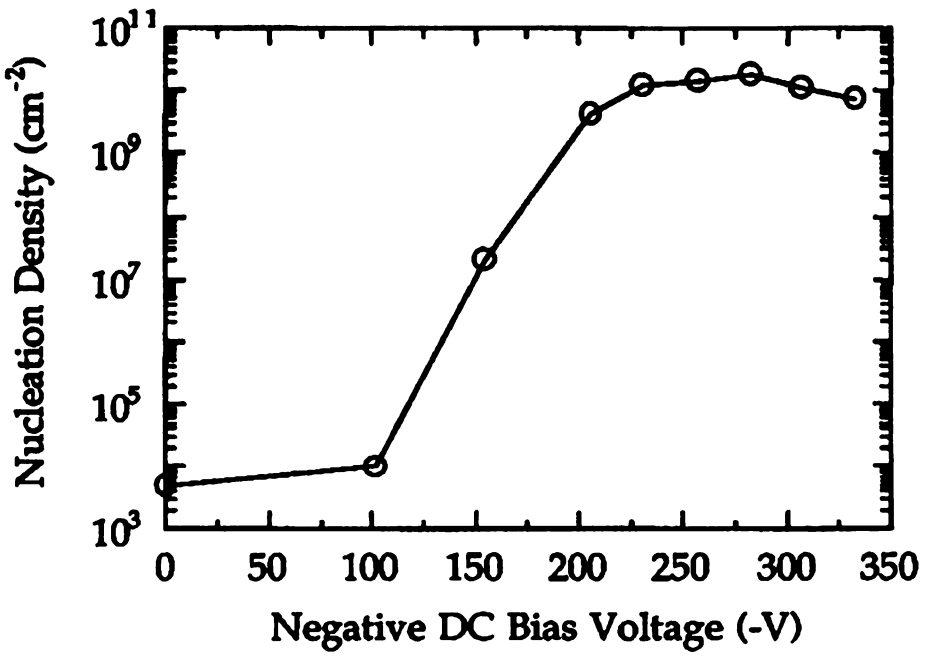

Figure 16 Plot of nucleation density for negative bias voltages keeping the time-integrated current constant for each data point *(105)*.

The nucleation density increased sharply above –100 V, and saturated above –210 V at a value that is five orders of magnitude higher than for 0 V bias. Low nucleation densities correlated with small increases in current, and this indicated the existence of a critical voltage for the onset of nucleation. Below the critical voltage, the impinging species are not energetic enough to overcome the nucleation barrier.

Sheldon et al. *(106)* used Electron Energy Loss Spectroscopy (EELS) and TEM to determine an amorphous carbon layer is deposited on the Si substrate during a –200 V BEN procedure. The deposit thickness, approximately 4 nm, was independent of the substrate temperature; suggesting the carbon was deposited through a non-chemical surface process. Ion energies of 2-20 eV were estimated. In other studies of OES during biasing at -150V, it was shown that atomic hydrogen increases near the substrate by more than 20% *(107)*. Atomic hydrogen is known to etch sp^2 carbon faster than sp^3 carbon

(108, 109), and it also has been found to stabilize sp^3 clusters *(110)*. The increase in atomic hydrogen directly above the substrate may have enhanced the carbon layer that formed due to hydrocarbon ion collisions. By stabilizing sp^3 clusters, it may also serve to increase the amount of amorphous carbon on the substrate that later nucleates diamond.

5.3.1.3 Ion bombardment increases surface diffusion

Jiang et al. *(88, 111)* studied the early growth stages of diamond on Si using SEM and AFM data, and postulated that surface diffusion of the carbon species on the substrate is increased due to ion-bombardment. First-nearest-neighbor distributions of particles imaged by AFM, for 10 minute and 12 minute bias times at a –150 V bias, showed distributions shifted to larger distances compared to a random (Poisson) distribution. They claimed a depletion zone develops around the nuclei and small just-forming islands. Therefore, the growth process induced by ion-bombardment of the substrate can be completely explained by thermodynamics. On the other hand, Ascerelli *(112)* concluded the depletion could be due to a deformation zone induced by the diamond-Si lattice mismatch. Jiang et al. however, reported that because the depletion zone is a function of bias voltage, ion-bombardment must influence the diffusion of the surface species *(88)*. Other studies have been done to show atomic diffusion is enhanced by ion bombardment during diamond BEN *(113)*.

5.3.1.4 Ion bombardment causes growth of a silicon-carbide buffer layer

Stoner et al. *(114)* studied the nucleation and growth of diamond on Si using XPS, AES, EELS (electron energy loss spectroscopy) and TEM. It was suggested that ion-bombardment enabled the formation of an amorphous-SiC layer (>9 nm) during the

first hour of biasing at –250 V in a MWCVD reactor. Further biasing developed an excess carbon concentration at the surface, which with continued ion bombardment could have become mobile on the surface and nucleated diamond. Other studies have shown that BEN on Si led to the formation of an epitaxial SiC layer, which nucleated oriented diamond crystallites *(115-118)*.

In a detailed study of bias nucleation, Stöckel et al. used MPCVD to investigate the ion-bombardment nucleation mechanism for diamond growth on Si *(118, 119)*. Their bias setup is nonstandard, as the (100) Si substrate is grounded, and a +250 V bias is applied to a tungsten electrode in the plasma *(120)*. By examining SEM and TEM images of the carbon deposits, the following 4-step model for nucleation was proposed: (1) In the first minutes of bias, nanocrystalline β-SiC forms on the Si substrate with a near epitaxial relationship. Simultaneously, the Si surface is etched by the H^+ flux in the plasma. (2) The β-SiC forms a closed continuous film after about 10 min at 10 nm thickness. This film is polycrystalline, but with an epitaxial relationship to the substrate. Excess carbon flux leads to a supersaturation of carbon in the SiC. Diamond nuclei form in the carbon layer, some with registry to the SiC. (3) Further biasing etches the β-SiC layer and exposes the diamond nuclei. (4) Growth conditions allow the diamond nuclei to grow – those with an epitaxial relationship grow as an oriented film.

5.3.2 Electron emission

Ion bombardment has been shown repeatedly to lead to enhanced diamond nucleation. However, the following experiments indicate it may not be the only mechanism at work, and some nucleation enhancement may be due to electron emission of diamond.

Stoner et al *(121)* studied the effects of a diamond coated substrate holder, an uncoated molybdenum substrate holder, and an alumina substrate holder during BEN. For the diamond coated holder they obtained high nucleation densities and a 5-fold increase in current during bias over the other two substrate holders. In addition, it was observed that: (1) the diamond coating on the holder surface is etched or removed during extended biasing (they don't indicate how long) leading to a decrease in bias current, (2) the plasma turned red near the surface of the sample and holder at increased voltages, indicating increased atomic hydrogen (H^0), and (3) nucleation began at the substrate edge and moved towards the center. The enhanced nucleation may be due to (1) a material transport mechanism, whereby diamond coated surfaces in the vicinity of the sample are etched and carbon is transported to the substrate and deposited, or (2) electron emission of the diamond surfaces causes increased levels of dissociated H_2 and/or hydrocarbons near the substrate. They noted that BEN experiments in a pure hydrogen plasma under the same conditions showed no increased nucleation, so the second explanation was more likely.

Wang et al. studied the mechanism for increased nucleation due to biasing using HFCVD *(122-124)*. The nucleation density was increased by one of two ways: applying a negative bias to the substrate, or to a circular diamond-coated tungsten ring 3-5mm above the substrate. In the second case enhanced nucleation arose from increased electron emission from the diamond-coated tungsten filament. The substrate is positive relative to the electrode in this case so the increased nucleation could not be due to increased positive ion bombardment. Chen et al. *(85)* also found that it is unnecessary for the substrate to be negatively biased in HFCVD. Nucleation densities were increased if a

diamo

while

BEN

For a

the Si

Nucle

cm^2 i

Witho

that n

the di

increa

incre

5.4

acco

prev

glow

durir

subs

HOD

the c

diamond coated filament was placed in the vicinity of the substrate and biased negatively while the substrate was held at a positive potential.

Perng et al. *(86)* studied the role of electron emission in biased MWPCVD. A BEN process was applied to micropatterned SiO_2/Si substrates and sapphire substrates. For a pattern of silicon dots 5 and 8 um in diameter, nucleation densities of ~10^9 cm^{-2} for the Si dots, and ~10^8 cm^{-2} for the SiO_2 masked areas were measured (via SEM). Nucleation (~10^8 cm^{-2}) and growth of diamond were also observed on the edges of a 1x1 cm^2 insulating sapphire substrate placed between four 1x1 cm^2 silicon substrates. Without the silicon substrates, the sapphire was only etched during bias. They proposed that nucleation is enhanced on insulating SiO_2 and sapphire due to electron emission from the diamond that was already formed on the Si in the vicinity. Electron emission increased the concentration of reactive species above the SiO_2 and sapphire, resulting in increased nucleation densities.

5.4 The secondary plasma

The deposition of high nucleation densities of diamond has often been reported accompanied by a bright secondary discharge during biasing. All the reports of the previous section, 5.3.2, discuss a bright blue, purple or red glow *(85, 86, 121-123)*. The glow always appeared either above the sample or the surrounding area of the holder during biasing, and the glow is related to diamond coatings on the substrate and/or substrate holder. Stoner et al. *(121)* pointed out that repeatability of bias-enhanced and HOD diamond results was a problem in early experiments, possibly due to differences in the coatings, and that it could be etched during biasing.

Biasing of the substrate affects the charge distribution in the plasma. As was described in section 3.4.1, mobile charged species in the plasma screen the discharge from an externally applied field forming a "sheath" region between the main discharge and the substrate. This will modify the conditions near the substrate and thus the nucleation process.

Schreck et al. *(76, 125)* provided evidence that biasing produces a plasma state that is a superposition of a microwave plasma and a DC glow discharge. They measured the intensity profile for the H_α Balmer emission line[6] during a bias of –200 V above a substrate (Figure 17).

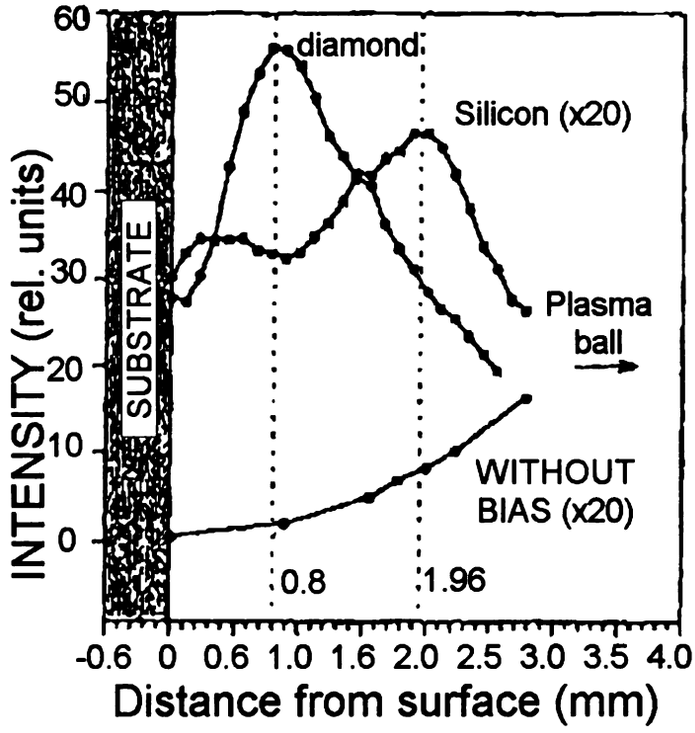

Figure 17 H_α Balmer line (λ=656.3nm) intensity measured above a diamond covered sample and a bare silicon sample biased at -200V, and a sample without an applied bias. Schreck et al. *(125)*.

[6] H_α emission/absorption line at λ=656.3 nm is the first atomic transition in the Balmer series. The Balmer series corresponds to atomic transitions that end in the first excited state of hydrogen (E=-3.4eV).

The intensity above an unbiased Si sample increased monotonically from the substrate into the main plasma discharge. With an applied bias, a peak in intensity appeared 1.95 mm above the Si substrate. The peak gained in intensity (x20) and shifted closer (0.8 mm) when the Si was covered in a diamond film. The profile of emission intensity was very similar to that near the negative electrode in a DC glow discharge (See Figure 13(b)). The maxima in intensities develop at voltages much lower than for a normal glow discharge because the microwave plasma contributes to the DC glow discharge. An I-V curve for the bias voltage on a graphite holder, a silicon substrate and diamond film covered Si substrate (Figure 18) was also reported. The first plateau was suggested to corresponded to positive ion saturation with the subsequent steep increase due to electron multiplication.

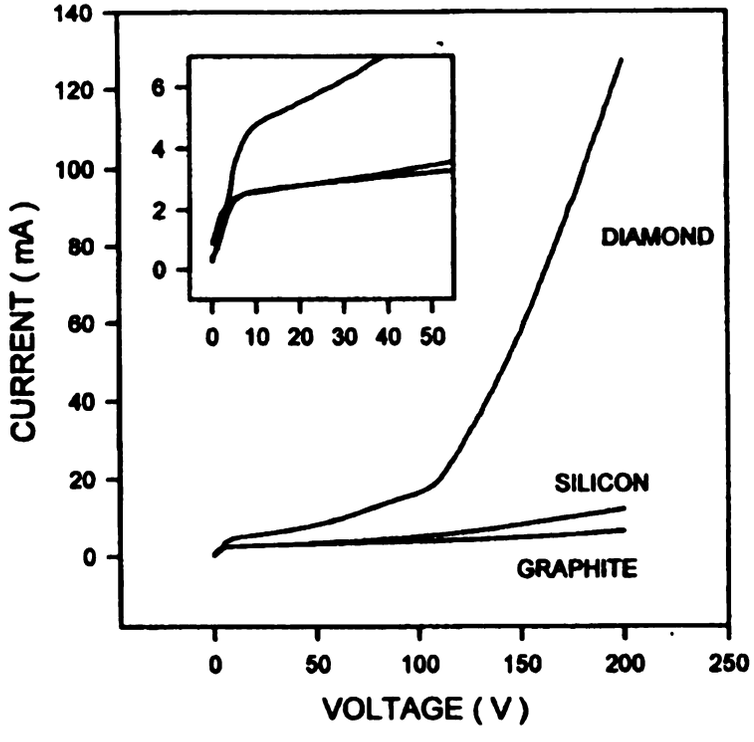

Figure 18 I-V curve for a diamond coated silicon substrate, a silicon substrate, and a clean graphite sample holder. Schreck et al. *(76)*.

It was proposed that the field in the secondary plasma (or the cathode sheath) accelerates the ions and electrons. The higher ion saturation curve for the diamond film compared to silicon or graphite means stronger ionization of the plasma *(76)*. The strong electron multiplication above diamond covered areas on the substrate may influence the plasma chemistry (cf. Stoner *(121)*) and may contribute to the nucleation on uncovered areas.

Kulisch et al. *(126)* reported a similar I-V characteristic for a microwave plasma CVD system (Figure 19). Others have suggested that the increase in current over the diamond covered substrate can be explained by enhanced secondary emission from diamond *(114, 127, 128)*.

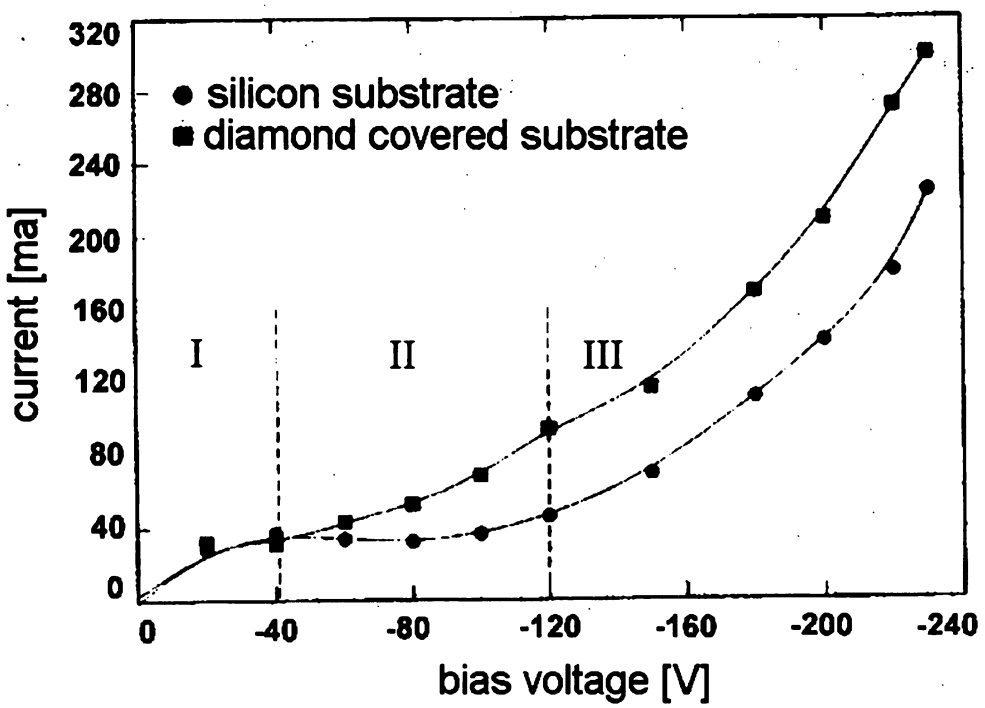

Figure 19 I-V plot for a bare silicon substrate and a diamond covered silicon substrate. Kulisch et al. *(126)*. Region I corresponds to a mobility limited current, region II to the saturation of positive ions at the surface, region III to current enhancement by additional ionization.

Although the shape of the I-V curve agrees with others *(76)* – the absolute measured

current and the time scale of I(t) (for a 30 minute bias period) were poorly reproducible. Two plausible reasons were given for this:

1. Current is strongly influenced by diamond surfaces in the substrates vicinity. This can vary due to relative sizes of the sample and holder, or the elevation of the sample with respect to the holder.
2. The respective volumes of the microwave plasma and the secondary discharge are easily influenced by small changes in the sample arrangement, geometry or quality of the diamond coating. The secondary plasma may change in volume and sample coverage during biasing. If the secondary plasma is the result of a normal glow discharge, then current changes would be apparent in changes of effective electrode area (including diamond coverage of the holder).

Other researchers *(129-131)* have carefully studied the secondary plasma emission during biasing and found similar emission spectra and I-V curves.

5.4.1.1 The secondary plasma and epitaxy

The cathode sheath or secondary discharge may play a role in the nucleation of heteroepitaxial diamond. Stöckel et al. observed a spatially inhomogeneous nucleation pattern, along with a secondary plasma sheath *(118, 119)*. The secondary plasma was initially localized over the substrate holder and advanced radially inwards over the substrate. This correlates with the nucleation front on the substrate. Taking advantage of the spatial inhomogeneity of the secondary plasma, they interrupted the bias process when the secondary plasma had advanced 1/3 of the way from the edge to the center. The sample was examined after nucleation, and after growing out half of the sample further. The mechanism proposed for epitaxial diamond nucleation was discussed in

section 5.3.1. Only over a region 1/3 to 1/2 of the way radially inward did they see oriented diamonds. It was concluded that the epitaxial growth occurs just ahead of the secondary plasma front and that epitaxial nucleation requires critical timing of the bias procedure.

Thürer et al. *(132)* studied the HOD nucleation and growth on Si using XRD to examine the linewidths of azimuthal scans of diamond{220} after growth as a function of bias voltage and bias time. For each particular voltage, azimuthal alignment of the diamond film was only possible within a certain bias time window. The final film alignment was determined during the biasing step. As the secondary plasma formation is a function of time, it is likely the two are related.

5.5 Biased enhanced nucleation on iridium

In contrast to Si, few studies have investigated the role biasing plays in the nucleation of diamond on Ir. The reports that do exist suggest the role may be quite different.

Ohtsuka et al. *(5)* conducted XPS on studies on biased Ir/MgO samples and found that no Ir-C compounds form during biasing. Instead an amorphous carbon layer deposits. It was suggested that the effect of biasing (or ion irradiation) is to roughen the Ir surface and deposit a thin amorphous carbon layer.

Hörmann et al. *(133, 134)* studied the effects of biasing on Ir/$SrTiO_3$ substrates with SEM and HRTEM. No evidence for an amorphous carbon interlayer was found on thin diamond film samples. It was pointed out that defect bands extended directly from the iridium into the diamond, which would not happen with an amorphous layer in between *(134)*.

Sawabe et al. *(135)* conducted cross-sectional HRTEM on diamond/Ir/MgO samples. Misfit dislocations and the diamond/Ir interface suggested to them a strong chemical bond between the Ir and diamond in these areas. They found no evidence for an interlayer, but significant roughening of the Ir surface during biasing. The roughened regions of the Ir were proposed to act as nucleation sites for diamond.

5.6 Summary

Differences in CVD reactors and experimental repeatability make it difficult to compare results among groups, or even experiments from the same researchers. However, it is clear that despite the disparity, ion bombardment is a vital component for BEN as shown by Robertson, Lifshitz, Jiang and others. But the observations of Stoner, Schreck and Kulisch, etc. leave little doubt that diamond covered surfaces affect the behavior of the plasma and thus the nucleation in a way that is poorly understood. Biasing effects on Ir substrates are less studied. The research in this work will show that nucleation on Ir is also strongly affected by ion bombardment and the biasing induced secondary plasma.

Chapter 6 Substrate preparation for diamond heteroepitaxy

6.1 Chapter overview

This chapter details the preparation of substrates for diamond deposition. The substrate is a critical component in heteroepitaxial growth. Highly ordered diamond (HOD) can be grown on (001) Si substrates; (001) Ir is used as a substrate for growth of single crystal diamond. The discussion of epitaxial Ir deposition comprises the bulk of this chapter. Ir is not available as a high quality, single crystal substrate, so we first deposit it epitaxially on another substrate. We have used (001) $SrTiO_3$, (001) MgO, (001) $LaAlO_3$, and $(11\bar{2}0)$ Al_2O_3 as underlying substrates for single crystal (001) Ir deposition using UHV electron beam deposition. A brief review of other Ir epitaxy studies is given, and the structure and preparation of (001) $SrTiO_3$ and $(11\bar{2}0)$ Al_2O_3 are discussed. In both cases, the goal was to obtain smooth, terraced surfaces for the deposition of single crystal Ir. The epitaxy of Ir on $(11\bar{2}0)$ Al_2O_3 is not yet fully understood due to the complex structure of the $(11\bar{2}0)$ surface, and the differing geometries of the lattices. We suggest a possible epitaxial relationship of Ir on a-plane Al_2O_3. The UHV electron-beam evaporation system used for all Ir depositions is described and results of studies on the Ir morphology and crystalline quality evolution

with

diam

6.2

It al

(00

cher

(14

film

rela

C s

sp

S

S

with temperature and thickness are presented. The preparation of Si substrates for diamond deposition is straightforward, and is only briefly discussed.

6.2 Substrate preparation for iridium deposition

Ir has a high melting point (2454 °C), and low vapor pressure (1.47 Pa at 2443°C). It also has a high surface energy for a metal, with a theoretical value of 3.81 J/m^2 for the (001) surface *(136)*. Ir thin films have been prepared previously by metalorganic chemical vapor deposition (MOCVD) *(137-139)*, radio-frequency magnetron sputtering *(140)*, pulsed laser deposition *(141, 142)* and e-beam evaporation *(143)*. Epitaxial Ir thin films were first demonstrated on sapphire in 1994 using MOCVD *(137)* with an epitaxy relation of $(100)_{Ir}||(11\bar{2}0)_{Al_2O_3}$ with $<011>_{Ir}||\langle 1\bar{1}00\rangle_{AL_2O_3}$, for iridium deposited at 600° C substrate temperature. For subsequent diamond growth, Ohtsuka et al. used magnetron sputtering to deposit epitaxial (001) Ir films onto cleaved (001) MgO surfaces. *(5)*. Schreck et al. demonstrated epitaxial Ir deposited via e-beam evaporation onto (001) $SrTiO_3$ *(7, 8)*. In the course of our work over the last three years, we have deposited single crystal (001) Ir onto polished (001) $SrTiO_3$, (001) MgO, (001) $LaAlO_3$, and a-plane Al_2O_3 using e-beam evaporation. Each of these surfaces requires preparation before single crystal Ir can be grown. The major portion of the work described in this thesis is on $SrTiO_3$ and Al_2O_3, so discussion in this chapter is limited to these two. It should be noted that preparation of MgO and $LaAlO_3$ substrates is similar to $SrTiO_3$.

6.2.1 Strontium titanate substrate preparation

$SrTiO_3$ is a cubic perovskite (space group Pm3m), with a melting point of 2080° C, commonly used in oxide superconductor growth. The unit cell and lattice TiO_2 terminated structure are pictured below.

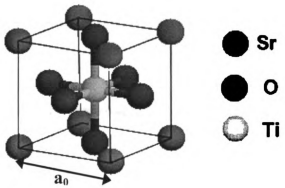

Figure 20 $SrTiO_3$ unit cell. a_0 = 0.39050 nm

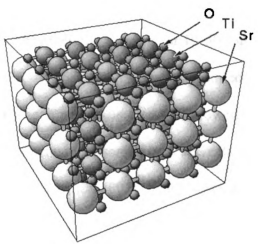

Figure 21 $SrTiO_3$ structure with TiO_2-terminated surface.

It has lattice parameter a_0=0.39050 nm, a 1.7% mismatch to fcc Ir. The two structures are similar, so Ir deposits epitaxially on $SrTiO_3$ with the relation $(100)_{Ir}||(100)_{SrTiO_3}$ and $[110]_{Ir}||[110]_{SrTiO_3}$. 1x1x0.5 cm^3 substrates were coated with photoresist and cut into 0.5x0.5 cm^2 pieces using a wire saw. They were inspected for defects under an optical

microscope after ultrasonic cleaning in acetone and methanol for 10 mintues each, followed by a rinse in DI water. Figure 22 shows a typical surface after cleaning.

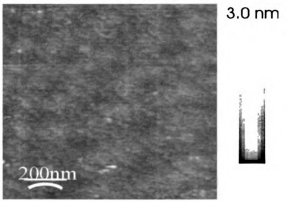

Figure 22 $SrTiO_3$ surface AFM scan after ultrasonic cleaning for 10 minutes each in acetone and methanol, followed by DI water rinse.

Substrates that did not pass inspection due to pits, scratches or defects were returned to the supplier. Terraced, atomically flat, TiO_2-terminated surfaces were prepared by standard methods *(144, 145)*. They were first etched for 10-60 s in a buffered pH 4.5 hydrofluoric solution (NH_4F:HF = 87.5:12.5). Higher pH resulted in rough surfaces, a lower one in etch pits. A two hour anneal in flowing O_2 followed in a tube furnace at 950° C. They were then again cleaned ultrasonically in solvents before being loaded into the UHV system for Ir depositon. A typical (001) $SrTiO_3$ surface is shown in Figure 23.

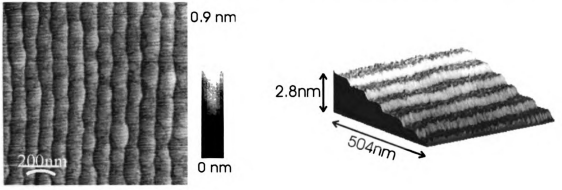

Figure 23 AFM image and 3D profile of typical $SrTiO_3$ surface after surface preparation. Mean roughness = 0.2 nm.

After annealing the surface was covered in terraces across the surface, with a mean roughness of 0.2 nm. The mean step height of the surface in Figure 23 is 0.42 ± 0.03 nm, which is within error of the lattice parameter of $SrTiO_3$, indicating these are single atomic steps.

6.2.2 A-plane sapphire substrate preparation

Sapphire has a hexagonal crystal structure and belongs to the space group $R\bar{3}c$. It has lattice constants a=0.476 nm, c=1.299 nm, and a melting point of 2040°C. The crystal structure of α-Al_2O_3 is a hexagonal close-packed arrangement of O^{2-} anions, with two-thirds of the octahedral voids occupied by Al^{3+} cations *(146)*. The structure is stable and standard processing leads to terraced, defect-free surfaces. We have used both small offcut angle (<0.1°) with <1 nm roughness $(11\bar{2}0)$ Al_2O_3 substrates for Ir deposition and more typically supplied substrates of this orientation with offcut angles of up to 0.5° and rms roughness of 5-8 nm. The substrates were coated with photoresist, cut and cleaned following the same procedure as strontium titanate. They were also inspected under the optical microscope for defects or pits. The samples that passed inspection were annealed, in air, at 1450° C for 15 hours. This leads to terraced surfaces, as shown in Figure 24.

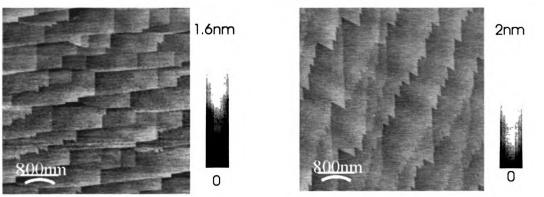

Figure 24 Representative AFM images of two different a-plane Al_2O_3 substrates.

The above figures show two different Al_2O_3 samples. The morphology of the a-plane surface after annealing may depend on the offcut angle of the substrate and the direction of the miscut, which is unknown in Figure 24. The roughness of both samples is <0.2nm.

Epitaxy of Ir on α-Al_2O_3 is not straightforward because of the dissimilar lattice structures. The a-plane of Al_2O_3 is perpendicular to the c-plane <0001> direction. It is the lengthwise, diagonal cross-section of the unit cell (Figure 25).

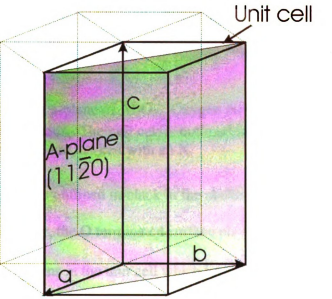

Figure 25 Schematic of sapphire structure, unit cell, and orientation of (11$\bar{2}$0) plane. a=b=0.476 nm and c=1.299 nm. The c-axis is aligned along the <0001> direction.

The unit cell of Al_2O_3 has lattice parameters c=1.299 nm, a=b=0.476 nm. The arrangement of aluminum and oxygen atoms on the (11$\bar{2}$0) plane is shown in Figure 26.

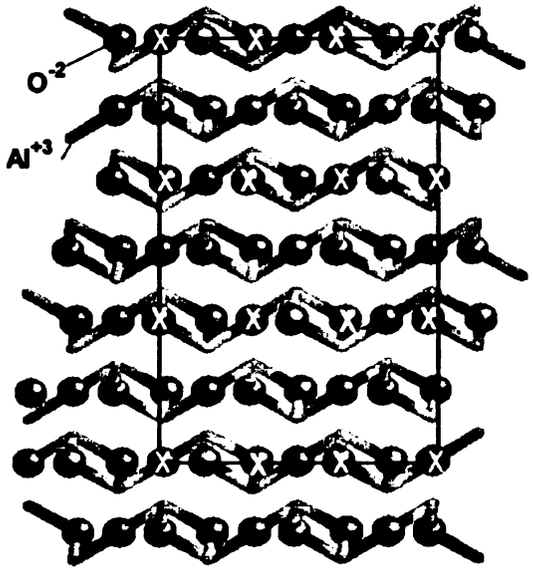

Figure 26 Surface of $(11\bar{2}0)$ a-plane of Al_2O_3. Oxygen atoms are depicted as spheres, aluminum atoms as rods. The unit cell is outlined in black. Oxygen atoms that lie in the same plane, are marked with an X.

The projection of the unit cell is outlined in black in the above figure. We believe, that similar to GaN/sapphire epitaxy, the O terminated surface plays a role in Ir epitaxy on the $(11\bar{2}0)$ plane *(147, 148)*. O atoms in the unit cell which lie in the same plane are marked with an "X" in Figure 26. Figure 27 shows the suggested (001)Ir epitaxy on the O atoms.

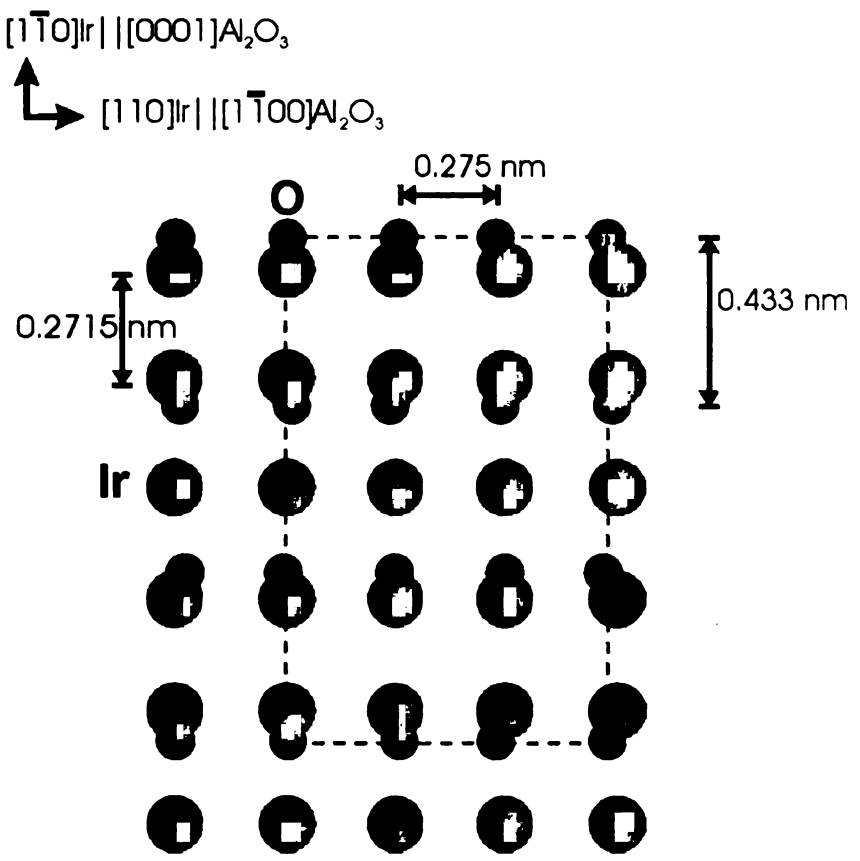

Figure 27 Possible epitaxial relationship of (001) Ir on $(11\bar{2}0)\,Al_2O_3$. The dotted box indicates the unit cell in the $(11\bar{2}0)\,Al_2O_3$ plane projection.

The distance between oxygen atoms for this surface is 0.433 nm along the <0001> and 0.275 nm along the $\langle 1\,\bar{1}\,00\rangle$ directions. When the (001) Ir plane is superimposed with $<110>_{Ir}||\langle 1\,\bar{1}\,00\rangle_{Al_2O_3}$, the lattices match 3:2 in the $\langle 1\,\bar{1}\,0\rangle$ ||<0001> directions with a 11% mismatch, and 1.2% in the $<110>||\langle 1\,\bar{1}\,00\rangle$ directions.

6.3 E-beam iridium deposition

Ir single crystal films are deposited using ultra high vacuum (UHV) electron beam evaporation *(75)*. The main chamber base pressure is 5 x 10^{-10} Torr, pumped with an ion pump and a titanium sublimation pump. The load lock is evacuated after sample loading

using a turbo pump backed by an oil-free diaphragm roughing pump to a pressure of 10^{-7} Torr. The system has two water-cooled electron guns in the main vacuum chamber. The power supply can maintain a total current of 660 mA to the guns. 99.9% Ir slugs in Cu crucibles were evaporated with a focused electron beam with current between 300-400 mA. A 1" diameter resistive heater mounted on the sample puck heats the sample to the deposition temperature, as measured by a thermocouple mounted to the top of the sample holder. A crystal thickness monitor measures the deposition rate.

6.3.1 Procedure on strontium titanate and sapphire

The substrates are loaded into the UHV chamber of the e-beam evaporation system through the load-lock immediately after solvent cleaning and drying in a nitrogen gas flow. The substrate heater is turned on and in 30-40 minutes reaches deposition temperature of 800° C. The shutter is opened, and the Ir deposited at a rate of 0.3-0.5 Å/s to a total thickness of 150-300 nm. A 150 nm Ir film takes about 1 hr to deposit. Upon removal, the films are examined with AFM and X-ray diffraction.

6.3.2 Description of iridium growth mechanism on strontium titanate and sapphire

Ir growth initiates on $SrTiO_3$ and Al_2O_3 in the 3-D island growth mode (Volmer-Weber). The films coarsen as the thickness increases. Eventually a continuous film forms, and 2-D layer-by-layer growth can proceed. We have demonstrated this with the followings studies on the evolution of the crystalline structure and morphology of Ir.

6.3.3 Structure and morphology of Ir films on $SrTiO_3$

Epitaxial Ir is deposited on $SrTiO_3$ provided the substrate temperature is above 450° C. The morphology of the film is dependent on temperature and thickness. A 150 nm film evaporated at 800° C had the X-ray diffraction pattern shown in Figure 28.

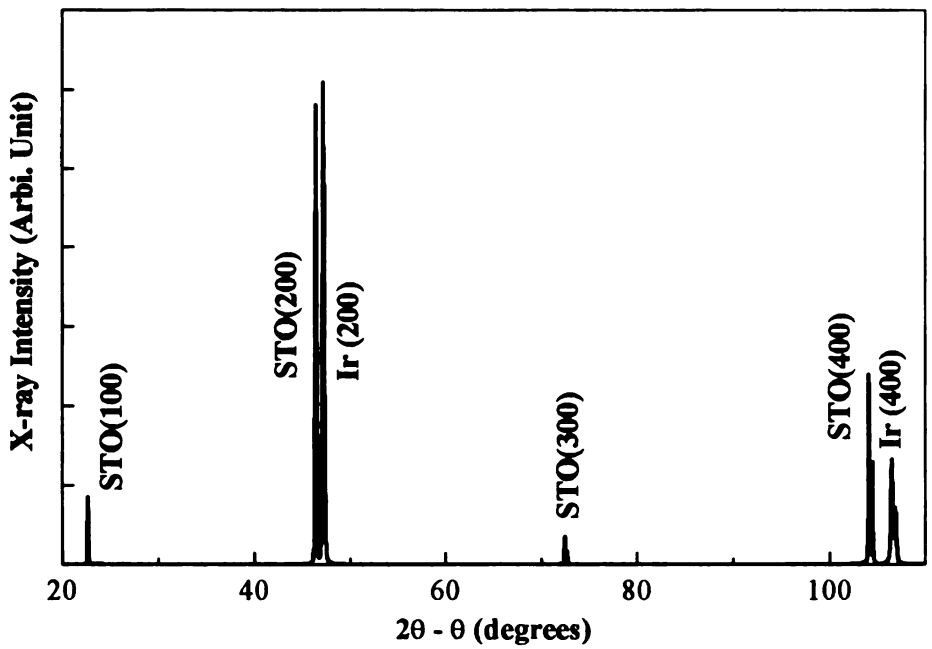

Figure 28 X-ray 2θ-θ scan of Ir on $SrTiO_3$ using Cu Kα radiation. Film was 150 nm thick, grown at substrate temperature of 800°C.

Although the (111) Ir reflection has a relative intensity about twice that of the (200), the 2θ-θ scan above does not show any evidence of (111) Ir, indicating the film consisted entirely of (100) Ir. The linewidths of the (200) $SrTiO_3$ and (200) Ir reflections are calculated by a Gaussian fit to the experimental data, and are 0.03° for $SrTiO_3$ and 0.19° for Ir, as shown in Figure 29.

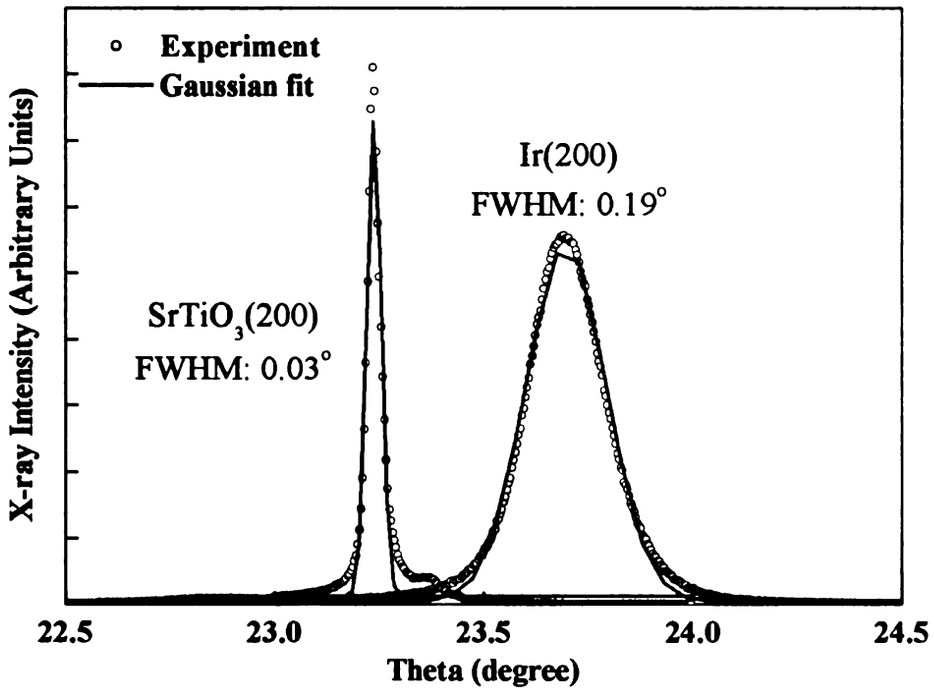

Figure 29 The Gaussian linewidth extracted from a least-squares fit to the data: 0.03° for (200) $SrTiO_3$ and 0.19° for (200) Ir.

By comparison, Hörmann et al. have reported a rocking curve linewidth of 0.15° for the (200) Ir peak for a 200 nm Ir film deposited at 950° C on $SrTiO_3$ *(133)*. Presumably the value is somewhat better due to a thicker film deposited at a higher temperature, and differences in instrument resolution.

Morphology of the Ir was studied using AFM for different thicknesses of Ir. Ir was deposited in the same manner for each run, at a substrate temperature of 800° C. Representative AFM scans are shown in Figure 30.

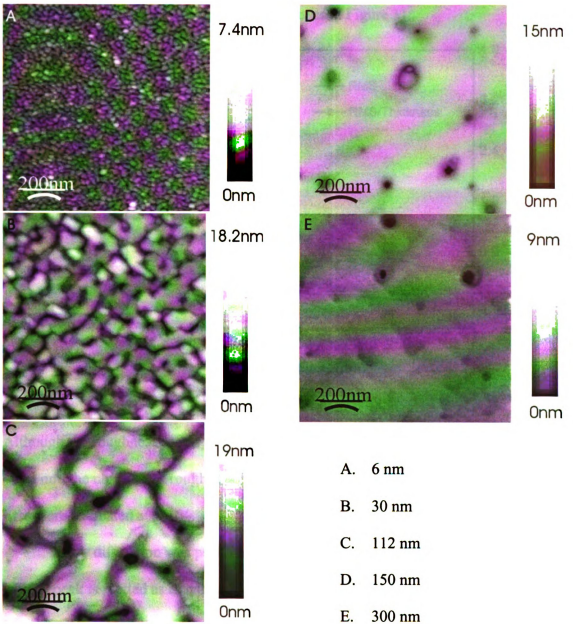

Figure 30 1x1 μm^2 area AFM images of Ir on $SrTiO_3$

Small islands emerged initially then coarsened as the film thickness increases and eventually coalesce. At 150 nm thickness, the film is completely coalesced, only some pinholes remain on the surface. At 300 nm the pinholes are mostly filled in, and the film appears to grow layer-by-layer, a 2-D growth mode. The pinholes that remain have been determined by AFM not to extend through to the substrate. The rms roughness of the

above Ir films is plotted against the film thickness in Figure 31.

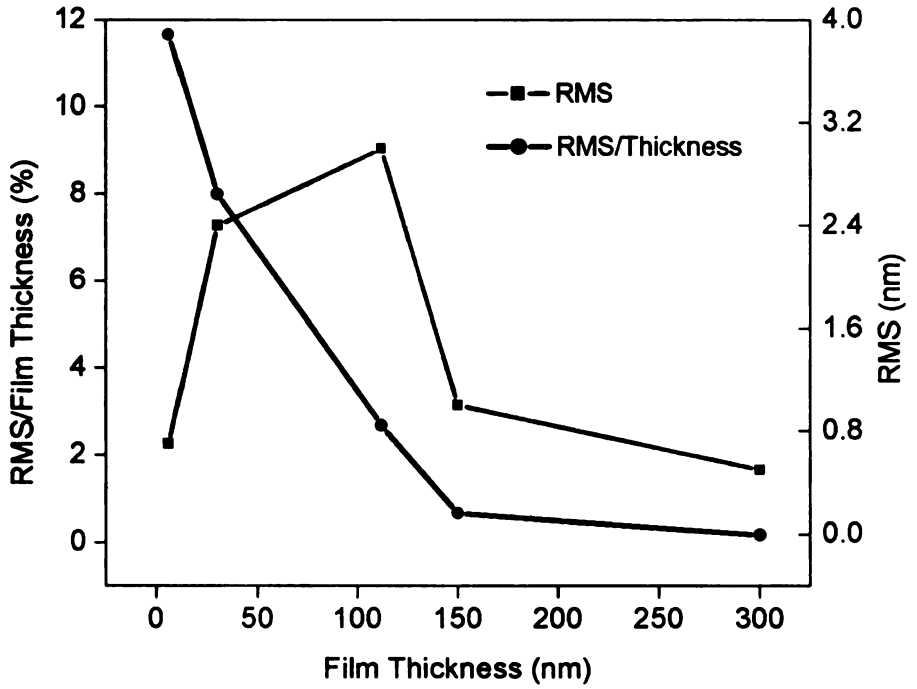

Figure 31 Ir roughness vs. substrate thickness measured from 1x1μm AFM scans.

Although the roughness seems to increase with increasing film thickness for thickness <150 nm, the normalized roughness falls off with increasing thickness, then stabilizes. Errors are estimated at ±10%.

X-ray diffraction was performed on these films as well. The linewidth of the Ir(200) peak is plotted as a function of thickness in Figure 32.

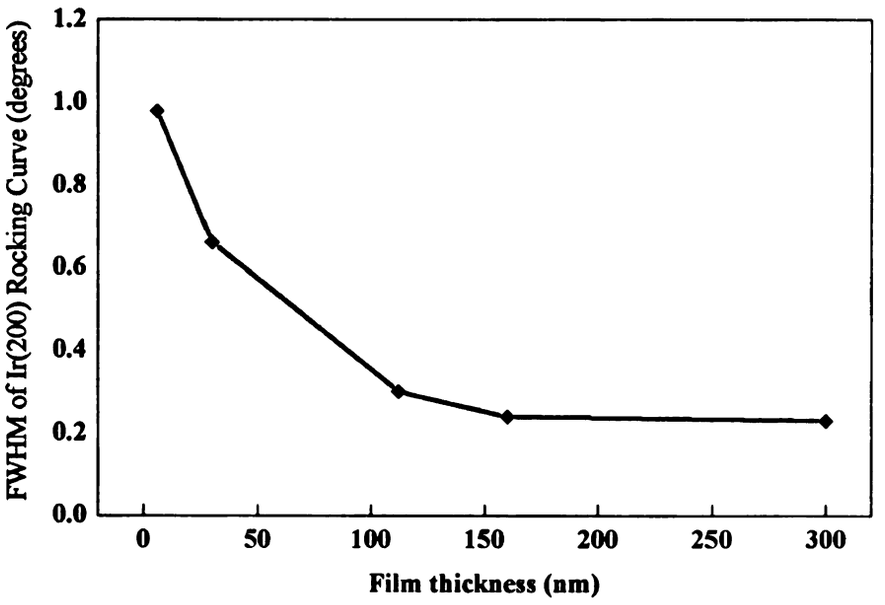

Figure 32 X-ray analysis of Ir (200) vs. film thickness.

The peak width narrows with increasing film thickness, in agreement with other results *(133)*. It reaches a value of 0.19° for 150 nm, and then remains constant.

6.3.4 Temperature dependence of iridium morphology on $SrTiO_3$

The evolution of surface morphology and crystalline quality of Ir:$SrTiO_3$ substrates was also studied as a function of substrate deposition temperature. 150 nm Ir films were deposited in different runs with substrate temperatures from 450° C to 800° C. The morphology was studied using AFM, and the crystal structure using X-ray diffraction analysis of the (200)Ir peak. The AFM images are shown in Figure 33.

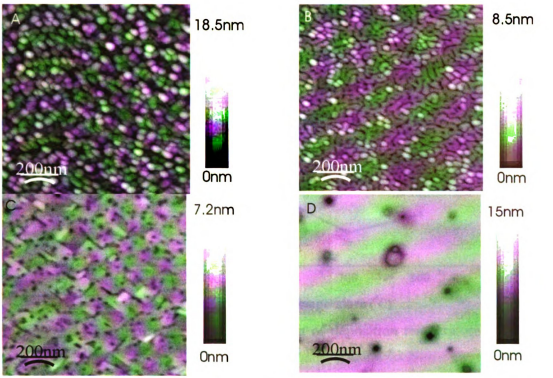

Figure 33 1x1 μm AFM scans of Ir on $SrTiO_3$ deposited at different substrate temperatures. All films are 150 nm thick. A. 450° C, B. 600° C, C. 700° C, D. 800° C

At 450° C, the film grows in 3-D mode, indicated by the discreteness of the features. Films deposited at higher temperatures, 600° and 700° C, show monotonically increasing island size. At 800°C a continuous film forms. The film also becomes smoother as deposition temprature increases. A plot of average surface roughness with depositon temprature is shown in Figure 34.

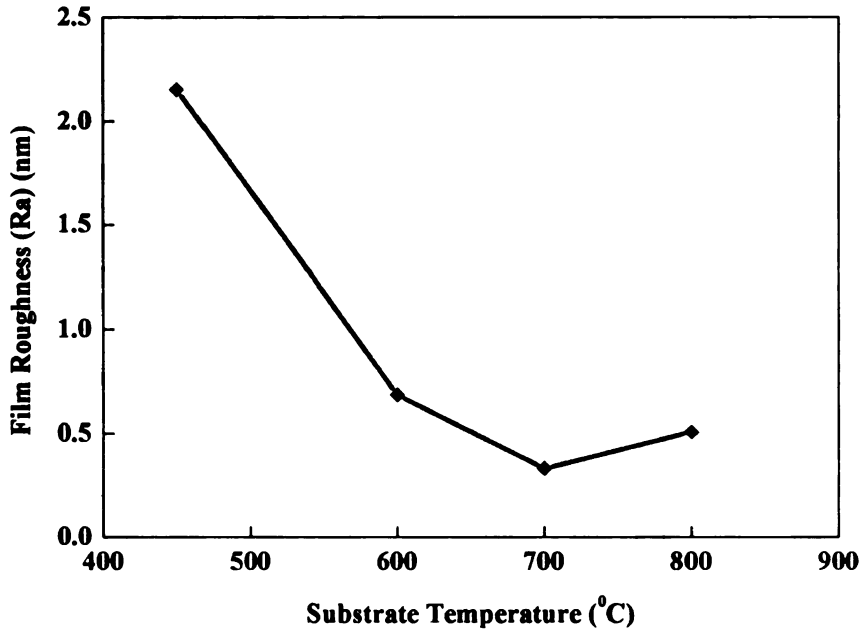

Figure 34 Iridium roughness as a function of deposition temperature. All films are 150 nm thick. Measurements made with AFM.

Roughness decreases with increasing substrate temperature. It increases slightly at 800°C again – due to the agregation of pinholes on the surface. The linewidth of the Ir (200) peak decreases with increasing substrate temperature, as shown in Figure 35. The crystalline perfection increased with increased deposition temperature.

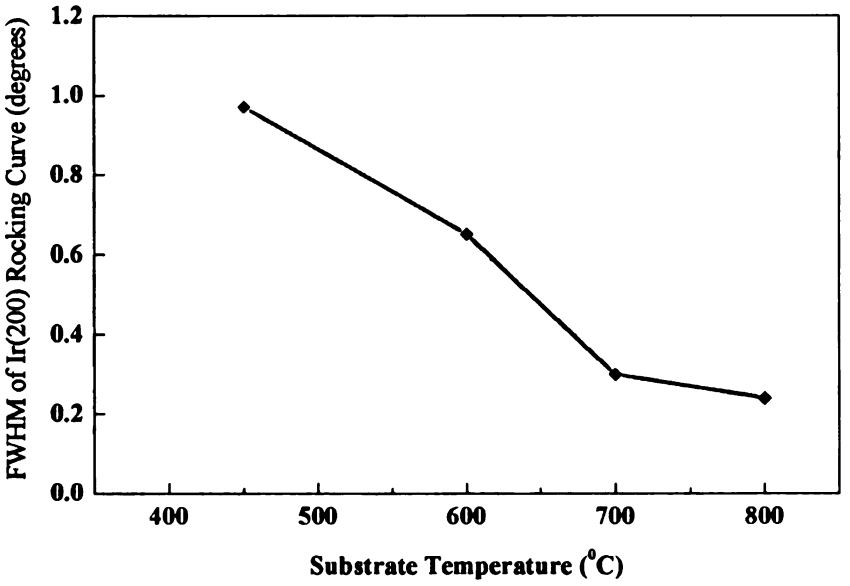

Figure 35 X-ray rocking curve width of Ir (200) as a function of substrate temperature.

6.3.5 Morphology and structure of iridium films on $(11\bar{2}0)\,Al_2O_3$

A 300 nm Ir film deposited at 800° C on $(11\bar{2}0)\,Al_2O_3$ with e-beam evaporation had the x-ray diffraction rocking curves shown in Figure 36.

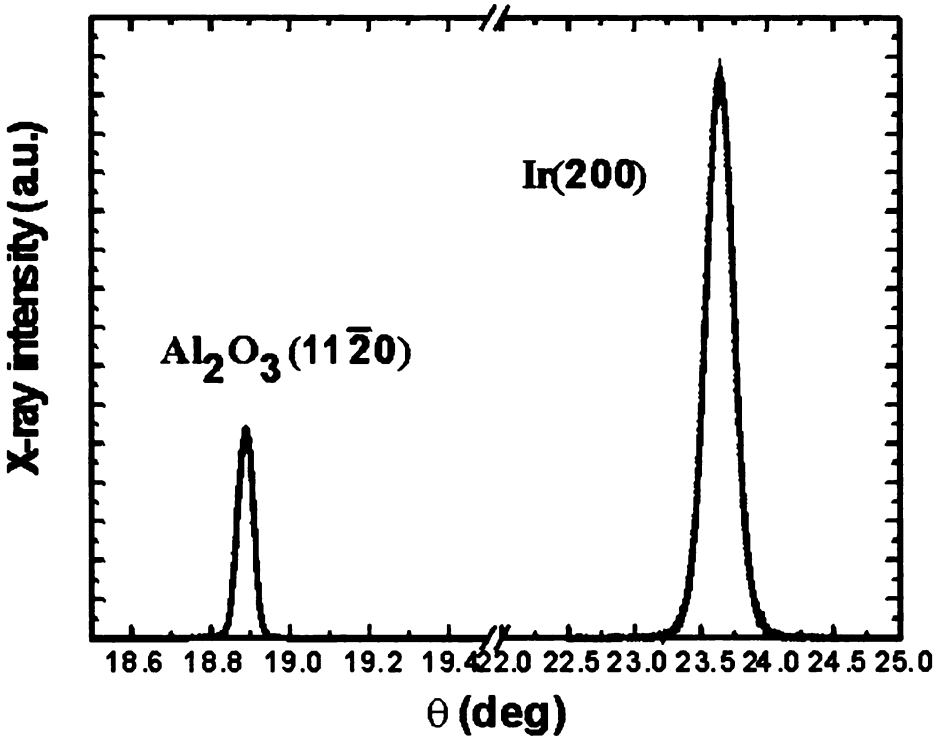

Figure 36 X-ray diffraction rocking curves for 300 nm epitaxial Ir grown on $(11\bar{2}0)$ Al_2O_3. Linewidths: sapphire, 0.04° ; iridium, 0.21°.

The sapphire linewidth is 0.04° and the Ir 0.21°, comparable to that of Ir on $SrTiO_3$ (Figure 29). The morphology and crystalline quality of the iridium films on A-plane sapphire also varied with temperature and thickness. Both (100)Ir and (111)Ir epitaxy are possible on $(11\bar{2}0)$ Al_2O_3. (100)Ir epitaxy occurs at substrate temperatures of 700°-800° C during e-beam deposition with the epitaxial relation $(001)_{Ir}\langle 110\rangle_{Ir}\|(11\bar{2}0)_{Al_2O_3}$ $\langle 1\bar{1}00\rangle_{Al_2O_3}$. For lower temperatures, we observed $(111)_{Ir}\|(11\bar{2}0)_{Al_2O_3}$. The epitaxy of the Ir may also be dependent on the direction and/or the angle of the offcut on the Al_2O_3 substrates. The morphology of the cleaned, etched and annealed surface is shown in

Figure 37 before and after after Ir deposition. The Ir film was 300 nm thick and deposited at 800° C.

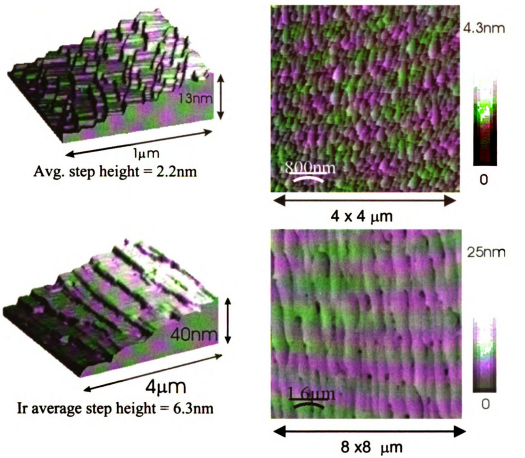

Figure 37 AFM scans of $(11\bar{2}0)$ sapphire substrate before (upper) and after (lower) (001)Ir deposition. Ir thickness = 300 nm. (Sample 02042002).

The surface of the Al_2O_3 is irregularly terraced after the annealing treatment. The average step height is 2.2 nm and the RMS roughness 0.6 nm. After Ir deposition the surface displayed a surface with terraces and mean roughness 1.7 nm.

6.3.6 Backside coating

$SrTiO_3$, Al_2O_3 and the other oxides used are electrically insulating. For biasing, it was assumed necessary to have a conducting path from the Ir to the rest of the biased stage. $SrTiO_3$ can be made conductive by heating it in vacuum at 750° C in contact with

the stainless steel sample holder. This may be due to oxygen reduction, which results in a conduction carrier enhancement *(133)*, or a chemical reaction between the oxide and the metal. However, the method was not reliable, as the backside resistance varied for each sample, from less than $100\,\Omega$ to a few $k\Omega$. This also did not work as well for the other oxide substrates. Sapphire is particularly stable, and remained highly insulating after heat treatment. To obtain reliable backside conductivity on all samples, we deposited a 100-150 nm coating of Ir on the backside and one edge using a tilted sample holder designed for this purpose.

6.4 Silicon preparation

We have used Si substrates early in our studies to investigate the effects of changing sample holder geometry on current density (Chapter 8). The 3" (001) p-type Si wafers used as substrates had well-polished single crystal surfaces with few defects. They were coated with photoresist to protect the surface, then cut with a dicing saw into 1 or 2 cm squares. The individual samples were marked on the backside, and then cleaned in a solvent rinse with acetone and methanol for 10 min each in an ultrasonic bath. For bias-enhanced experiments, no other surface preparation was necessary. The samples were placed in the CVD reactor, and subjected to a 10 min hydrogen plasma cleaning prior to adding CH_4 to remove the native oxide *(149-151)*. We determined that lengthening or shortening this step by as much as 5 min did not affect nucleation densities.

6.5 Summary

Single crystal substrates of high quality are required for the deposition of single crystal diamond. This chapter mainly discussed the preparation of Ir films on $SrTiO_3$ and Al_2O_3. Terraced, low roughness surfaces of (001) $SrTiO_3$ and $(11\bar{2}0)$ Al_2O_3 substrates were prepared using a combination of cleaning, chemical etching and annealing at high temperatures. We deposited single crystal (001) Ir on these surfaces using UHV electron beam evaporation. The morphology and crystalline structure of Ir on $SrTiO_3$ was studied with AFM and X-ray diffraction as a function of substrate temperature and film thickness. High quality smooth (001) Ir films with X-ray linewidths of 0.19° and 0.21° for $SrTiO_3$ and Al_2O_3 substrates respectively, were achieved. The epitaxial relationships are $(001)_{Ir}<110>_{Ir}||(001)_{SrTiO_3}<110>_{SrTiO_3}$ and $(001)_{Ir}<110>_{Ir}||(11\bar{2}0)_{Al_2O_3}\langle 1\bar{1}00\rangle_{Al_2O_3}$. The epitaxy relation between (001) Ir and $(11\bar{2}0)$ Al_2O_3 was studied and a possible matching of the two lattices suggested.

Chapter 7 Microwave plasma chemical vapor deposition of diamond

7.1 Chapter overview

This chapter presents details of the experimental setup for CVD diamond growth. The microwave plasma reactor is described, and modifications made to the sample holder of the system for biasing experiments are discussed. Finally the procedure for heteroepitaxial diamond nucleation and growth on iridium are given. Results of biasing and growth experiments are given in the following chapters.

7.2 Chemical vapor deposition system

Diamond growth is carried out in a microwave plasma CVD reactor based on a design by Asmussen *(152)*. A schematic diagram of the reactor is shown in Figure 38.

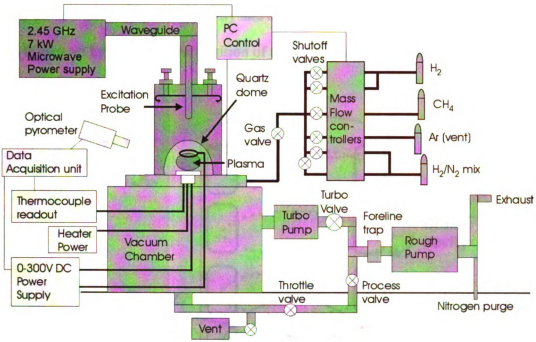

Figure 38 Microwave plasma CVD diamond reactor system

The system consists of: (1) a 2.45 GHz microwave source with a 7 kW magnetron power supply, a rectangular wave guide, a cylindrical brass cavity and an excitation probe; (2) a gas handling system for a stainless steel vacuum chamber outfitted with ports for feedthroughs and gauges, a quartz dome, mass flow controllers and a pumping system; (3) a PC control system that monitors system pressure, microwave input and reflected power and allows timed experiments; and (4) biasing and stage temperature monitoring circuits with a data acquisition unit.

7.2.1 Reactor and vacuum chamber

The system comprises a quartz bell jar type reactor that confines the plasma and reactant gases to a quartz dome in the vacuum chamber. The reactor is fed with a 2 m long rectangular waveguide from a Cober 2.45 GHz 7 kW model SF6 microwave power source to a cylindrical brass microwave cavity. An adjustable brass excitation probe

extends down from the top of the cavity and allows excitation of the modes. The cavity length is also set by adjusting the position of the sliding short. The excitation mode is TM_{013}, shown in Figure 39.

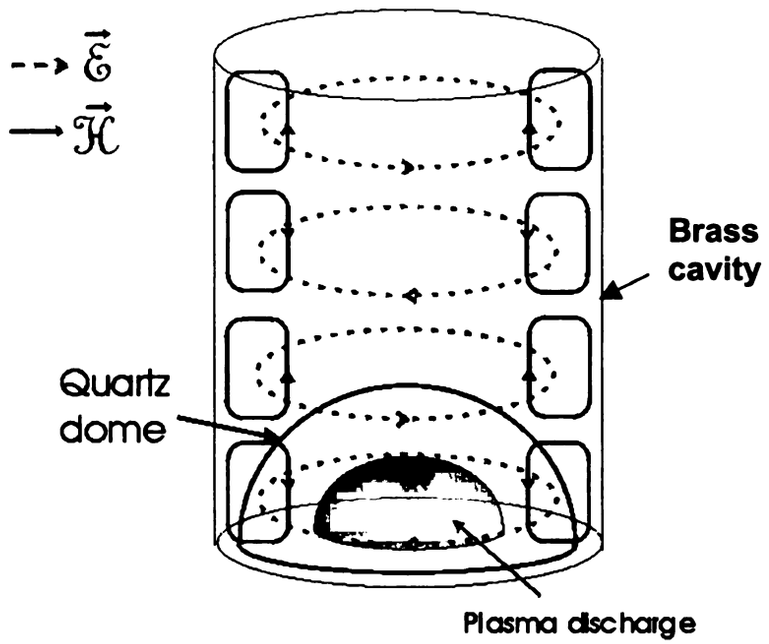

Figure 39 TM_{013} Electromagnetic mode of reactor cavity.

In TM_{013} mode, the electric field lines circle the inner perimeter of the cavity, and the magnetic field lines consist of four toroids evenly spaced on the vertical axis. This gives the plasma a hemispherical shape. The quartz dome sits inside the brass cavity as shown in the cross-sectional schematic in Figure 40. Positioned within the dome is the stage and sample holder.

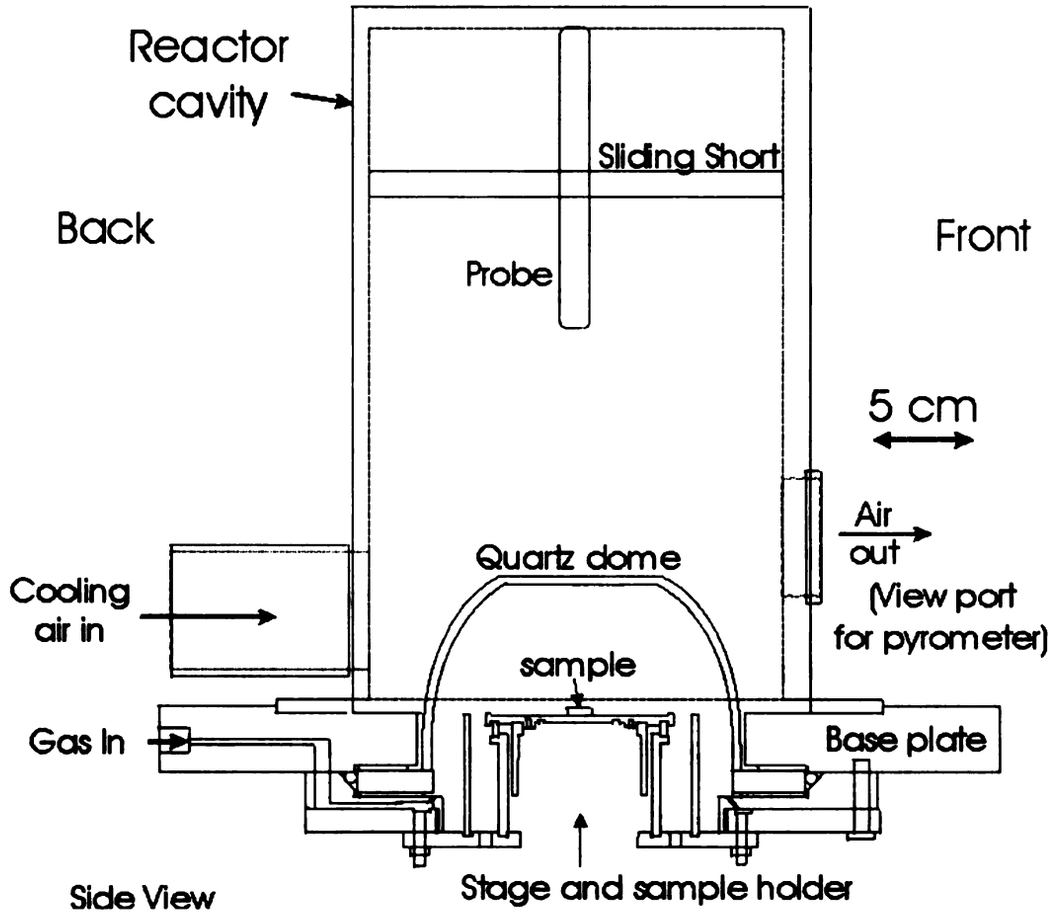

Figure 40 Cutaway scale drawing of CVD reactor. The base plate rests on the vacuum chamber.

With the ionization of the reactant gases directly above the sample holder, a plasma forms. The quartz dome and stainless steel platform that holds the Mo sample holder sit above a vacuum chamber that has a residual gas analyzer, ion gauge, pumping system (turbomolecular pump and roughing pump), gas handling system and electrical feedthroughs for thermocouple, stage biasing, and heater connections. The entire sample stage is removable, and is bolted to the baseplate of the vacuum chamber, so that the sample sits flush with the base of the cavity.

The reactor cavity and baseplate are cooled using a closed loop cooling system with lines running through the baseplate around the cavity base, and through the probe.

A Neslab chiller model CFT-300 with a 5 gallon capacity is set to 29° C when the system is running.

7.2.2 Gas handling

The gas handling system consists of a vacuum chamber, pumped by a water cooled Alcatel model 5150 turbomolecular pump backed by an Alcatel Model 2021 CP roughing pump. The pump reduces the system base pressure to the mid 10^{-8} Torr range. The system does not have a load lock for sample loading. After a sample is loaded, the system is pumped for a minimum of 4 hr to reach a base pressure $<5x10^{-7}$ Torr. Residual gases then consist of water and nitrogen ($<10^{-9}$ Torr) as measured by a residual gas analyzer (RGA). Gases are mixed in the line after coming through the flow controllers and fed into the system through a single inlet valve. The process gas feeds into a gas distribution plate with 8 symmetric angled 0.04" holes around the base of the stage, allowing for even gas flow into the bell jar. The gas is pumped out through eight 0.25" symmetrically placed holes at the base of the stage plate. This is referred to as a forced flow configuration. A MKS type 653 throttle control valve and MKS type 651C pressure controller with 0-10 Torr and 0-100 Torr baratron pressure transducers regulate the pressure to within 0.1 Torr of the setpoint. Exhaust gases are purged with compressed nitrogen at the outlet of the rough pump and exhausted through the building exhaust handling system. Each cylinder has a gas line to the inlet valve with a manual shutoff valve after the flow controller to prevent leakage of unwanted process gases into the system while the main gas valve is open, and also for leak checking the lines. The system has dedicated lines for CH_4 (99.999%), H_2 (99.9995%), Ar (99.999%), and N_2/H_2 gas mixes. It is vented using 99.999% Ar to minimize nitrogen contamination of the

system walls. The process tanks are regulated at a line pressure of 150 psi, the small N_2/H_2 bottles at 30 psi. Gas lines are flushed and leak-checked, and the vacuum system is baked out with heat tape when a process gas tank, or the quartz dome is changed.

7.2.3 Modifications for biasing

We modified the sample holder and stage to carry out experiments on biased nucleation and growth of diamond. A new stage was designed to include an electrically floating sample platform and holder, as shown in Figure 41.

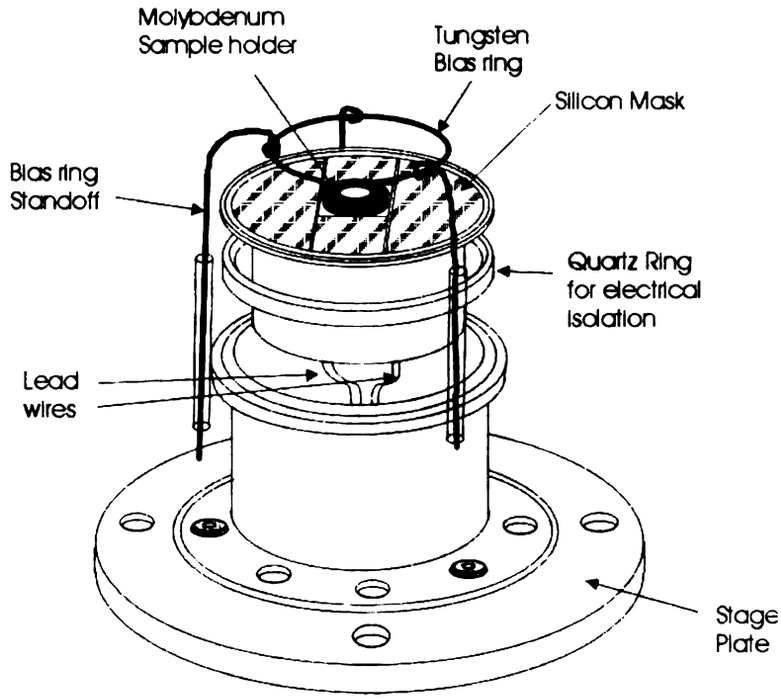

Figure 41 Exploded view of CVD stage and sample holder setup.

The stainless steel sample platform is electrically isolated from the stage by a 0.25"x 2.75" OD ring of fused quartz. A K-type thermocouple is mounted on the underside of the stainless steel platform. A 1.5" substrate heater can also be mounted underneath, but was not used for the experiments in this thesis. The original design of the sample platform was for a 3" Si wafer. Due to geometry constraints, the top surface area of the

platform has to remain fixed for the TM_{013} mode to remain stable in the reactor cavity. We found that by electrically masking the area of the platform surrounding the 0.8 cm Mo sample holder, we obtained a high current flux through the sample area during biasing. Here, the sample holder and platfrom are at a negative 100-300 V potential, while the rest of the stage remains grounded. The sample holder geometry relevant to the nucleation of heteroepitaxial diamond is described in detail in section 8.3.3.

A Kepco DC power supply, model BOP 1000M, capable of 0-300V/0-200mA provided the bias potential. Two 50 Ω, 5W resistors were connected in series with the power supply on both the positive and negative terminal. The schematic bias circuit diagram is in Figure 42.

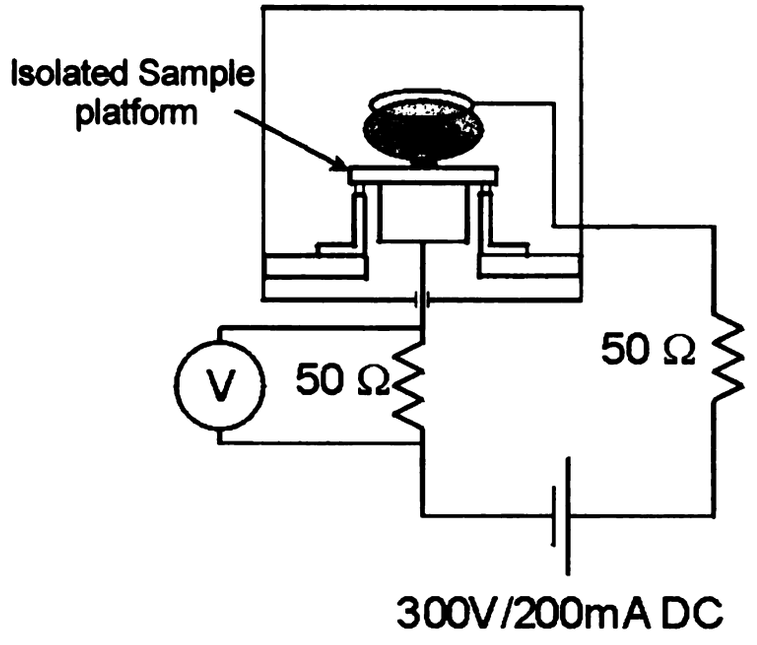

Figure 42 Circuit for bias setup.

Under certain biasing conditions, we observed arcing: the plasma was unstable and sent electrical feedback to the power supply during biasing. The resistors served two

purposes: to help dissipate feedback spikes from the plasma to the power supply, and to provide a means for measuring bias current. A circular electrode immersed in the plasma, connected by three standoff wires to the base of the stage, provided electrical contact to the plasma. The plasma circuit had a resistance of 3-5 $k\Omega$. The return path for the bias current is through the plasma and the bias circuit was only complete with a plasma ignited.

7.2.4 Computer operation

The system is operated with a computer interface to control an experiment. Input parameters are gas flow rates, system pressure, microwave input power, and duration of experiment. The program records incident and reflected power and pressure fluctuations at one-minute intervals. A separate computer running as a PC data recorder, with a Fluke Hydra data acquisition unit, records the substrate temperature from the thermocouple, pyrometer and bias current. The main system PC monitors chamber pressure, and reflected and incident microwave power, checking they are within preset safety parameters. It also has control of the pneumatic process (roughing pump) and main throttle valves. The system can operate unattended for the preset experiment time. However, adjustment of gas pressure and flow must be done manually when growing heteroepitaxial diamond.

7.3 Operation procedure

Microwave plasma chemical vapor deposition is a complex process with many variables. Some variables, such as pressure, microwave power, gas flow and mixture, bias voltage and timing, can be independently controlled. Temperature and bias current,

however, are highly dependent on pressure, geometry, bias voltage and, to a lesser extent, microwave power. Finding optimal parameters for diamond growth with such a large parameter space is not trivial. After each run, the sample was examined and characterized using optical microscopy and/or SEM and sometimes AFM, Raman microscopy or X-ray diffraction. In most cases, experiments in which only one parameter varied were attempted. We conducted more than 250 CVD runs on Ir/oxide substrates and at least half as many on Si substrates. To keep track of the experiments on Ir/oxide, we constructed a database. For each run, the input parameters of each step were recorded (microwave power, gas pressure and flow, time and bias voltage), as well as bias current and temperature readings of the pyrometer and thermocouple. This was entered into a spreadsheet along with information about the substrate, pre-experiment reactor conditions and geometry, and hyperlinks to files containing SEM images and the data recorded by the system computers. From the spreadsheet, individual datasheets for each experiment were made using a script that presents the relevant data in a one page format for easy reference. The spreadsheet allowed us to quickly sort runs that were made under specific conditions, and find the relevant data for them. We can, for example, find all runs that had a 60 min bias at –150V followed by 60 min growth, and compare data from different runs.

7.3.1 Procedure for heteroepitaxial diamond growth on iridium

The following is an abbreviated procedure for heteroepitaxial diamond growth on Ir. Growth of diamond on Si followed a similar procedure, with modified parameters.

7.3.1.1 Loading the sample

Samples are loaded into the CVD reactor in a Mo sample holder, resting on a platform that sits on a removable stage. After a sample is placed on the Mo post, a Mo cap is placed on top of the sample. The cap serves a three-fold purpose: (1) it keeps the sample held in place during loading; (2) it masks any exposed oxide substrate, so that the plasma only sees an Ir surface, and (3) it provides an electrical contact to the Ir. The stage with the sample is loaded into the vacuum chamber and bolted into place in the reactor. The chamber is pumped to 4×10^{-7} Torr, as measured by an ion gauge.

7.3.1.2 System startup, hydrogen cleaning, carburization and bias procedure

After pumping down, the ion gauge and RGA are shut off, and the turbo valve closed. The pressure setpoint is set to 15 Torr. The turbo pump is turned off and the roughing valve and gas valves opened. H_2 flows into the vacuum chamber at 300 sccm. At 10 Torr, the microwave power supply is manually turned on and set to 1 kW. The ignition of the plasma at 10-12 Torr and 500 W of microwave power define t=0. At t=2 min, the microwave power is ramped up to 1.5 kW. It takes approximately 4-6 min for the system to reach the pressure setpoint of 15 Torr. This stage of the procedure is called the "hydrogen cleaning" step. At t=5min, the methane flow controller is turned on allowing 6 sccm of methane to flow into the system, and the pressure setpoint increased to 18 Torr. The plasma is allowed to stabilize for 12 min. This step is called the "carburization" step. At t=16 min the bias power supply is turned on. At t=17 min, the voltage control is turned on, and the bias voltage ramped up to –150 V over 20 s. After the bias time, the voltage is ramped down to zero over 10 s. The power supply is left on,

with the voltage set at 0 V. This leaves the stage at a slightly positive potential with respect to the plasma.

7.3.1.3 Growth step

After the bias is stopped, the CH_4 flow is set at 3 sccm. For growth times of three hours or less, no other parameters are changed, and the microwave power is shut off after turning off the methane channel for 1 min. For longer runs, after 1.5 hr, the pressure is increased incrementally, and the methane flow rate further reduced. After turning off the microwave power at the end of the run, the gas valve is closed and the throttle valve opened fully, allowing the system to immediately pump down. This minimized deposition of non-diamond carbon during the cool-down phase. The system is allowed to cool, and the sample removed.

Chapter 8 Heteroepitaxial nucleation of diamond

8.1 Chapter overview

This chapter describes major advances in the implementation of high density diamond nucleation on epitaxial Ir grown on $SrTiO_3$ and a-plane sapphire substrates. The first part, presenting early work on nucleation on (001) silicon substrates, introduces the CVD reactor geometry and general operating parameters. We then discuss the geometry and CVD conditions needed to initiate nucleation on (001) Ir. To obtain a high nucleation density on Ir, we focus on several critical issues: temperature, bias voltage/current density, the sample holder, and overall geometry. Although the initial starting CVD parameters for growth of diamond on iridium were similar to those for growth of diamond on Si, we discovered that Ir degraded during processing. This led to a systematic investigation of the effects of pressure, microwave power, bias voltage and sample geometry on temperature. Furthermore, the environment near the growth surface profoundly influences the nucleation. The secondary plasma that appears above the substrate during biasing is also vital to nucleation. The second half of the chapter describes the evolving morphology of the carbon condensate during the biasing process, and the initial stages of diamond growth on Ir. We use a number of quantitative measures of the initial crystallite spatial distributions: 2-D Fourier transforms and radial density plots give us statistical information on the distribution of crystallites on Ir.

8.2 Role of bias current density

The first biased-enhanced nucleation experiments were carried out on 3" dia. Si wafers. An alternative arrangement was an array of four 0.5 x 0.5" Si samples centered on a 3.5" diameter Mo sample holder. Typical results are shown in Table 7.

Run ID	*Bias (Volts)*	*Current (mA)*	*Sample size*	*Nucleation Density*
04-Feb-00	-150	110	0.5" square	10^4-10^9
09-Feb-00	-200	340-400	0.5" square	10^{11}
10-Feb-00	-200	280-500	3" round	10^{11}

Table 7 Diamond nucleation on Si. All runs had a 15 min bias duration, 32 Torr, 3 kW microwave input power, 6 sccm methane in 300 sccm hydrogen. For 09-Feb-00 and 10-Feb-00 runs the current rose continuously during biasing.

In some runs, the current increased with time at constant bias voltage. Although the nucleation density approached 10^{11} cm^{-2} for high voltage and currents, we realized that higher nucleation densities across the entire sample would require higher currents than possible with available power supplies. We surmised that higher current densities would allow us to maintain a secondary plasma while increasing nucleation densities.

A square Mo sample holder, 2x2 cm^2 was designed to replace the 3.5" Mo holder for 3" dia. wafers. To increase the current density, we devised a mask to shield the stainless steel sample platform, reducing the total current while increasing the current density at the sample. The mask was made from a 3" Si wafer diced into 4 pieces as shown in Figure 43.

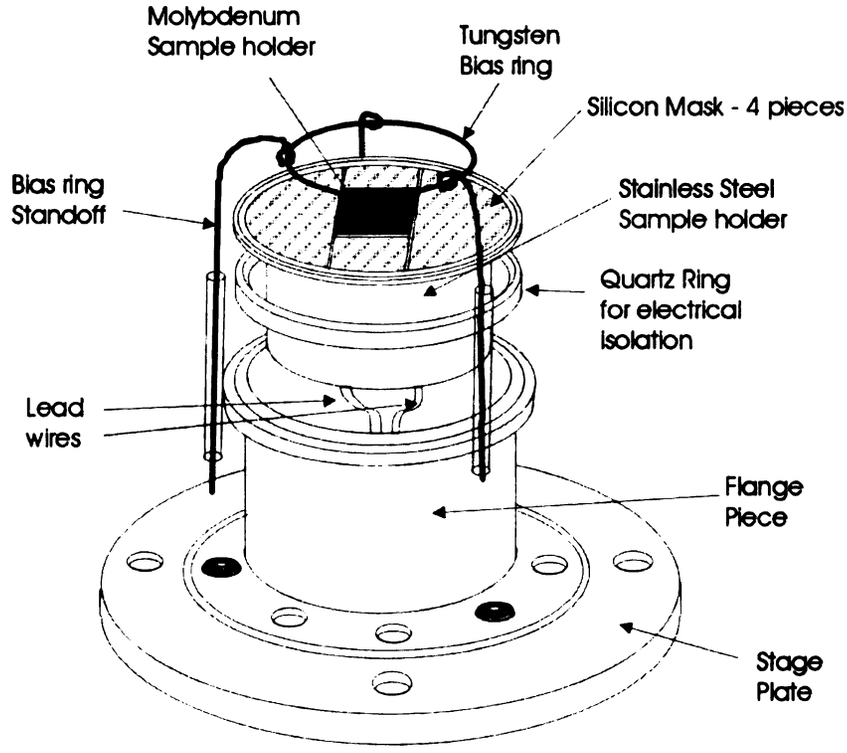

Figure 43 Sample holder, sample platform and bias stage with Si mask and 2x2 cm^2 Mo sample holder.

The silicon mask surrounded, but did not contact, the 2 cm Mo sample holder. It was electrically isolated from the stainless steel platform by 1 mm thick slabs of fused quartz. The Mo holder was 1 mm above the Si mask.

Table 8 shows the results of these changes. The total current was significantly reduced while maintaining high nucleation densities.

Run ID	*Bias (Volts)*	*Current (mA)*	*Sample size*	*Nucleation Density*
12-Feb-00	-200	50-120	2 cm square	10^{10}-10^{11}
15-Feb-00	-150	35-40	2 cm square	10^{4}
18-Feb-00	-200	50-120	2 cm square	10^{10}-10^{11}

Table 8 Data from experiments carried out using the sample configuration in Figure 43. Sample data on silicon comparing bias voltage, current and nucleation density. All runs had a 15 min bias duration, and were carried out at 32 Torr, 3 kW microwave input power, 2% CH_4 in 300 sccm H_2. Current is rising during biasing.

Assuming that all current flows through the sample, the current densities were I/A=7-13 mA/cm^2 (run 09-Feb-00) before masking, as compared to 13-30 mA/cm^2 (run 18-Feb-00) after masking. The total current decreased, but the current density increased. This configuration allowed us to achieve current densities high enough to obtain nucleation densities of 10^{10}-10^{11} cm^{-2} across the entire sample. After biasing, we then grew diamond on Si. We successfully grew highly oriented diamond films on 2 cm square (001)Si wafers (Figure 44).

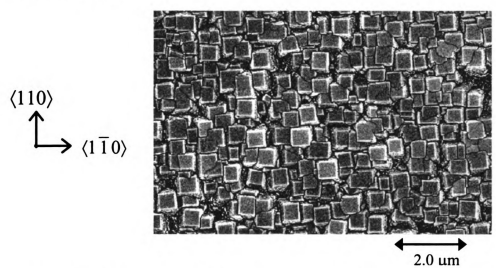

Figure 44 Highly ordered diamond grown on (001)Si. The crystallite faces are (001) but there is appreciable misorientation so that good coalescence does not occur. Bias: –175 V, for 5 min at 32 Torr, 2% CH_4 in H_2; 3 hr growth time.

8.2.1 Arcing during biasing

The arrangement described above was not rigid and the mask and Mo holder could be inadvertently moved while loading into the vacuum chamber. This led to arcing during biasing. Charge build up along the edges of the silicon mask could discharge to the Mo holder or the stainless steel platform. Arcing also occurred due to carbon deposits building up on the stainless steel platform, or poor contact between the molybdenum holder and the stainless steel platform. This was reflected in large current spikes in the I(t) profile (Figure 45).

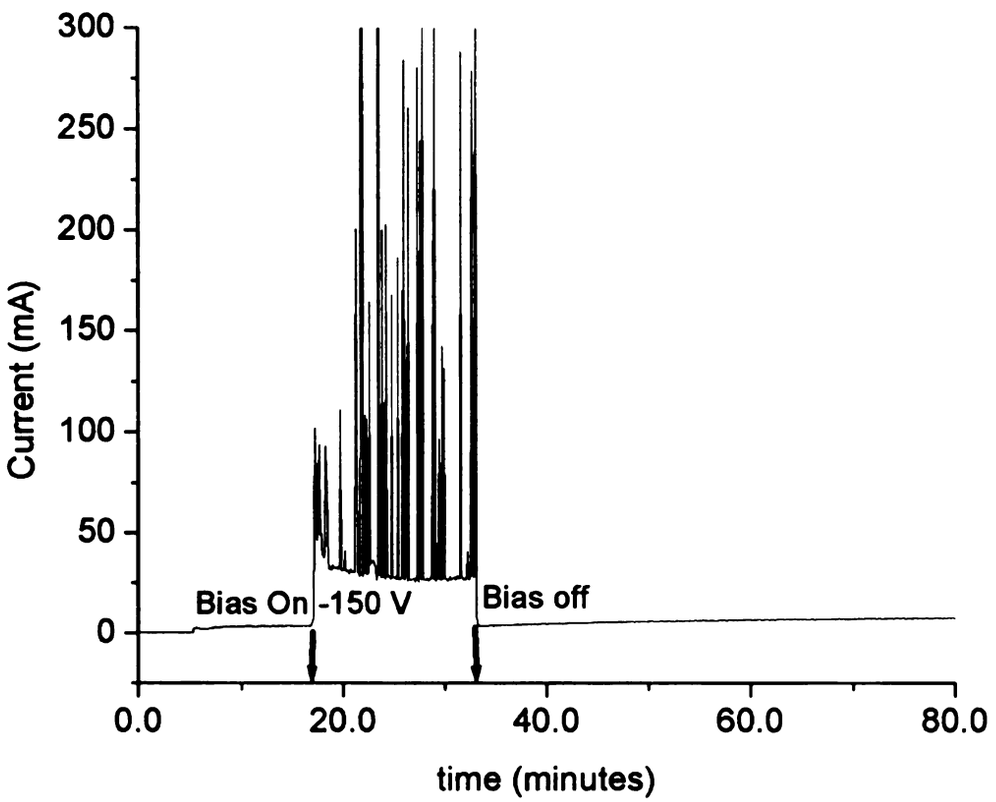

Figure 45 I(t) profile for biasing on Si (22-Apr-00). Bias: -150V for 16 min at 32 Torr, 2.2kW input MW power, 1% CH_4 in H_2, 150 ppm N_2.

The current spikes corresponded to bright "flashes" across the sample, or around the sample holder. Arcing, as well as low total current levels during the bias period, led to

inhomogeneous nucleation across the sample and growth of highly twinned polycrystalline diamond.

A new configuration was designed to solve these problems. A Mo sample holder to hold 0.5 x 0.5 cm^2 Ir/oxide substrates (Figure 46) consisted of a round 0.8 cm post screwed into the stainless steel platform, to insure good electrical contact. A Mo cap rested on top of the substrate and enveloped the post. The Si mask was cut with a 1 cm hole in the center, and the mask was supported and held in place by three alumina pegs spaced symmetrically around the edge of the mask. Round geometry was chosen to eliminate corners or sharp edges, and to keep with the symmetry of the rest of the system.

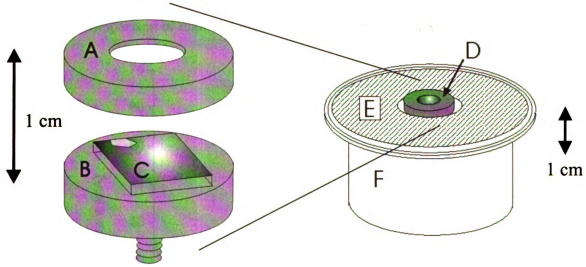

Figure 46 Illustration of the Mo sample holder and arrangement on the stainless steel platform. A is the Mo sample cap, B, the sample post, C, the sample. Right figure shows holder D (consisting of A,B,C) screwed into stainless steel platform F, and Si mask E. The cap leaves a 3.5 mm region of the Ir exposed. The alumina support pegs under the Si are not shown.

The Mo cap served to make electrical contact with the Ir, and also to shield any oxide left exposed by incomplete iridium evaporation.

8.3 Improving bias conditions

For Ir/oxide substrates, the CVD conditions are compared to those used for HOD on Si in Table 9. The current-voltage behavior is shown in the I-V curve of Figure 47.

Substrate	Ir	Si (for HOD)
Microwave Power	2.2 kW	2.2 kW
Pressure	32 Torr	32 Torr
Gas mix (%CH_4 in H_2)	5% CH_4, 150ppm N_2	1% CH_4, 150 ppm N_2
Bias	-250 V	-175 V
Bias time	10 min	4.5-10 min
Ring height	16 mm	16 mm

Table 9 Comparison of diamond growth on Ir with growth on Si.

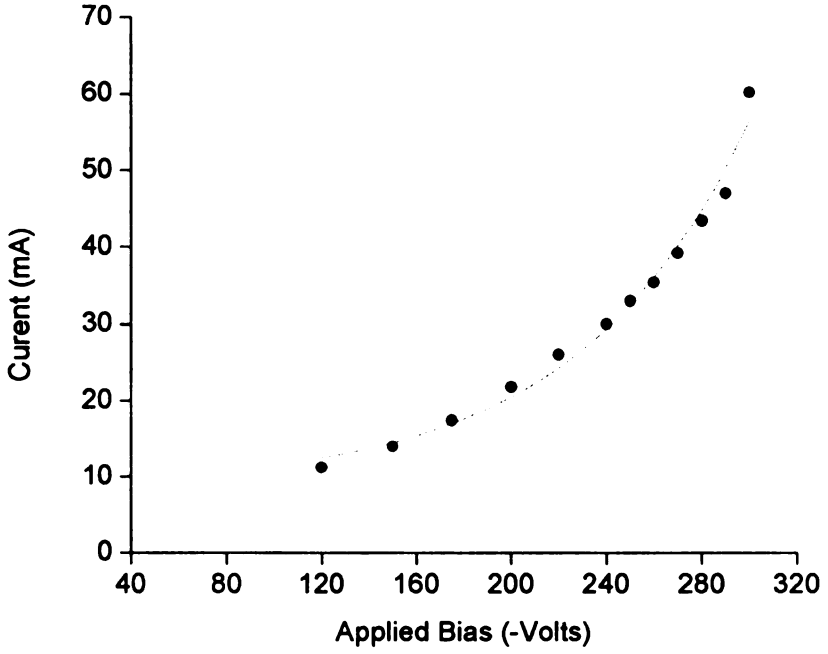

Figure 47 I-V of round cap geometry with Ir/oxide substrate. Line is a guide to the eye. 2.2 kW input MW. 32 Torr, 5% CH_4, 16.5 mm ring height.

At –280 V, a bright secondary glow appeared over the iridium sample and the Mo cap edges. Initially we tried bias and growth parameters similar to those used for HOD on Si. A higher voltage (-250V) was used to attain current densities to sustain the secondary plasma.

We were able to obtain nucleation densities of 10^9 - 10^{10} cm^{-2}. However, we noted heavily twinned diamond and Ir damage that could have resulted from the ion bombardment or the high temperature. During biasing, the temperature rose to 870°-930° C whereas Ir deposition took place near 800-850^0 C.

We then carried out experiments in which the bias voltage was varied from –250 to –150 V. Heavily twinned diamond was still observed; changing CH_4 concentration also had little effect. The effects of gas pressure and microwave power and bias voltage on temperature were then studied, with results shown in Figures 48 - 50 below.

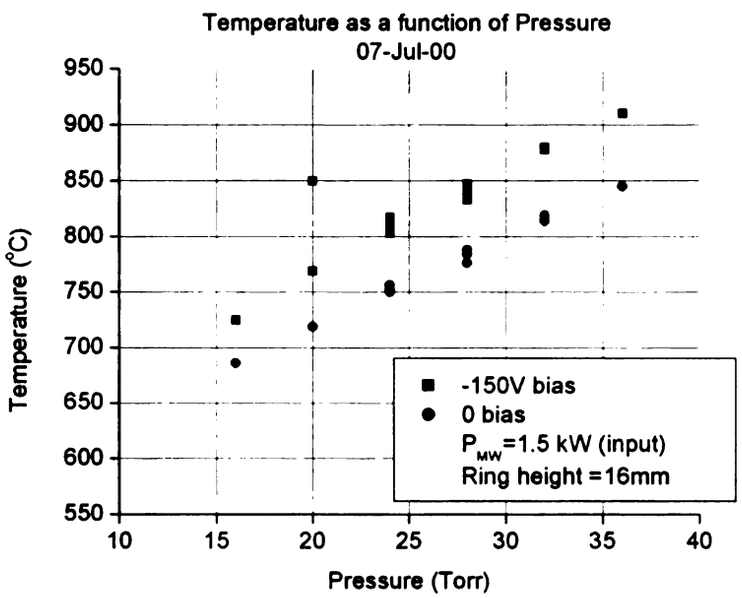

Figure 48 Temperature vs. pressure at -150V bias and 0V bias. Temperature is measured with an optical pyrometer focused on the Mo cap surface.

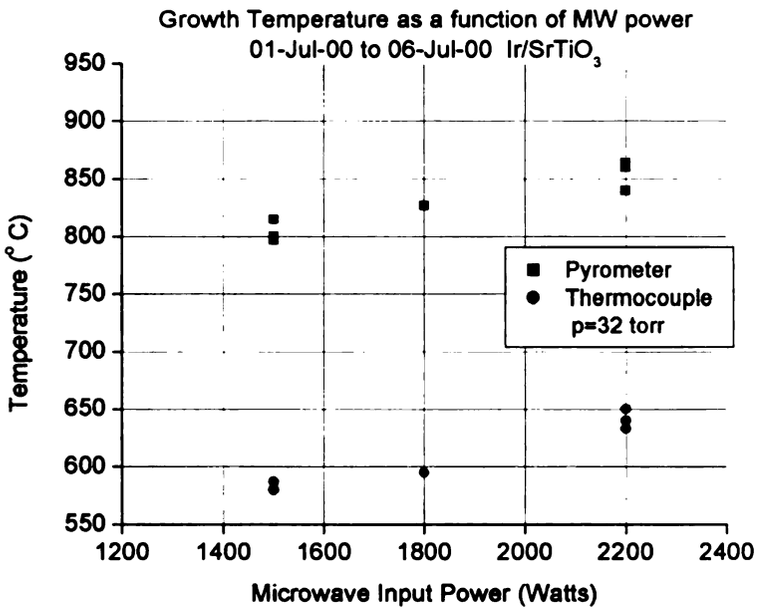

Figure 49 Growth temperature at 32 Torr as function of microwave input power. Temperature measured with an optical pyrometer focused on the Mo cap, and a K-type thermocouple fixed underneath the stainless steel platform.

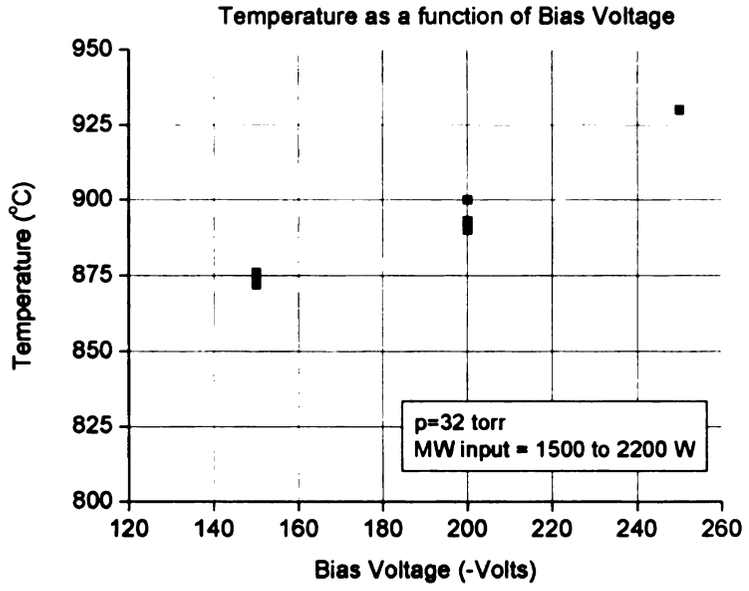

Figure 50 Temperature as a function of negative bias voltage at 32 Torr. Temperature is measured with an optical pyrometer focused on the Mo cap surface.

The results of these calibrations indicated a strong dependence of temperature on gas

pressure. In general, bias current decreased with increasing pressure at a fixed voltage. Microwave power, on the other hand, had little effect on bias current. Furthermore, subsequent studies showed changing the distance of the bias ring from the holder changed the shape of the plasma, as well as the current and thus temperature. Raising the bias ring from 16 to 32 mm elongated the plasma between the two electrodes, and the current decreased on average 20 mA.

We lowered the temperature over a series of runs by decreasing pressure from 32 to 18 Torr, decreasing the microwave power from 2.2 to 1.5 kW, lowering the bias voltage from –250 to –150V, and increasing the ring height from 16 to 32 mm. We also eliminated N_2 from the feed gas. Under these conditions, we found the temperature was 710 ± 10^{o} C during biasing as measured by an optical pyrometer focused on the Mo cap.

For a 30 min bias, the Ir appeared undamaged with locally high nucleation densities, 10^{10}-10^{12} cm^{-2}. We next sought to improve nucleation uniformity. Increasing the bias voltage only caused Ir damage, and fast growth due to high temperatures. We extended the bias time with the intent to saturate the surface with carbon. The near-optimal biasing parameters are shown in Table 10.

Microwave power	1.5 kW
CH_2/H_2 ratio	2%
Pressure	18 Torr
Bias Voltage	-150 V
Bias time	60 min
Ring height	32 mm

Table 10 Parameters for carbon saturation of the Ir surface during biasing.

SEM images showed a substrate covered in a bright electron-emissive dense carbon deposit (Figure 51).

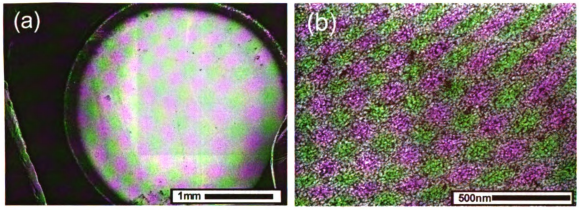

Figure 51 SEM images of sample (17-Jul-00) with conditions of Table 10. The circular bright area in (a) corresponds to the biased region of the 5 mm square Ir/oxide sample, exposed to the plasma through the round opening of the Mo sample cap. The surrounding dark area is bare Ir, masked by the sample cap. The narrow band around the bright area is due to shadowing by the sample cap. The objects in the lower right and left of the image are copper sample clips, part of the SEM sample holder. (b) shows a high resolution scan of the central region of the sample, covered in a uniform dense carbon deposit. The sample was in the plasma for 1 min beyond biasing, so some growth and coalescence of nuclei has already occurred.

Short growth after biasing under somewhat modified CVD conditions (Table 12, Section 9.1) showed that this carbon layer was necessary for the nucleation and growth of diamond single crystal films.

8.3.1 The molybdenum cap and sample holder

After many CVD runs, the Mo cap became thickly coated with diamond which began to flake off. The uncoated surface of a new cap and sample holder did not yield a uniform coverage of the sample, but rather inhomogeneous nucleation as shown in Figure 52.

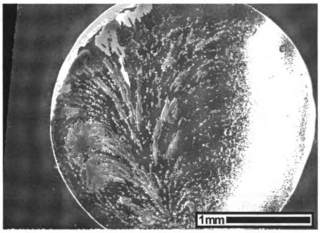

Figure 52 Sample 07-Nov-2000 after standard 60 min biasing and 3 hr growth. Mo cap was polished and uncoated. Bright region has a very high density of highly twinned crystals

8.3.2 Sample height relative to the plasma

We observed bias and growth temperature were sensitive to the vertical position of the sample. Figure 53 shows a plot of bias temperature vs. position of the top of the sample holder (relative to the fixed stainless steel platform). Only bias temperature is plotted here for clarity, the growth temperature was 40-50° C lower for each run.

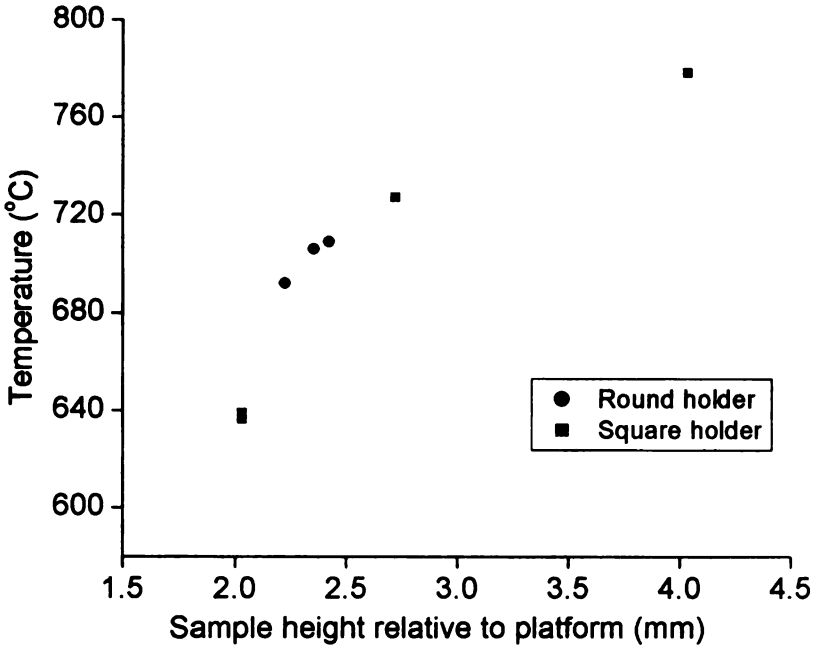

Figure 53 The temperature during bias vs. sample holder height; relative to the fixed stainless steel platform in the CVD reactor. A round and square sample holder was used. Pressure, 18 Torr, except for data at 4.0 mm, p=16 Torr. Temperature was measured using an optical pyrometer focused on the Mo cap surface.

The strong temperature dependence is surprising, and is essentially independent of sample holder shape. A temperature change of 50° C occurred for a 0.5 mm change in height. Since there is a narrow temperature window in which diamond "nucleation" can occur, the precise positioning of the sample with respect to the plasma is crucial. We found the optimal condtions for diamond nucleation and growth occurred at a 2.4 mm height relative to the platform, for which the sample temperature was 710° C for bias and 650° C for growth. The height maximized the nucleation density. Qualitatively, it appears that variations in height may also expose the growth surface to different plasma species at different concentrations.

8.3.3 The secondary plasma

During biasing we observed a bright, secondary, plasma that occurred directly above the sample, separated from the main plasma discharge (Figures 57 and 58). We made the following observations: (1) The presence of a secondary plasma during biasing is a necessary, but not sufficient, condition for efficient diamond nucleation on Ir; (2) Instability of the secondary plasma during biasing is fatal to good nucleation; (3) Bias voltage, bias current, geometry and the cap coating influence the secondary plasma glow.

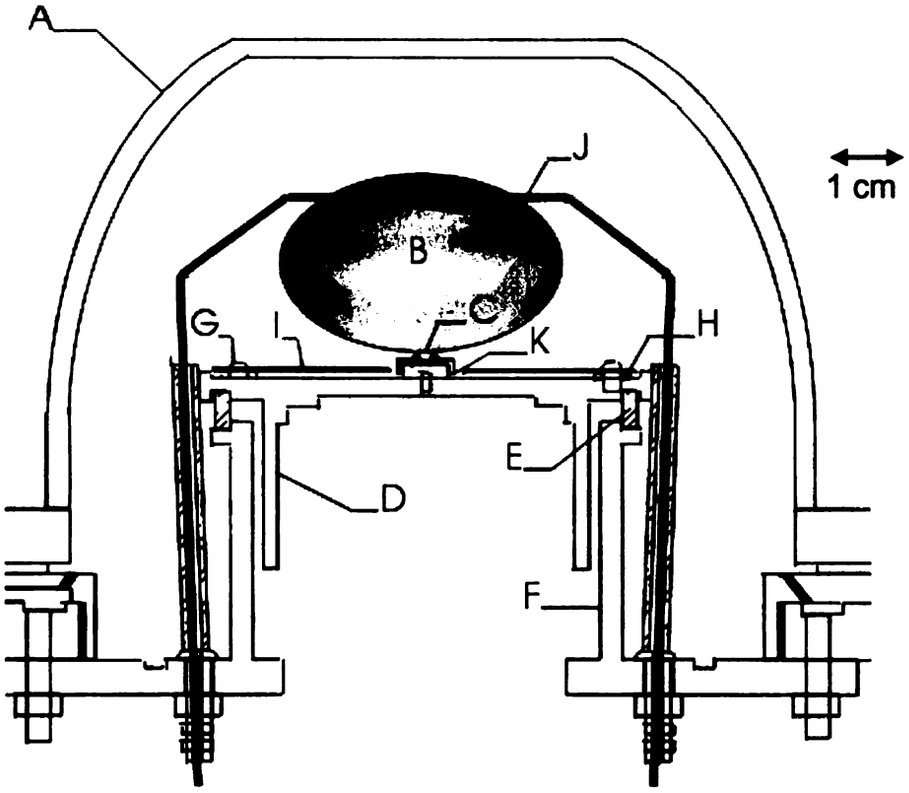

Figure 54 Cross-section of the bias stage and the sample holder. The bias ring confines the main plasma discharge. A secondary discharge appears above the sample area. A. Quartz dome. B. Main plasma discharge, C. Secondary plasma discharge. D. Stainless steel platform, E. Quartz isolation ring, F. Stainless steel stage, G. Alumina centering posts for the Si mask, H. Alumina washers for mask isolation, I. Si mask, J. Bias ring and supports, K. Mo sample holder.

The small secondary discharge appears pale, almost colorless, and is much brighter in intensity than the main discharge. There is also faint blue glow over the diamond coated

cap. Whereas the secondary plasma extinguishes immediately when the bias is turned off, the blue glow over the cap remains. Other groups have reported on a blue, purple or red secondary plasma above the sample, or the diamond covered sample holder *(85, 86, 121-123)*, but they have not noted that the secondary discharge was confined at the sample. We believe that the characteristics of the secondary plasma result from a dc glow discharge induced by the biasing process in the specific reactor geometry used. From the discussion of glow discharges in Section 3.4.1, the secondary discharge could correspond to the negative glow. Other groups *(76, 125)* have reported the secondary discharge corresponded to the cathode sheath. If the secondary plasma is a negative glow of a dc discharge, then electrons are carrying the current in this region. The pale, slightly blueish color of the secondary plasma is indicative of the negative glow region of a hydrogen glow discharge *(44)*. The cathode glow in a hydrogen plasma should have a reddish/brown color.

8.4 0^+ growth experiments – The effect of biasing on $Ir/SrTiO_3$ and Ir/Al_2O_3

8.4.1 Bias experimental procedure (0^+ growth)

The experiments described in the remainder of this chapter consist of a CVD biasing procedure with no subsequent growth. These investigations were concerned with the time development of the bias process. However, some short time growth is inevitable even if the plasma is extinguished after bias. This is the reason for adopting the terminology "0^+" growth. To reliably compare a series of runs, we made every effort to insure a reproducible process for every experiment. 0^+ growth experiments (or biasing only) were carried out with the following conditions: 1800 W microwave power, -150 V

DC bias, 2 sccm CH_4 in 300 sccm H_2 at 18 Torr. Timing began with ignition of the plasma at 1000 W and 10-12 Torr. There is some variability in the exact pressure when the plasma is ignited, because the pressure rises very quickly at this stage. The process included the following steps:

t=0 (1) Hydrogen cleaning: 300 sccm hydrogen is flowed into the bell jar to raise the pressure to 15 Torr.

t=5 min (2) "Carburization": the methane flow is turned on to 2 sccm. The pressure setpoint is increased to 18 Torr.

t= 15 min (3) The bias power supply is switched on. The voltage control on the power supply is switched on at t=16min.

t=17 min (4) The bias voltage is increased smoothly from 0 to –150V over 20 s.

t=20-180 min (5) The biasing period. At the end of the biasing period, the microwave power is turned off. This extinguishes the plasma and the biasing current drops abruptly to zero. The throttle and gas valves are closed immediately to stop the gas flow into the system; the bias power supply is switched off. The system is pumped out using the backing pump.

The important part of the process is the rapid termination of the biasing step, leading to a "quenching" of the sample temperature.

Examination of the Ir surface with SEM has proven useful in visualizing the carbon distribution, and the early stages of diamond growth. When examining the following images, it should be noted that there are two effective means of interpreting contrast in a SEM image. Higher topographical features are brighter because they present

a larger volume to the electron beam; so more scattered electrons are produced. Diamond, in contrast to other forms of carbon, produces a bright SEM image because of its high electron emissivity. This is critical, as extremely small volumes of diamond can be detected.

The following sections describe how carbon condenses on Ir/$SrTiO_3$ samples as the biasing period varies from 20 to 180 min.

8.4.2 20 min bias

Although the Ir surface appeared unchanged under visual inspection after 20 min bias, SEM revealed striking changes to the surface (Figure 55).

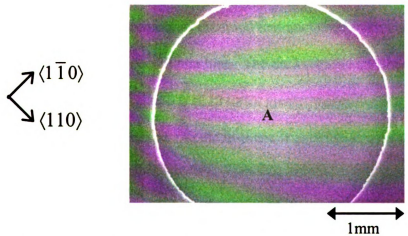

Figure 55 SEM image of sample 20-Jul-02 of (001) Ir on $SrTiO_3$ after 20 minute bias.

The above SEM scan shows bright contrast in the circular region at the center of the 5 mm substrate. The exposed area is circular, a result of the 3.5 mm aperture of the Mo cap. The edge of the exposed area is brighter due to a buildup of carbon at the inside edges of the cap. The area labeled A in Figure 55, is expanded in Figure 56 revealing bright contrast that originates from an inhomogeneous diamond, or diamond-like, deposit

that covers 75 ± 4% of the surface.

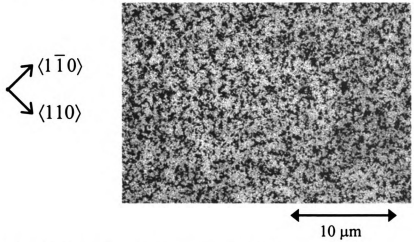

Figure 56 Center region of 20 min sample (20-Jul-02)

The percentage of carbon coverage is calculated by binarizing the image, and measuring the ratio of white to black areas. Variation in the threshold limits determines the error. We interpret the bright condensate as diamond that nucleated from the carbon deposited on the Ir over the course of the 20 min bias. The dark regions are believed to be Ir, not yet covered by diamond. Figure 57, at 10 times greater magnification, shows that the condensate is oriented with respect to the in-plane Ir crystallographic axes.

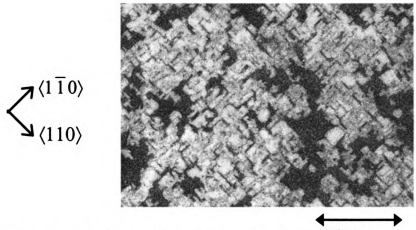

Figure 57 20 min bias sample (20-Jul-02) SEM image.

Block-like areas, 100-200 nm, are oriented along Ir [110] directions. The dark regions

are either bare Ir, or areas covered with non-diamond carbon where diamond has not yet nucleated. A higher magnification image, Figure 58, shows the structures in the dark regions. These lines of diamond appear to decorate surface features that are aligned with Ir [110] directions.

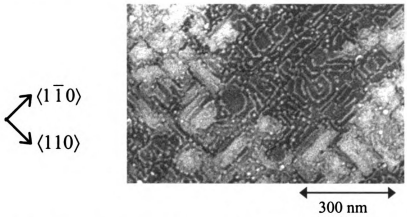

Figure 58 High resolution SEM image of 20 min bias sample (20-Jul-02).

The "whorls" may correspond to diamond that preferentially nucleates on topographic features of the Ir, e.g., step edges. The thickness of the deposits has not been measured directly with AFM, but are expected to be only a few nm.

8.4.3 60 min to 80 min bias

Runs of 60 and 80 min bias led to similar results for coverage: 82 ± 4% for 60 min, 89 ± 4% for 80 min. An SEM image of the central region of a 60 min bias sample (the same scale as Figure 57) shows an increased area of diamond deposition (Figure 59).

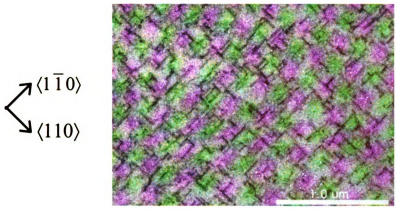

Figure 59 Central region of 60 min bias sample (18-Jul-02).

Here, dark regions correspond to areas devoid of diamond that lie along [110] directions. The 80 min bias sample was nearly indistinguishable from these results at this magnification.

At higher magnification, Figure 60, remarkable features emerge. An SEM scan of the bright area on an 80 min bias sample is shown in Figure 60.

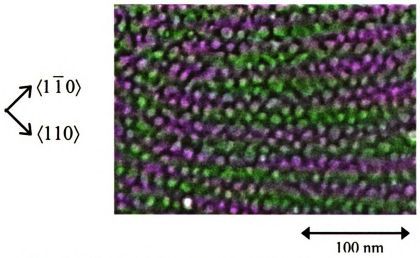

Figure 60 SEM image of 80 min bias sample (22-Jul-02).

The image shows small bright objects on a dark background with a mean diameter of 10-15 nm distributed across the Ir surface. In some cases, as in Figure 60, the particle edges appear aligned with Ir [110] directions. A quantitative analysis of the distribution of

particles is given in Section 8.5. If the outermost edge of this sample is examined, Figure 61, it shows a pattern similar to that seen at the shortest bias times (20 min).

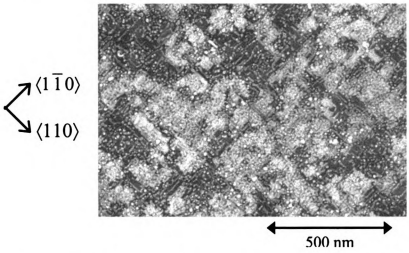

Figure 61 Edge (within 200 μm of the inside cap edge) of 60 min bias sample (21-Jul-02).

The above SEM scan was taken only about 200 μm from the inside cap edge. With the exception of this small, circumferential region, the density was uniformly high over the rest of the substrate.

8.4.4 120 and 180 min bias

Biasing for yet longer times (120 and 180 minutes) proved detrimental to the Ir surfaces. An SEM image of a 120 min bias sample shows new features that did not appear at shorter times (Figure 62).

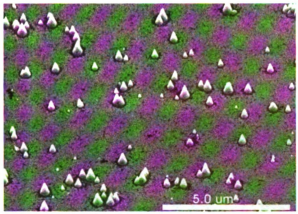

Figure 62 120 min bias sample (08-Sep-00). 30° sample tilt

Small white asperities on a scale of 200-300 nm appeared on the surface. The white spots appeared as "cone-like" growths in the carbon deposit. This indicated that extended biasing caused instabilities to develop in the carbon deposit and the occurrence of growth during biasing. The instabilities may initiate at defects in the iridium surface. The above scan was taken at a 30° tilt of the substrate in the SEM.

180 min of biasing resulted in significant damage to the iridium surface (Figure 63).

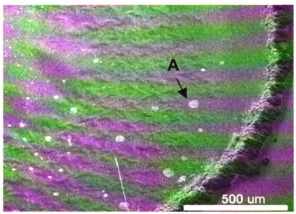

Figure 63 Corner of 180 min bias sample (08-Sep-00). 30° sample tilt.

The Ir buckled and detached from the substrate surface. This SEM image is of the lower

right corner of the biased sample area. A ridge of carbon formed along a circular ring defined by the inner edge of the Mo cap. An image of a spot, such as at the region labeled A, is shown in Figure 64 at higher magnification.

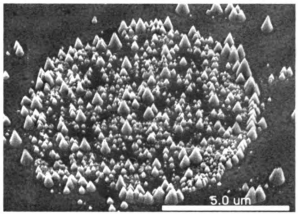

Figure 64 SEM scan of 180 min bias sample (08-Sep-00). 30° sample tilt.

The spots show a "forest" of the cone-like growths that self-assemble into μm-diameter clusters that appeared also on the 120 min bias sample. It may be that the cones stimulate growth of more neighboring cones. The range in cone sizes suggests that they did not appear simultaneously, but emerge over time.

8.5 Quantitative analysis of 60 min bias on Ir/Al_2O_3

Our standard process for single crystal diamond involves a 60 min bias, therefore this bias time is of particular interest. The sensitivity of the SEM to diamond enabled us to distinguish individual crystallites that emerge at a very early growth stage of diamond on Ir. (See Figure 60 and Figure 65). The clarity of the images has allowed us to characterize the size and spatial distributions using several statistical measures: (1) direct real-space particle analysis to obtain the areal density and size distribution; (2) 2-dimensional Fourier transforms of binarized images to reveal spatial symmetry, and (3)

radial density functions that show interparticle correlations. The particles are of order 10 nm in size. The particle density (n) was calculated by binarizing the image, so that the particles became black blobs on a white background. They were then labeled and counted over the entire SEM image area using the NIH ImageJ software package *(153)* This was done for SEM images on different samples of the same bias time. The particle density is calculated directly by dividing the number of particles by the image area. For 60 min samples, $n = 3.2 \pm 0.7 \times 10^{11}$ cm^{-2}. The nucleation and early growth was similar on Ir/$SrTiO_3$ and Ir/Al_2O_3 samples. The analysis contained in the rest of this chapter was done on 60 min biased Ir/Al_2O_3 samples.

The particle distribution at first appears random for a 60 min biased sample, as can be seen in Figure 65.

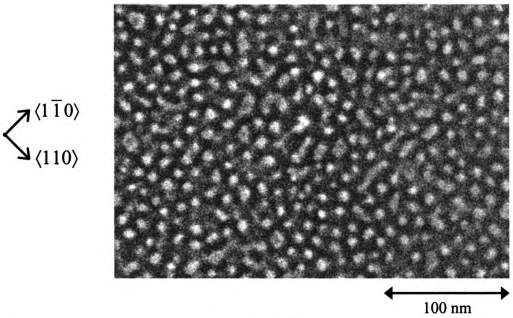

Figure 65 High resolution SEM image of 60 min bias sample 12-Apr-02.

Closer inspection, however, showed evidence for spatial correlations. In order to test for this possibility, we calculated 2-D Fourier transforms as follows:

A grayscale SEM image was first cropped to 512x512 pixels, and then filtered to equalize the level of contrast, since the SEM scans often had a grayscale gradient across the digitized image. The filtered image was then transformed to a 1-bit black/white image. The threshold level was set by inspection. Since this setting is somewhat subjective, it was varied to determine the effect of different levels and chosen to maintain a reasonable representation of the original image. An example of the filtered SEM image, and its binarized version are shown in Figure 66 for a 60 min bias sample.

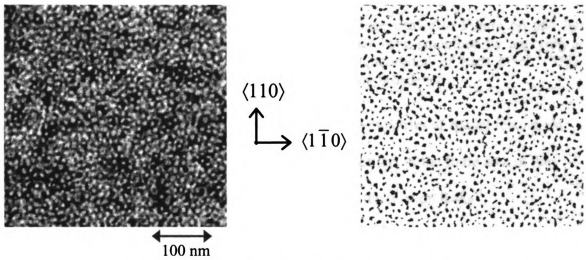

Figure 66 Equalized SEM scan (left) of sample 12-Apr-02 and its binarization (right). Nuclei correspond to light spots in the SEM image, dark spots in the binarized image.

Although the sizes of the particles are somewhat dependent on the binarization threshold, there is little effect on the number of particles in a 100 nm^2 area, or on their relative positions. The 2-D FFT of the binarized image was calculated using the Image/J software program. The power spectrum of the 2-D image from the SEM image of Figure 66 is shown in Figure 67, with intensity on a logarithmic scale.

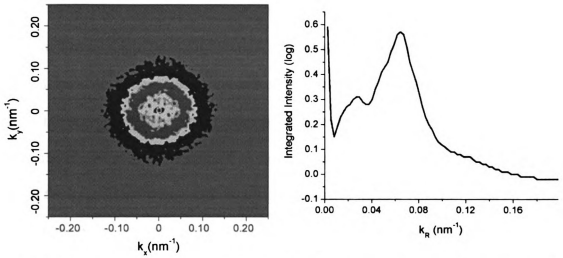

Figure 67 2-D power spectrum of the binarized image shown in Figure 66 and its radial cross-section. The power spectrum has been smoothed by applying a filter that takes the average of the 3x3 neighborhood of each pixel. This process was applied twice, so small features are broadened.

The Fourier transform is useful for revealing averaged symmetries of spatial features in an image. Figure 67 shows an intense central peak, an artifact of the finite area of the transform, and a prominent ring at k_R= 0.068 nm^{-1}, with the relation $R=k_R^{-1}$, corresponding to a real-space distance of R=14.7 nm. A smaller peak at k_R=0.028 nm^{-1} emerged from the cross-section at R=35.7 nm.

The radial distribution function can give information about the distribution of nearest and next nearest neighbors. It is often used to describe the spatial correlations between molecules in a liquid *(154, 155)*, particularly in analyzing X-ray scattering data of liquids *(156)*. It is here modified for 2D. A density, $\rho(r)$, is defined for the number of particles (n) per unit area of an annulus of width, dr, as $\rho(r)dr = \frac{dn}{2\pi r}$. The radial distribution function, $g(r)$ is then defined as the density function at a radius r divided by the total areal density, i.e. $g(r) = \frac{\rho(r)}{\rho_o}$, where ρ_o is $N/(\pi R^2)$. For large r, $g(r) \rightarrow 1$.

The radial distribution of small crystallites was found by assigning a (x,y) position to every particle in the binarized image of the sample pictured in Figure 66. For this analysis, the entire SEM image was used (1280x960 pixels) in order to keep the largest data set possible. A cutoff value of 10 px was assigned, so blobs smaller than 10 px in the above image were ignored in the analysis. The (x,y) positions were found using the Image/J software measurement tool, which picked a center of mass for each blob in the image, and assigned it a coordinate relative to the upper left corner of the image. The output was saved as a text file. The distances between all pairs of coordinates were calculated using a script, which binned the measurements, and saved the results to a text file. The normalized RDF for the image of Figure 66 is shown in Figure 68.

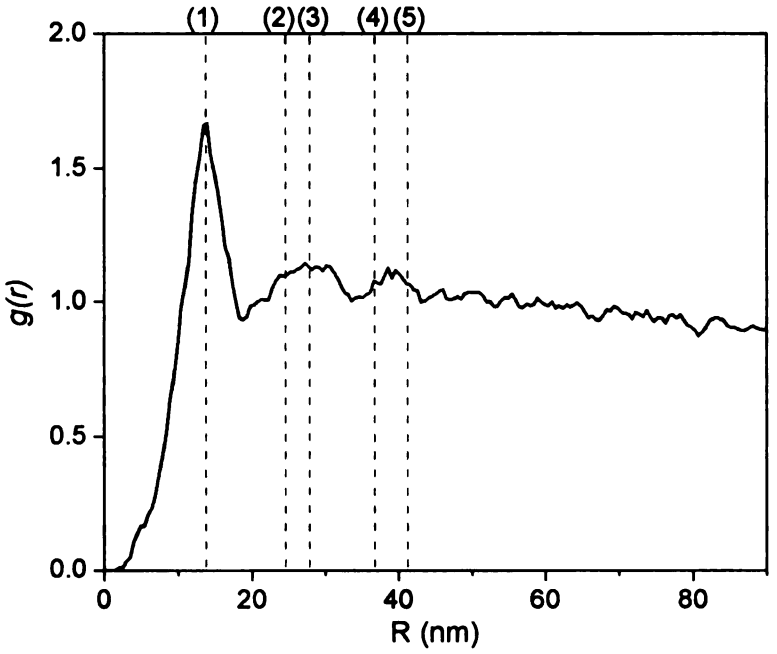

Figure 68 Radial distribution function plot of 60 min bias sample. Dropped lines show predicted peak positions for a 2D hexagonal array. A properly normalized RDF should asymptotically approach 1 as $R \rightarrow \infty$. The fall off at large R is due to finite system size (R_{max} ≈240 nm).

The RDF shows a first nearest neighbor peak at 13.8 nm followed by two broader peaks. The position of the first peak agrees well with the measurement from the 2-D Fourier transform and indicates strong correlations in radial distances of adjacent crystallites. The presence of higher order peaks indicates that correlations persist to much longer distances. The peak positions for a hexagonal array are tabulated in Table 11 for a first nearest neighbor distance, a = 13.8 nm.

Neighbor	*Distance*	*Calculated for a=13.8 nm*
1st	a	13.8
2nd	$\sqrt{3}a$	23.9
3rd	$2a$	27.6
4th	$\sqrt{7}a$	36.5
5th	$3a$	41.4

Table 11 Calculated values for a 2D hexagonal array.

The predicted and measured values up to 4th neighbor distances agree well. The second peak in the RDF maybe be significantly broadened because it involves overlap of the 2nd and the 3rd neighbor peaks. The third peak in the RDF falls in between the calculated values of the 4th and 5th neighbors.

8.6 Discussion

The time evolution experiments of biasing on Ir indicate there is a window for the bias time. A bias period that is too short results in incomplete sample coverage, and a bias period that is too long causes damage to the Ir. However, close examination of the short bias time (20 min) was useful for identifying the island aggregation of the carbon on the iridium. Aggregation of depositing material on a substrate is known for other systems of epitaxial deposition, and has been studied using STM (Scanning Tunneling

Microscopy) and computer simulations *(157-160)*. It is possible that certain areas of the Ir, such as step edges, have different sticking coefficients for carbon, and are preferential for the carbon. This has been shown to be the case in Si/(001)Si epitaxy, *(161)*, for the transition between 2-D layer by layer and island growth.

Inspection of SEM images of 60 min bias samples, such as in Figure 65 and Figure 66, suggested to us a hexagonal close-packed array of particles. Most crystallites appear to have an average of six nearest neighbors. The RDF peak positions agree well with a hexagonal array, and indicated the correlation goes further then can be seen by inspection. This suggests that the distribution results from "interactions" among nuclei. We infer that nucleation does not need to occur at special topographic features of the substrate. Careful examination by SEM also reveals that the crystallite shapes, even at this early stage, are faceted with [110] lateral faces. Furthermore, the narrow distribution of sizes of crystallites across the entire surface of the Ir strongly suggests that nucleation begins synchronously with the termination of bias current. The areal density measured, $n = 3.2 \pm 0.7 \times 10^{11}$ cm^{-2}, is a lower limit on the nucleation density. As some coalescence has already occurred, it is likely closer to 10^{12} cm^{-2}. Our measurements for nucleation densities are unambiguous, based on a count of particles per unit area. This is significant because nucleation densities in other reports have usually been estimated from outgrown crystals. In Chapter 4, Table 6 and the accompanying discussion, we pointed out that the highest nucleation densities previously reported on Ir are 10^8-10^9 cm^{-2} *(4-8)*. Other work that has examined the initial distribution of crystallites, looked at the distribution of nearest neighbor distances for diamond crystallites on silicon *(88, 111)*. It was found that the measured nearest neighbor distances follow a random nucleation model, with no

spatial correlation. We believe the correlated distribution of crystallites is directly related to the high nucleation densities observed on the Ir after biasing. This arrangement of nuclei could not happen unless the nucleation occurred as the sample was quenched with the cessation of the bias. This leads to the formation of single crystal diamond after short growth times.

8.6.1 Nucleation and early growth model of heteroepitaxial diamond

Based on the evidence presented in this chapter, we propose the following model for the nucleation and growth of heteroepitaxial diamond (Figure 69).

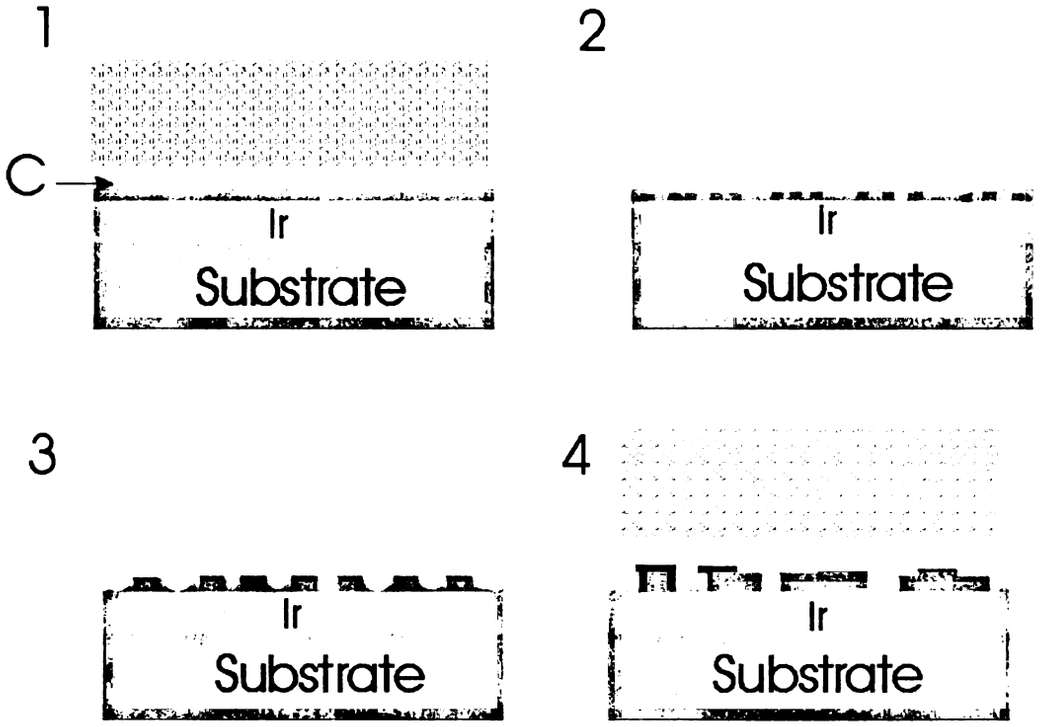

Figure 69 Model for heteroepitaxial nucleation and growth of diamond on Ir. 1) Ion bombardment and/or enhanced electron emission in the sample vicinity leads to deposition of a carbon layer on the iridium. 2) Cessation of the bias current leads to immediate nuclei formation on the surface. 3) Early growth involves depletion of local carbon, and coalescence of nearby nuclei into crystallites. 4) Growth from vapor phase proceeds on a surface already almost entirely covered by diamond.

1. Biasing deposits carbon on the surface of the Ir. In the presence of a bias current, the carbon condensate is in a highly excited, nonequilibrium state, and nucleation does not take place. It is also possible that long bias times (60-80 minutes) are necessary for the carbon to diffuse into the iridium and saturate the surface.
2. Turning off the bias voltage causes the temperature to drop rapidly with the extinguishing of the secondary plasma over the sample. The carbon condensate cools, and nucleation is initiated.
3. Early growth is dominated by depletion of the carbon deposited during biasing by the initial nuclei. It is possible that there are much higher densities of nucleation sites initially ($>10^{12}$), but competition for surface carbon amplifies growth of larger nuclei.
4. Growth proceeds from the vapor phase as the surface carbon is depleted. Coalescence occurs via lateral overgrowth methods while the crystallites are still very small, because they are so densely packed.

8.7 Summary

In summary, experiments initially on Si and later on Ir/oxide substrates allowed us to increase the current density to the sample leading to increased nucleation densities. Bias geometry and conditions which are conducive to the appearance of a secondary plasma over the sample during biasing are crucial to the success of the diamond nucleation. We developed a precise processing procedure that leads to rapid quenching of our samples after bias. This allowed us to examine previously unseen early stages of diamond growth on Ir. The initial arrangement and density of crystallites on the iridium were investigated quantitatively. The Fourier transform clearly shows a circularly

symmetric ring corresponding to R=14.7 nm in real space, a nearest-neighbor correlation length. Radial correlations persist to large distances. The RDF plot confirmed this, and distances of nearest neighbors are consistent with a hexagonal close packed 2D array for to 3rd and 4th neighbors. We ended by presenting a new model for the nucleation and early growth of diamond on Ir.

Chapter 9 Heteroepitaxial diamond growth: characterization and analysis

This chapter examines the growth of diamond on iridium on strontium titanate and sapphire substrates. The first section discusses experiments with growth times of ≤ 3 hr on Ir/$SrTiO_3$, and on Ir/Al_2O_3. The other section describes thick diamond films grown on Ir/$SrTiO_3$ substrates.

9.1 Short growth experiments - ≤3hr growth time

Short growth experiments in this section are defined as experiments where we biased for one hour, under conditions conducive to high nucleation density, then changed CVD parameters to growth conditions that lasted as long as 3 hr. Bias and growth conditions are given in Table 12.

	Bias Conditions	*Growth Conditions*
Bias Voltage	-150 V	--
CH_4/H_2 ratio	2%	1%
Pressure	18 Torr	18 Torr
MW power	1500 W	1500 W
Time	60 min	1 min to 3hr

Table 12 Bias and growth parameters for short growth experiments

9.2 Progression of diamond growth – Ir/$SrTiO_3$

9.2.1 Early stages of growth – analysis using 2D-FFT

We studied the early growth and coalescence of diamond on Ir/$SrTiO_3$ with interrupted growth experiments at intervals of 1, 5, 10, and 20 minutes. An SEM image of the surface after approximately 1 min growth is shown in Figure 70.

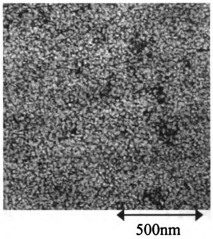

Figure 70 SEM micrograph of the sample surface after 60 min of biasing plus 1 min of growth (17-Jul-00).

The surface is covered in small oriented diamond particles that are already starting to coalesce. SEM micrographs were taken under the same conditions at identical resolution for 5, 10 and 20 min growth. 2D-FFTs were performed on the SEM micrographs to obtain an objective understanding of the early grain growth and coalescence. Even for short growth times, coalescence has proceeded enough to make individual grains indistinguishable. Therefore, in contrast to the Fourier analysis of the previous chapter, the transforms here reflect the voids between incompletely coalesced adjacent crystallites rather than individual particles. In the binarization procedure the voids appear as dark regions and the diamond as white. The real space SEM micrographs are shown at the left

and the corresponding reciprocal space power spectra on the right in Figure 71.

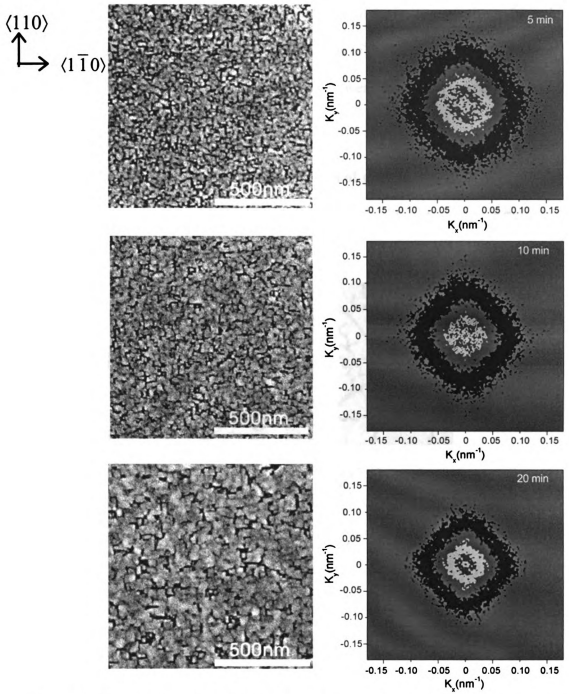

Figure 71 SEM micrographs of 5-20 minutes diamond growth and the corresponding 2-D power spectra.

The 2-D power spectra reveal the anisotropic orientations of the voids appearing in the SEM images. As coalescence proceeds, the average distance between voids increases;

thus the power spectrum contracts in reciprocal space. Alignment of the voids emerges as an increased sharpening of the four-fold symmetry in the power spectrum. In each case, the voids are aligned with the <011> directions of the Ir. The Fourier transform demonstrated that after 20 minutes of growth, voids were almost exclusively aligned along these directions.

9.2.2 Complete coalescence – 30 to 180 minutes of growth

SEM and AFM studies demonstrated the evolution of coalescence of films grown for 30 min, 60 min and 180 min (Figure 72).

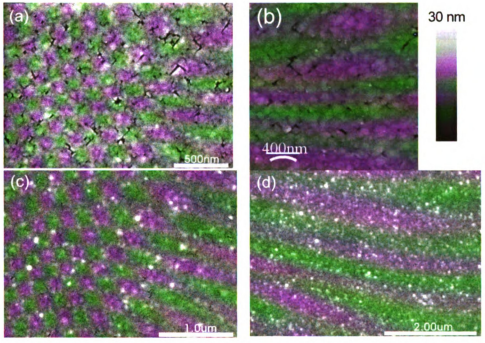

Figure 72 Diamond on Ir/$SrTiO_3$. (a) 30 min growth SEM image sample 21-Jul-00 , (b) 30 min growth AFM scan of 21-Jul-00 , (c) 60 min 09-Apr-01, (d) 180 min, 23-Jun-01.

A high magnification image of the central region of the 30 min sample, (a), showed few residual voids. An AFM scan, (b), of the central region had a mean roughness of 2 nm. The remnant voids are the darker regions. 60 to 180 min of growth after biasing under

the conditions of Table 12 resulted in completely coalesced continuous films with the occasional void over a few μm^2 area, (c) and (d). The thickness of a 180 min film (19-Jun-01) was 0.54 ± 0.02 μm obtained from SEM images of a fracture surface. Optical microscopy showed a uniform, transparent film, with features of the substrate visible through the diamond film. The bright spots in the SEM images of Figure 72 are small asperities on the surface; thus, they are related to surface roughness. The AFM scan (b) in Figure 72 with its vertical scale, indicates that these features are a few nm high. Charge builds up on these areas as the electron beam scans across the surface and electron emission is enhanced. Their presence is most noticeable on films of small thickness with few voids. Voids, which may contain graphitic or other carbon, may shunt the SEM current to the conducting Ir substrate, reducing the enhanced emission from the "tip". This reduces the charge buildup in this region.

9.2.3 Comparison with other results by other groups

Our 60 min films, which exhibit complete coalescence and coverage, may be contrasted with a 600 nm film on Ir:$SrTiO_3$ reported by Schreck et al. shown in Figure 73 and Figure 74 *(8)*.

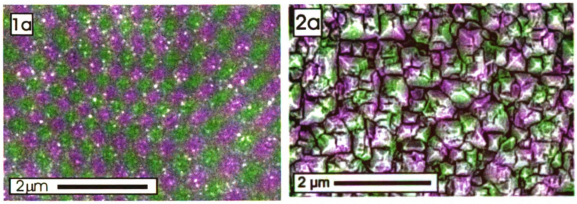

Figure 73 (1a) SEM micrograph of the center of a 173 nm ± 2 nm thick diamond film on (001) $Ir/SrTiO_3$ grown in this study. Thickness was measured by SEM from cross-sections (2a) SEM micrograph of a 600 nm thick diamond film on (001)$Ir/SrTiO_3$, Schreck et al. *(8)*.

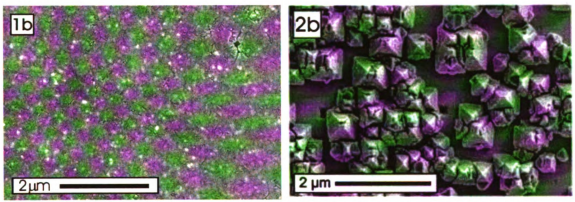

Figure 74 (1b) SEM micrograph of the edge of the diamond film shown in Figure 73 (1a), 1.5 mm from the center. (2b) Edge of the epitaxial area of the film shown in Figure 73 (2a) grown by Schreck et al. *(8)*.

Aside from an occasional void, our films show complete coalescence at the center, whereas thicker films of other groups still show evidence of individual crystallites. At the edge, we have a few voids, but the scale of features is much smaller than comparable studies. We believe that the early coalescence of our films is a direct result of the high nucleation densities reported in the previous chapter. We observed such film growth on both $Ir/SrTiO_3$ and Ir/Al_2O_3 substrates. Subota et al. *(6)* also reported on a thin diamond

film grown for 2.5 hr total after 60 min biasing. They did not give the film thickness, and SEM images show some holes and residual voids. Thinner films (1hr bias and 30 min growth) show morphology similar to those of Schreck et al. in Figure 73. Ohtsuka et al. report an average roughness of 1 nm for most of the epitaxial area from AFM for a 1.5 μm thick film *(4)*, as compared to 2 nm we measured for a 30 min film. For growth of 30 minutes after biasing, they have a nucleation density of ~10^8 cm^{-2}, and isolated epitaxial particles are observed *(5)*.

9.2.4 X-ray diffraction studies on 180 minute diamond films

The crystallographic relationship of the diamond, Ir and $SrTiO_3$ was determined to be $(100)_{dia}<110>_{dia}||(100)_{Ir}<110>_{Ir}||(100)_{SrTiO_3}<110>_{SrTiO_3}$ by a {111}-ϕ scan of a 180 min diamond sample (Figure 75). The crystal was rotated by an angle ϕ about the normal to the (001), and reflections appear at angles corresponding to the expected {111} pole positions.

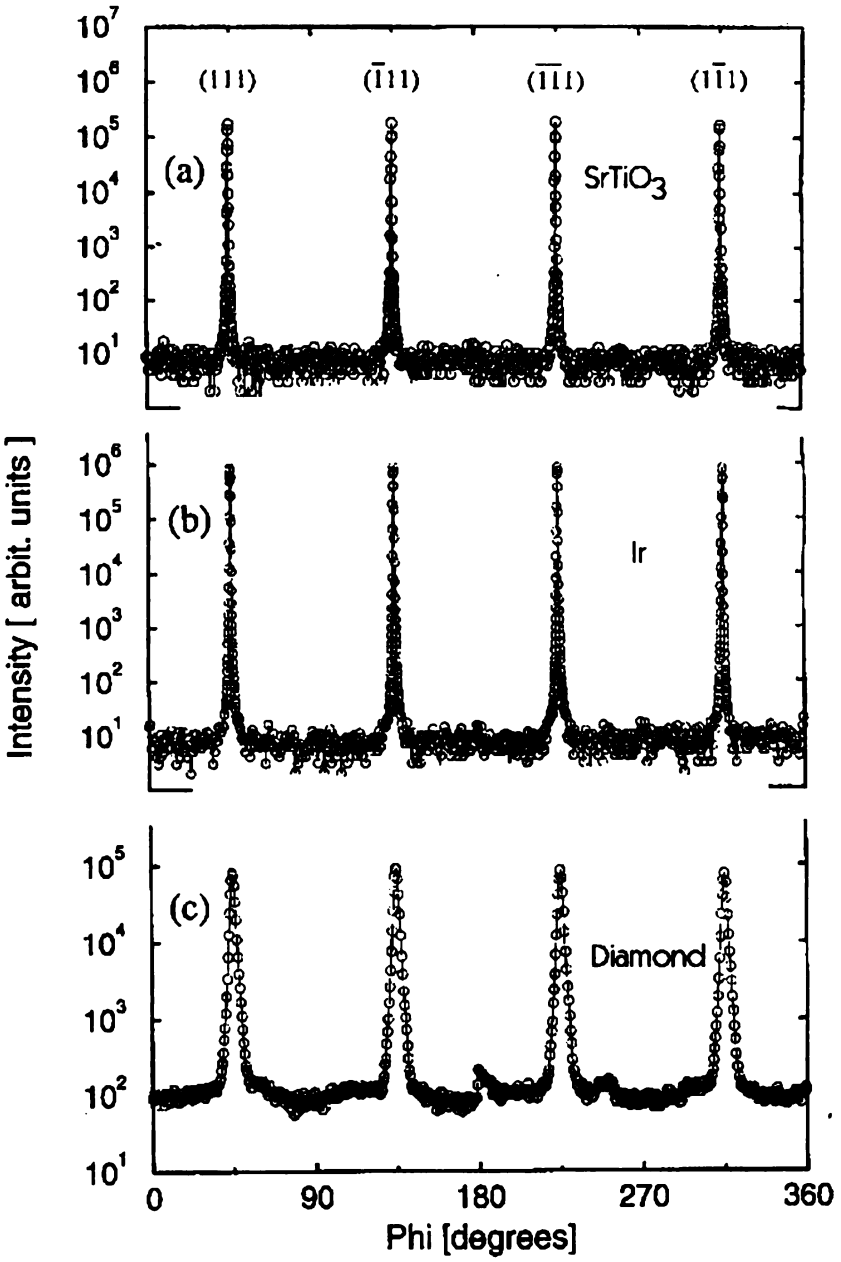

Figure 75 {111}–ϕ X-ray scans of 180 min diamond on Ir/$SrTiO_3$. Data taken by A.R. Kortan.

The four {111} reflections of the diamond, Ir and $SrTiO_3$ fall at the same angles, indicating in-plane as well as rotational alignment of all three crystals. The equal intensity of the peaks along ϕ requires perfect alignment of the sample in the x-ray beam. An x-ray reciprocal-space map is shown in Figure 76 for a (0KL) area scan taken using a

position sensitive detector.

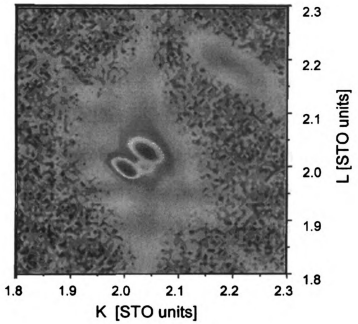

Figure 76 (0KL) X-ray area scan of a 180 min diamond film on Ir/$SrTiO_3$. The central dark spot is $SrTiO_3$ at (0,2,2), and all others are relative. The dark spot at (0,2.05,2.05) is Ir. Diamond is at (0,2.2,2.2). An unknown phase lies between $SrTiO_3$ and Ir, aligned with $SrTiO_3$ in the **K**-direction, and Ir in the **L**-direction. Data taken by A.R. Kortan.

The intensity contours in reciprocal-space are given relative to $SrTiO_3$, at (0,2,2). The Ir reflection is at (0,2.05,2.05) and diamond (0,2.2,2.2), in the upper right-hand side of the map. The small spot with the **K** of $SrTiO_3$ and the **L** of Ir indicates a stressed phase between the two that likely forms due to the lattice mismatch. Both the Ir and the diamond are strained with respect to the $SrTiO_3$ substrate. The asymmetry of the scan with the spots stretched along a line of constant **K**=2.03, and along **L**=constant***K**, indicates strain in these directions.

9.2.5 Effect of small angle substrate offcut – Ir/$SrTiO_3$

Diamond was grown on $SrTiO_3$ substrates, offcut with respect to the (100) direction by 7, 5, 1, and 0.1 deg. Growth is influenced by surface topography; as offcut angles increase, the step density increases. AFM scans showed mean roughness of 2-3 nm after 150 nm Ir deposition for all samples. Diamond grown on these substrates, however, exhibited different morphology and roughness, which depended on the $SrTiO_3$ offcut angle. All samples were grown in successive runs under identical CVD reactor conditions with a 1 hr bias and 1 hr growth. SEM micrographs are shown in Figure 77 and AFM scans in Figure 78.

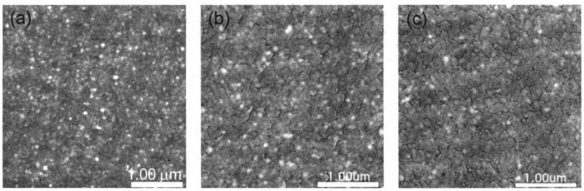

Figure 77 Scanning electron micrographs of diamond on Ir on offcut $SrTiO_3$ substrates. Offcut angle of $SrTiO_3$ (in deg): (a) 0.1, (b) 5, (c) 7. CVD run: (a) 25-Mar-02, (b) 23-Mar-02, (c) 22-Mar-02.

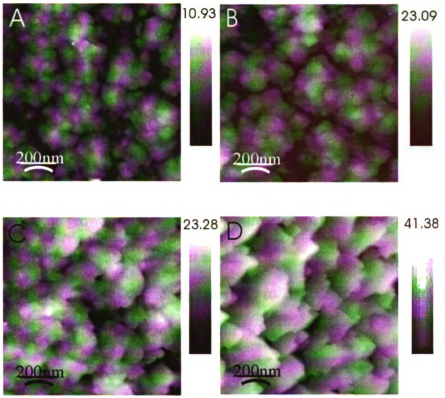

Figure 78 AFM scans of diamond on Ir on offcut (001) $SrTiO_3$ substrates. All scans are 1x1 μm^2. $SrTiO_3$ offcut angle (in deg): A. 0.1, B. 1, C. 5, D. 7. CVD run: A. 25-Mar-02, B. 24-Mar-02, C. 23-Mar-02, D. 22-Mar-02.

Figure 79 shows the mean roughness of the diamond as a function of the offcut angle of $SrTiO_3$.

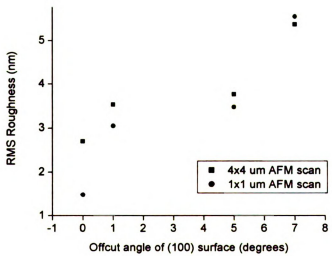

Figure 79 RMS roughness of diamond on Ir on offcut (001) $SrTiO_3$ substrates.

Roughness increased as the offcut angle increased. 0.1 deg offcut substrates gave diamond surfaces with the smoothest surfaces.

9.3 Evolution of diamond growth – Ir/Al_2O_3

We studied the very early stages of diamond growth on Ir/Al_2O_3, as well as growth times of 5 min to 180 min. As discussed in Chapter 6, both (001)- and (111)-oriented Ir films can grow on a-plane Al_2O_3 substrates, depending on deposition temperature and possibly substrate offcut angle.

For (100) Ir on Al_2O_3, diamond grown on 5 to 180 min samples looked similar to diamond with those same growth times on Ir/$SrTiO_3$ (Figure 80).

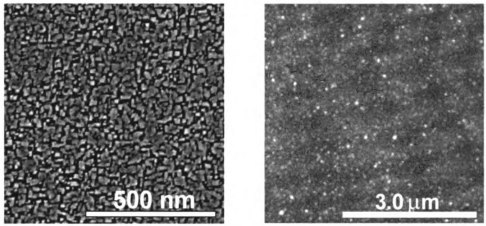

Figure 80 SEM micrographs of diamond on Ir/Al_2O_3 grown for 5 min (left) and 180 min (right).

X-ray diffraction rocking curve linewidths of diamond grown for 60 min on Ir/Al_2O_3 were also indistinguishable from diamond grown on Ir/$SrTiO_3$. We studied the initial growth of diamond on Ir/Al_2O_3 by rapid quenching after 20 and 90 seconds of growth as described in Section 8.4.1. SEM micrographs of our observations and the accompanying 2-D power spectra are shown in Figure 81.

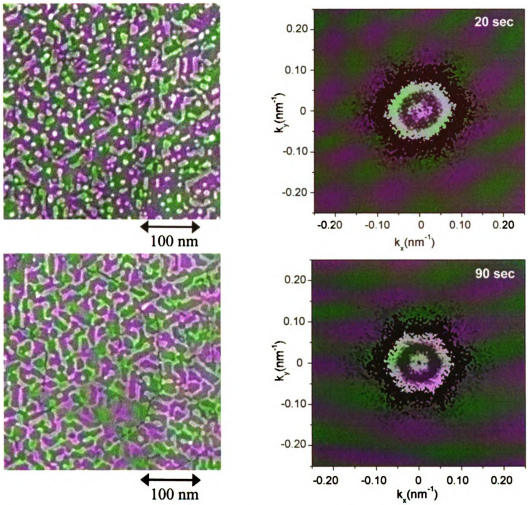

Figure 81 SEM scans of short growth on (111) Ir/Al_2O_3 and the corresponding 2-D power spectra.

The SEM micrographs and power spectra revealed a 6-fold symmetry we had not seen on any previous samples. Post-CVD X-ray diffraction on these surfaces revealed a (111) Ir surface, indicating that (111) Ir nucleated on $(11\bar{2}0)\,Al_2O_3$. This confirmed the symmetry seen in the Fourier transforms, and verified the transforms could be a valuable tool in visualizing angular alignment of crystallites after very short growth periods. The bright features in SEM micrographs may be evidence for (111) diamond deposition on (111) Ir. If the diamond were further grown under conditions conducive to (111) growth, the films could grow and coalesce similar to those on (001) Ir. We have not investigated further

the growth of (111) diamond in this work, but it is worth noting that these results strongly suggest it is possible to grow (111) single crystal diamond on Ir.

9.4 Thick films – Ir/SrTiO$_3$

Diamond films were grown on Ir/$SrTiO_3$ for periods of 6, 12, 36 and 48 hours. For thicker films the growth consists of a 2-stage process as outlined in Table 13.

	Bias Conditions	*Growth I*	*Growth II*
Bias Voltage	-150 V	--	--
CH_4/H_2 ratio	2%	1%	0.5-.75%
Pressure	18 Torr	18 Torr	28 Torr
MW power	1500 W	1500 W	1500 W
Time	60 min	90 min	4.5 - 46.5 hr

Table 13 Bias and 2-step growth CVD conditions for thick diamond samples.

After biasing, the samples were grown for 90 min after changing the CH_4 flow rate from 6 sccm to 3 sccm (2% to 1% CH_4:H_2). Then, CH_4 flow was reduced to 2.25 sccm (0.75%) and the pressure raised from 18 to 28 Torr by increasing the pressure setpoint by 1 Torr every 3 min.

Subsequent growth occurred under these conditions. SEM and AFM scans of the resulting films are shown in Figure 82 to Figure 84. The diamond films grown for 6 hours are extremely smooth (Figure 82).

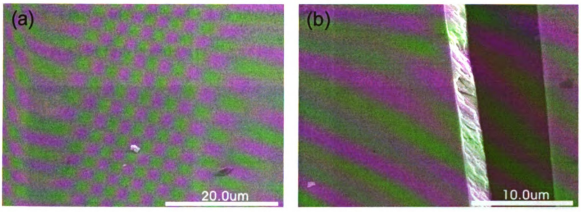

Figure 82 (a) Typical surface of a diamond film grown for 6 hr on Ir/$SrTiO_3$. The white speck is a piece of dust. (b) Fractured piece near the edge of the film that shows a cleaved surface.

6 hr films crack and break into pieces upon cooling in the CVD system due to stress from the mismatch of thermal expansion coefficients. The above images were made from remaining pieces of the film.

The 12 hr film cracked in half upon cooling, but otherwise remained intact (Figure 83).

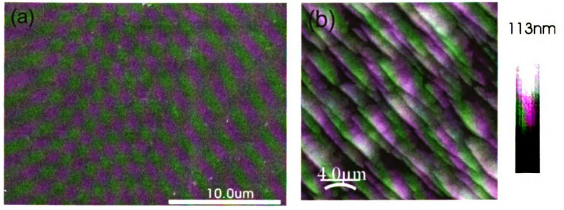

Figure 83 (a) Edge (approx. 1.5 mm from center) of the 12 hr diamond film on Ir/$SrTiO_3$. (b) Macro steps at the center of the film scanned with AFM.

AFM and SEM scans revealed that although most of the film is smooth and featureless, in some areas it had macro-steps of average height 20 nm on the surface. Similar macro-step bunching has been reported in homoepitaxial diamond growth *(162, 163)*. However, it is

unclear if this is indicative of a 2-D layer-by-layer growth mechanism.

A 48 hr film is shown in Figure 84.

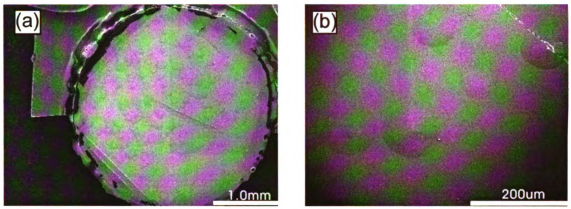

Figure 84 (a) A complete diamond film grown for 48 hrs on Ir/$SrTiO_3$. The substrate broke in half during cooling. (b) Center of the film showing a crack in the upper right-hand corner, and hillock-type defects.

Films grown for 36 or 48 hours remained intact through the cool-down period, although sometimes the substrate cracked, as shown above. The films were smooth and optically transparent. They also had denumerable defects on the surface (~100 cm^{-2}). These could be due to particulates deposited on the sample during growth, since the defects were not observed on samples grown for short times. Defects at this density can often be ascribed to particulates *(164)*. They may be similar to defects that form in homoepitaxial growth under similar methane concentrations (0.5-2%) *(163, 165)*. They should be suppressed with appropriately modified growth conditions.

An optical micrograph of a cleaved 36 hr freestanding sample is shown in Figure 85. Films grown for longer than 12 hr detached from the $SrTiO_3$ during cooling, with Ir adhering to the diamond surface. It was removed with an electrochemical etch comprising 15:10:1 $CaCl_2$:H_2O:HCl *(166)*.

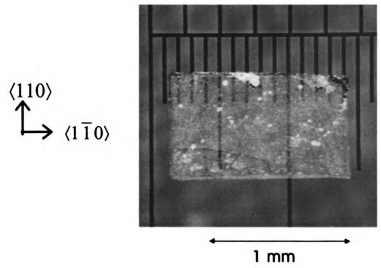

Figure 85 Optical micrograph of a single crystal slab of diamond. Cleaved from a 3 mm dia sample, it was originally about 0.01 carat.

The 25 μm thick sample cleaved along the crystal axes and was optically transparent. The surfaces are as grown. No polishing or thinning was carried out. The piece in Figure 85 is a portion of the original 3 mm sample - approximately 0.01 ct weight.

9.4.1 SEM cross-sections

The thicknesses of the 6 to 48 hr films were measured from SEM images or by optical microscope analysis of cross-sections. The thickness was measured at 3 to 4 points along a cleaved or fractured edge. The average value is reported in Table 14.

Total growth time (hours)	*Thickness (μm)*
6	3.7 ± 0.1
12	8.5 ± 0.2
36	25 ± 1
48	35 ± 1

Table 14 Cross-section thickness measured from SEM or optical micrographs.

The 6 hr film thickness measurement was taken from sample pieces closer to the edge of the film than the center, therefore this measurement is likely to be lower than average. The average growth rate is estimated at 0.7 μm/hr for these films.

9.4.1.1 Cleavage angle measurement

Single crystals cleave at angles that correspond to crystallographic planes. For diamond (001), (111) is the preferred cleavage plane. The angle between (111) and (001) planes is 54.74 deg. Shown in Figure 86 is a 25 μm diamond sample with a (111) cleavage plane.

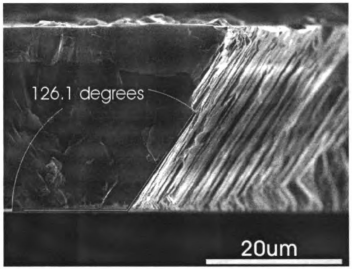

Figure 86 Cross section of 25 μm film showing cleavage angle of (111) plane. The <001> direction is normal to the top surface.

The measured clevage angle for this sample is 180-126.1 = 53.9 deg. The SEM micrograph in Figure 87 shows the cross-section (111) plane of the same diamond film.

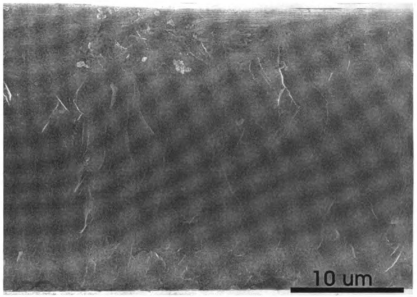

Figure 87 Fracture surface of a 25 μm diamond film revealing the (111) plane.

Although the SEM image looks unremarkable, it should be noted that columnar growth structure typical of polycrystalline diamond films is not present. Instead, horizontal "layers" are apparent, particularly near the growth surface of the diamond.

9.4.2 X-ray diffraction

X-ray rocking curves were measured for films grown from 1 to 36 hr on $Ir/SrTiO_3$. The diamond (004) linewidth as a function of the film thickness is shown in Figure 88.

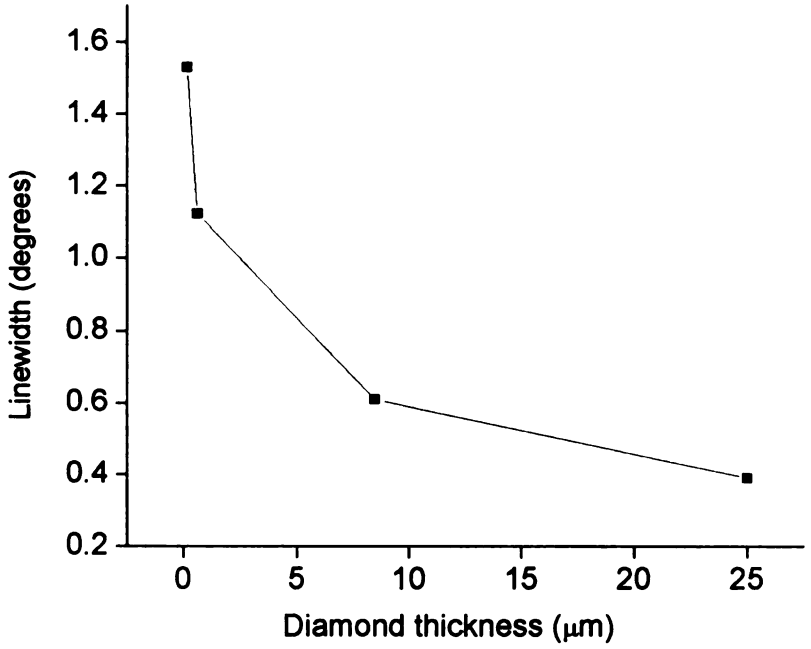

Figure 88 Thickness dependence of the X-Ray rocking curve linewidth of diamond on Ir/$SrTiO_3$.

The linewidth of the diamond (004) peak decreases, from 1.5 deg for the 173 nm thick film, to 0.34 deg for the 25 μm thick film. Schreck et al. reported similar thickness dependence of the diamond (004) linewidth on Ir/$SrTiO_3$, with a value of 0.17° for a 34 μm film *(7)*. However, it is not known whether this value was measured for a sample with the substrate side polished off.

9.4.3 Electron backscattering diffraction

We used electron backscattering diffraction (EBSD) to obtain a {111} pole figure from a 25 μm diamond sample. This was done by scanning the electron beam at 120 separate points in a 10 x 10 μm^2 area. At each point an EBSD pattern was recorded, and its coordinates indexed. The orientation at each point is represented by plotting the positions of its {111} poles in a stereographic projection, which forms the {111} pole

figure shown in Figure 89. Each point measured in the EBSD has three {111} poles, so 360 poles are plotted in the projection.

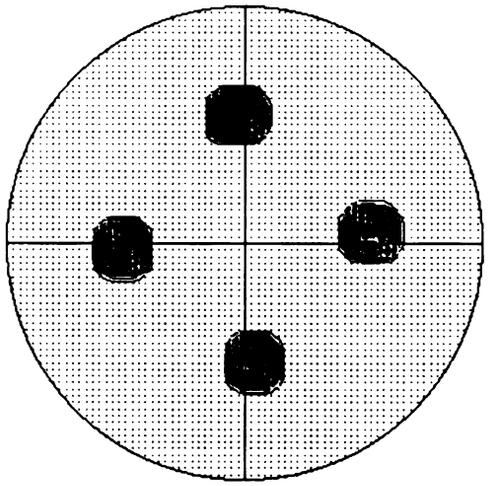

Figure 89 {111} pole figure from EBSD measurements on a 10x10um area, 120 separate points. <100> lies at the center of the projection, and the horizontal and vertical axes are along [110] directions.

If the surface had no texture, the measurements would be uniformly destributed in the projection. Instead, the measurements are clustered around the {100} poles indicating the characteristic pattern of a cubic crystal with (100), [001] texture.

9.4.4 Raman microscopy

For a 25 μm diamond film, removed from the iridium substrate, we observed the Raman spectrum in Figure 90.

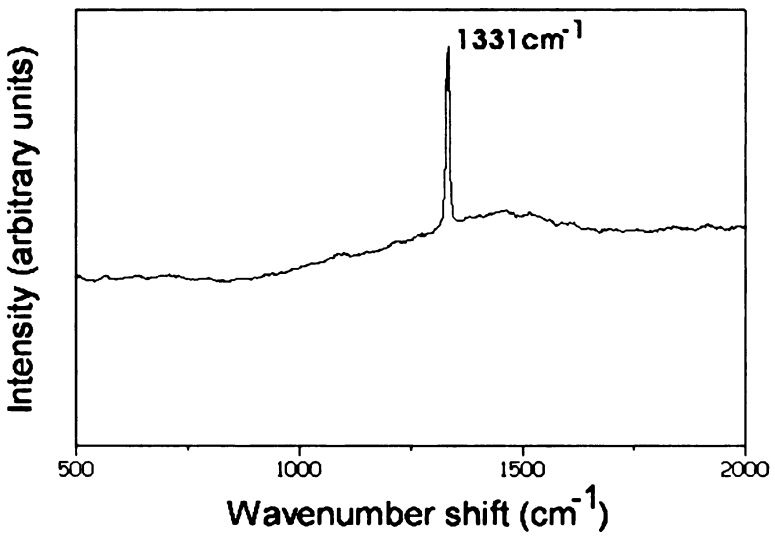

Figure 90 Raman spectrum of a 25 μm (001) diamond film on $Ir/SrTiO_3$. Linewidth is 8 cm^{-1}.

The diamond peak at 1331 cm^{-1} had a linewidth of 8 cm^{-1}. The background that leads to a shallow maximum near 1500 cm^{-1} indicates the presence of some disordered carbon *(15, 16)*. The peak shift from the expected 1332 cm^{-1} position is an indication of stress in the film. To investigate this further, we performed polarized Raman spectroscopy in the (001) backscattering configuration on a 35 μm film. We first measured a reference sample of type IIa natural diamond. It had a single peak at 1332.3 cm^{-1} with linewidth 2.1 cm^{-1} in the geometry $e_i||e_s||[110]$. The spectrum of the sample is shown in Figure 91.

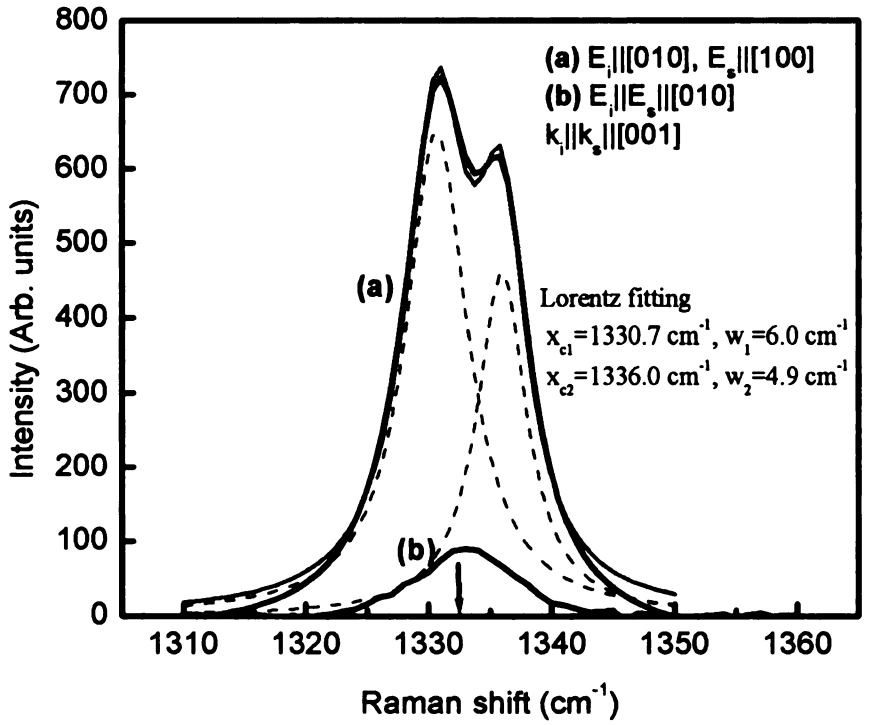

Figure 91 Polarized Raman spectra for 35 μm film. The arrow points to 1332 cm^{-1}.

The specturm obeys the Raman selection rules: for $\vec{k}_i$ and $\vec{k}_s$ parallel to <001>: the intensity of the scattered beam polarized in the <100> direction, (a), is proportional to the intensity of the incident light. The intensity polarized along <010>, (b), is due only to polarization leak, as seen also for the natural diamond. However, the Raman peak of (a) is split. Lorentz fitting shows two peaks shifted 1.6 cm^{-1} and 3.7 cm^{-1} away from 1332.3 cm^{-1}. The peak shifts are attributed to internal stresses – a compressive biaxial stress in the (001) plane and a tensile stress along the growth direction <001> *(167)*. The spectrum was measured for different focus depths through the thickness of the sample (Figure 92).

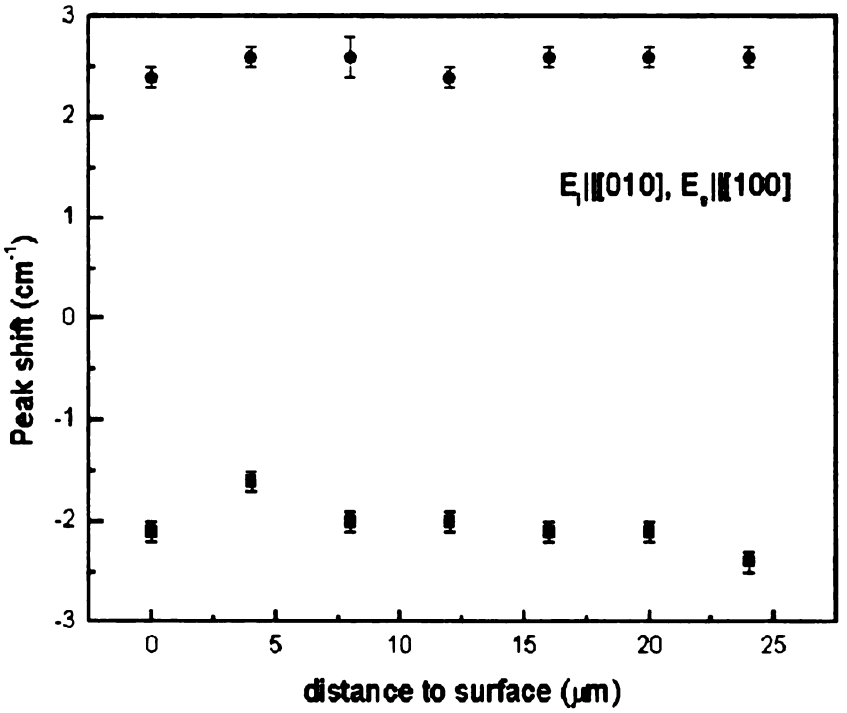

Figure 92 Depth profile of Raman peak shift for 35 μm film.

In changing the focus depth, only the intensity of the peaks changed, their positions remained the same, which indicated the stress is uniformly distributed along the <001> growth direction.

9.5 Summary

We have examined the growth evolution of diamond films on $Ir/SrTiO_3$ and Ir/Al_2O_3. The progression of coalescence for thin films was studied using 2-D Fourier transforms of SEM micrographs with interrupted growth experiments. After 20 minutes of growth, the remaining grain boundaries showed alignment predominantly along [011] directions. High nucleation densities initiated by the biasing procedure led directly to the early coalescence of crystallites on the substrate. The films show complete coalescence at $\lesssim$ 200 nm thickness. Our results may be compared to other reports that show

persistence of individual crystallites for films $\gtrsim$ 600 nm thickness. X-ray diffraction, in a {111}-ϕ scan demonstrated full epitaxial alignment of diamond, Ir and $SrTiO_3$ with the relation: $(100)_{dia}<110>_{dia}||(100)_{Ir}<110>_{Ir}||(100)_{SrTiO_3}<110>_{SrTiO_3}$.

Single crystal diamond grown heteroepitaxially on Ir/Al_2O_3 substrates was demonstrated for the first time. This is a significant advance towards realization of wafer scale diamond films, since sapphire is more widely available in large area defect-free form than $SrTiO_3$. We have also demonstrated that (111) diamond epitaxy may be possible on (111) Ir by investigating the early stages of diamond growth on this surface.

The thick diamond films are single crystals, as evidenced by cleavage, X-ray diffraction, EBSD and Raman measurements. The thickness dependence of the X-ray diffraction linewidths agrees qualitatively with an earlier study. We have shown, for the first time, heteroepitaxial diamond that obeys the Raman selection rules for single crystal diamond. The peak splitting in the Raman peak indicated the films are under internal stress. We have demonstrated a uniform film over the entire 3.5 mm diameter area exposed to the plasma.

Chapter 10 Conclusions and outlook

In the course of this research, we have demonstrated or observed a number of unique phenomena while investigating nucleation and growth of heteroepitaxial diamond. We have demonstrated that epitaxial iridium thin films provide a suitable surface for the study of diamond nucleation. Our study of the early growth of diamond just after the onset of nucleation has enabled us to develop a new model of the nucleation of heteroepitaxial diamond.

10.1 Summary of this research

The following results on the nucleation of heteroepitaxial diamond were presented:

1. The highest nucleation density reported (3.2×10^{11} cm^{-2}) for heteroepitaxial diamond growth. This number comes from an unambiguous count of particles on the surface. The evidence of particle coalescence at a very early stage suggested the actual nucleation density is more likely ~10^{12} cm^{-2}. High nucleation densities required optimization of the bias assisted procedure and geometry in a microwave plasma CVD system.
2. High-resolution SEM images showed that the diamond crystallites in an early stage of growth display a remarkably narrow distribution of sizes, indicating a synchronous onset of nucleation. Quantitative analysis using 2-D Fourier

transforms and radial distribution plots of particles after a "quenching" process revealed radial spatial correlations. This implies that there are "effective" interactions among crystals that destroy randomness.

3. The evidence of the first two points led us to outline a new model for the nucleation and early growth of diamond on Ir. The biasing process provides the necessary conditions for diamond nucleation, possibly as carbon saturation of the surface. The nucleation event, however, is a result of the quenching process with the termination of the biasing. High nucleation densities then lead directly to the early coalescence of the films.

Growth of single crystal diamond on iridium/oxide substrates was also studied in detail. The films were characterized using SEM, AFM, optical microscopy, Raman spectroscopy, X-ray diffraction and EBSD. The following aspects of the growth of heteroepitaxial diamond were presented in this work:

1. The early stages of diamond heteroepitaxial growth and coalescence. In order to observe the earliest growth stages we were required to formulate a precise procedure to ensure repeatability. We performed 2-D Fourier transform analysis on SEM micrographs taken after short growth periods. The power spectra of the transforms clearly showed the coarsening and alignment of the diamond films over relatively short growth times.
2. By growing for extended periods, to a maximum of 48 hr, diamond plates of thickness 35 μm were produced. Freestanding crystals exhibited (111) cleavage surfaces, the same as natural diamond, and were transparent in visible light. Characterization of the diamond by x-ray diffraction, electron backscattering

diffraction, and Raman scattering confirmed the existence of (001) oriented single crystal diamond. To our knowledge, these are the highest quality thick diamond films yet produced.

3. The discovery of iridium/sapphire as a new substrate for heteroepitaxial diamond growth. Our finding that a-plane sapphire can be used to grow (001) diamond promises to lead to improvements in diamond heteroepitaxy.

10.2 Suggestions for further work

Semiconducting diamond is attractive for applications of high temperature/high frequency devices because of its superior physical properties and its wide bandgap. This will require efficient n- and p- type doping. Acceptor (p-type) doping of diamond with boron leads to a level 0.38 eV above the valence band maximum, reasonable for device purposes. Donor (n-type) doping of diamond at a similar level has not yet been realized, mostly due to the strain that incorporating large atoms into the diamond lattice introduces. However, the method of nucleation presented in this thesis, may allow dopants to be introduced so that they are incorporated readily in the lattice. Electrical mobility measurements could then be carried out on heteroepitaxial grown films. Without doping, polycrystalline diamond films have already been demonstrated as nuclear particle detectors *(168-170)*. Radiation hardness and high temperature operation of such diamond devices is superior to similar silicon detectors. Unfortunately grain boundaries in polycrystalline diamond lead to carrier recombination and lower efficiency *(169)*. Single crystal diamond would remove this problem. Photo-excitation of the diamond films would allow a measurement of the lifetime of free carriers, an important parameter for photodetectors.

An obvious extension of this work would be the reduction of defect densities in the final thick films, and an understanding of their formation and origins. The defects we found in our single crystal heteroepitaxial diamond look qualitatively similar to common defects found in homoepitaxial diamond. This suggests that the growth of the diamond after a certain thickness proceeds identically to diamond grown on diamond. Related to this issue is the scalability of the sample size. We suspect that scaling the entire process will involve careful consideration of the secondary plasma during biasing. Optical spectroscopy of the secondary plasma during bias may provide some clues to understanding the specific roles that biasing accomplishes. Study of the secondary plasma and the scaling may indirectly lead to a better understanding of the nucleation mechanism.

Finally, the peak splitting of the polarized Raman spectra remains to be studied and understood. It is clear that the peak splitting must be related to the stress in the films, but such peak splitting has not been observed before in single crystal diamond films.

References

1. S. Wolter, B. Stoner, J. G. P. Ellis, *et al.*, *Textured growth of diamond on silicon via in situ carburization and bias-enhanced nucleation*, Appl. Phys. Lett. **62,** 1215 (1993).

2. X. Jiang and C.-P. Klages, *Heteroepitaxial Diamond Growth On (100) Silicon*, Diam. Relat. Mat. **2,** 1112 (1993).

3. C. Wild, R. Kohl, N. Herres, *et al.*, *Oriented CVD Diamond Films - Twin Formation, Structure and Morphology*, Diam. Relat. Mat. **3,** 373 (1994).

4. K. Ohtsuka, H. Fukuda, K. Suzuki, *et al.*, *Fabrication of epitaxial Diamond Thin Film on Iridium*, Jpn. J. Appl. Phys. Pt. 2 **36,** L1214 (1997).

5. K. Ohtsuka, K. Suzuki, A. Sawabe, *et al.*, *Epitaxial growth of diamond on Iridium*, Jpn. J. Appl. Phys. Pt. 2 **35,** L1072 (1996).

6. T. Tsubota, M. Ohta, K. Kusakabe, *et al.*, *Heteroepitaxial growth of diamond on an iridium (100) substrate using microwave plasma-assisted chemical vapor deposition*, Diam. Relat. Mat. **9,** 1380 (2000).

7. M. Schreck, F. Hormann, H. Roll, *et al.*, *Diamond nucleation on iridium buffer layers and subsequent textured growth: A route for the realization of single-crystal diamond films*, Appl. Phys. Lett. **78,** 192 (2001).

8. M. Schreck, H. Roll and B. Stritzker, *Diamond/Ir/$SrTiO_3$: A material combination for improved heteroepitaxial diamond films*, Appl. Phys. Lett. **74,** 650 (1999).

9. S. Yugo, T. Kanai, T. Kimura, *et al.*, *Generation of diamond nuclei by electric field in plasma chemical vapor depostion*, Appl. Phys. Lett. **58,** 1036 (1991).

10. W. Massa, *Crystal Structure Determination* (Springer-Verlag, Berlin, 2000).

11. B. B. Pate, in *Diamond: Electronic Properties and Applications* L. S. Pan and D. R. Kania, Eds. (Kluwer Academic Publishers, Boston/Dordrecht/London, 1996).

12. L. Reimer, *Scanning Electron Microscopy*. J. Enoch, *et al.*, Eds., Springer Series in Optical Sciences (Springer-Verlag, Berlin, 1985).

13. S. Flegler, J. Heckman and K. Klomparens, *Scanning and Transmission Electron*

Microscopy: An Introduction (W.H. Freeman and Company, New York, 1993).

14. B. D. Cullity, *Elements of X-ray Diffraction*. M. Cohen, Ed., Addison-Wesley Metallurgy Series (Addison-Wesley Publishing Co, Inc, Reading, MA, 1956).

15. D. S. Knight and W. B. White, *Characterization of Diamond Films By Raman-Spectroscopy*, J. Mater. Res. **4,** 385 (1989).

16. J. R. Dennison, M. Holtz and G. Swain, *Raman spectroscopy of carbon materials*, Spectroscopy **11,** 38 (1996).

17. R. J. Nemanich, J. T. Glass, G. Lucovsky, *et al.*, *Raman-Scattering Characterization of Carbon Bonding in Diamond and Diamondlike Thin-Films*, J. Vac. Sci. Technol. A-Vac. Surf. Films **6,** 1783 (1988).

18. M. C. Tobin, *Laser Raman Spectroscopy*. P. J. Elving and I. M. Kolthoff, Eds., Chemical Analysis (Wiley-Interscience, New York, 1971), vol. 35.

19. M. Cardona, in *Light Scattering in Solids II* M. Cardona and G. Güntherodt, Eds. (Springer-Verlag, Berlin, 1982), vol. 50, p. 19.

20. S. A. Solin and A. K. Ramdas, *Raman Spectrum of Diamond*, Phys. Rev. B **1,** 1687 (1970).

21. R. S. Krishnan, paper presented at the Proc Indian Acad Sci Sect A 1946.

22. M. A. Washington and H. Z. Cummins, *Linewidth of the sharp two-phonon peak in diamond*, Phys. Rev. B **15,** 5840 (1977).

23. C. B. Prater, P. G. Maivald, K. J. Kjoller, *et al.*, "Tapping Mode Imaging: Applications and Technology" *Tech. Report No. AN04* (Digital Instruments, http://www.di.com).

24. E. Bauer, Z. Kristallogr. **110,** 372 (1958).

25. J. A. Venables, *Introduction to Surface and Thin Film Processes* (Cambridge University Press, Cambridge, 2000).

26. J. E. Field, in *The Properties of Natural and Synthetic Diamond* J. E. Field, Ed. (Academic Press, London, 1992) p. 667.

27. A. Sawabe and H. Fukuda, *Heteroepitaxial growth of diamond*, Elec. & Comm.

Japan Pt 2 **81,** 162 (1998).

28. J. C. Angus and C. C. Hayman, *Low-Pressure, Metastable Growth of Diamond and Diamondlike Phases*, Low-Pressure, Metastable Growth of Diamond and Diamondlike Phases **241,** 913 (1988).

29. P. May, *CVD Diamond - a new technology for the future?*, Endeavor Mag. **19,** 101 (1995).

30. B. Spitzyn, L. Bouilov and B. Derjaguin, *Vapor growth of diamond on diamond and other surfaces*, J. Cryst. Growth **52,** 219 (1981).

31. A. Sherman, *Chemical Vapor Deposition for Microelectronics; Principles Technology, and Applications*. R. F. Bunshah and G. E. McGuire, Eds., Materials Science and Process Technology Series (Noyes Publications, Park Ridge, NJ, 1987).

32. B. Lux and R. Haubner, in *Diamond and diamond-like films and coatings* R. E. e. a. Clausing, Ed. (Plenum Press, New York, 1991) p. 579.

33. L. S. G. Plano, in *Diamond: Electronic Properties and Applications* L. S. Pan and D. R. Kania, Eds. (Kluwer Academic Publishers, Boston/Dordrecht/London, 1996).

34. P. K. Bachmann, G. Gärtner and H. Lydtin, *Plasma-assisted Chemical Vapor Deposition Processes*, MRS Bull. **13,** 51 (1988).

35. W. G. Eversole, US Patent No. 3030187, 3030188 (1962).

36. D. J. Poferl, N. C. Gardner and J. C. Angus, *Growth of Boron-Doped Diamond Seed Crystals by Vapor-Deposition*, J. Appl. Phys. **44,** 1428 (1973).

37. J. C. Angus, H. A. Will and W. S. Stanko, *Growth of Diamond Seed Crystals by Vapor Deposition*, J. Appl. Phys. **39,** 2915 (1968).

38. M. Kamo, Y. Sato, S. Matsumoto, *et al.*, *Diamond Synthesis from Gas-Phase in Microwave Plasma*, J. Cryst. Growth **62,** 642 (1983).

39. S. Matsumoto, Y. Sato, M. Tsutsumi, *et al.*, *Growth of Diamond Particles from Methane-Hydrogen Gas*, J. Mater. Sci. **17,** 3106 (1982).

40. S. Matsumoto, Y. Sato, M. Kamo, *et al.*, *Vapor-Deposition of Diamond Particles from Methane*, Jpn. J. Appl. Phys. Part 2 - Lett. **21,** L183 (1982).

41. N. Ohtake and M. Yoshikawa, *Effects of Oxygen Addition on Growth of Diamond Film by Arc- Discharge Plasma-Jet Chemical-Vapor-Deposition*, Jpn. J. App. Phys. Pt. 1 **32,** 2067 (1993).

42. S. Matsumoto, Y. Manabe and Y. Hibino, *Diamond Deposition Using an X-Y Stage in a Dc Plasma-Jet Chemical Vapor-Deposition*, J. Mater. Sci. **27,** 5905 (1992).

43. S. Matsumoto, M. Hino and T. Kobayashi, *Synthesis of Diamond Films in a Rf Induction Thermal Plasma*, Appl. Phys. Lett. **51,** 737 (1987).

44. H. V. Boenig, *Plasma Science and Technology* (Cornell University Press, London, 1982).

45. M. A. Lieberman and A. J. Lichtenberg, *Principles of Plasma Discharges and Materials Processing* (John Wiley & Sons, Inc., New York, 1994).

46. W. Kalss, R. Haubner and B. Lux, *Diamond deposition on noble metals*, Diam. Relat. Mat. **6,** 240 (1997).

47. T. Suzuki and A. Argoitia, *Current status of heteroepitaxy of CVD diamond*, Phys. Status Solidi A **154,** 239 (1996).

48. S. T. Lee, Z. D. Lin and X. Jiang, *CVD diamond films: nucleation and growth*, Mater. Sci. Eng. R-Rep. **25,** 123 (1999).

49. S. Koizumi, T. Murakami, T. Inuzuka, *et al.*, *Epitaxial-Growth of Diamond Thin-Films On Cubic Boron Nitride(111) Surfaces By DC Plasma Chemical Vapor-Deposition*, Appl. Phys. Lett. **57,** 563 (1990).

50. M. Yoshikawa, H. Ishida, A. Ishitani, *et al.*, *Study of Crystallographic Orientations in the Diamond Film On Cubic Boron-Nitride Using Raman Microprobe*, Appl. Phys. Lett. **57,** 428 (1990).

51. T. Inuzuka, S. Koizumi and K. Suzuki, *Epitaxial growth of diamond thin films on foreign substrates*, Diam. Relat. Mat. **1,** 175 (1992).

52. P. C. Yang, C. A. Wolden, W. Liu, *et al.*, *Coalesced oriented diamond films on nickel*, J. Mater. Res. **13,** 1120 (1998).

53. Z. Sitar, W. Liu, P. C. Yang, *et al.*, *Heteroepitaxial nucleation of diamond on nickel*, Diam. Relat. Mat. **7,** 276 (1998).

54. T. Tachibana, Y. Yokota, K. Nishimura, *et al.*, *Heteroepitaxial diamond growth on*

platinum(111) by the Shintani process, Diam. Relat. Mat. **5,** 197 (1996).

55. X. Jiang, K. Schiffmann, C. P. Klages, *et al.*, *Coalescence and overgrowth of diamond grains for improved heteroepitaxy on silicon(001)*, J. Appl. Phys. **83,** 2511 (1998).

56. H. Kawarada, T. Suesada and H. Nagasawa, *Heteroepitaxial Growth of Smooth and Continuous Diamond Thin Films On Silicon Substrates Via High-Quality Silicon-Carbide Buffer Layers*, Appl. Phys. Lett. **66,** 583 (1995).

57. H. Kawarada, C. Wild, N. Herres, *et al.*, *Heteroepitaxial growth of highly oriented diamond on cubic silicon carbide*, J. Appl. Phys. **81,** 3490 (1997).

58. Y. Yokota, T. Tachibana, K. Miyata, *et al.*, *Heteroepitaxial diamond growth on platinum(111) by Shintani process*, Diam. Films Technol. **6,** 165 (1996).

59. T. Tachibana, Y. Yokota, K. Kobashi, *et al.*, *Heteroepitaxial growth of {111}-oriented diamond films on platinum {111}/sapphire{0001} substrates*, J. Cryst. Growth **205,** 163 (1999).

60. M. Schreck, H. Roll, J. Michler, *et al.*, *Stress distribution in thin heteroepitaxial diamond films on Ir/$SrTiO_3$ studied by x-ray diffraction, Raman spectroscopy, and finite element simulations*, J. Appl. Phys. **88,** 2456 (2000).

61. R. O. Jones and O. Gunnarsson, *The density functional formalism, its applications and prospects*, Rev. Mod. Phys. **61,** 689 (1989).

62. S. Koizumi, *Heteroepitaxy of diamond on cubic boron nitride*, Isr. J. Chem. **38,** 33 (1998).

63. W. Yarbrough and R. Messier, *Current Issues and Problems in the chemical vapor deposition of diamond*, Science **247,** 688 (1990).

64. T. Taniguchi and S. Yamaoka, *Spontaneous nucleation of cubic boron nitride single crystal by temperature gradient method under high pressure*, J. Cryst. Growth **222,** 549 (2001).

65. P. C. Yang, R. Schlesser, C. A. Wolden, *et al.*, *Control of diamond heteroepitaxy on nickel by optical reflectance*, Appl. Phys. Lett. **70,** 2960 (1997).

66. Y. Shintani, *Growth of highly (111)-oriented, highly coalesced diamond films on platinum(111) surface: A possibility of heteroepitaxy*, J. Mater. Res. **11,** 2955 (1996).

67. T. Tachibana, Y. Yokota, K. Miyata, *et al.*, *Diamond films heteroepitaxially grown on platinum (111)*, Phys. Rev. B **56,** 15967 (1997).

68. H. Nagasawa, Y. Yamaguchi, T. Izumi, *et al.*, *Heteroepitaxial growth and ESR evaluation of 3C-SiC*, Appl. Surf. Sci. **70/71,** 542 (1993).

69. M. Hansen, *Constitution of Binary Alloys*. R. Mehl, Ed., Metallurgy and Metallurgical Engineering Series (McGraw-Hill Book Co., New York, Toronto, London, ed. Second, 1958).

70. C. Bednarski, Z. Dai, A.-P. Li, *et al.*, *Studies of Heteroepitaxial Growth of Diamond* paper presented at the 13th European Conference on Diamond, Diamond-like Materials, Carbon Nanotubes, Nitrides and Silicon Carbide, Granada, Spain 2002.

71. K. Suzuki, H. Fukuda, T. Yamada, *et al.*, *Epitaxially grown free-standing diamond platelet*, Diam. Relat. Mat. **10,** 2153 (2001).

72. K. Suzuki, H. Fukuda and A. Sawabe, *Epitaxial growth of diamond thin films on iridium surfaces* paper presented at the The 5th NIRIM International Symposium on Advanced Materials (ISAM '98), Tsukuba, Japan 1998.

73. T. Saito, S. Tsuruga, N. Ohya, *et al.*, *Epitaxial nucleation of diamond on iridium substrate by bias treatment, for microwave plasma-assisted chemical vapor deposition*, Diam. Relat. Mat. **7,** 1381 (1998).

74. F. Hörmann, M. Schreck and B. Stritzker, *First stages of diamond nucleation on iridium buffer layers*, Diam. Relat. Mat. **10,** 1617 (2001).

75. Z. Dai, A.-P. Li, C. Bednarski, *et al.*, *Epitaxial Iridium Growth on Strontium Titanate*, Mater. Res. Soc. Symp. Proc. **648,** 11.35.1 (2001).

76. M. Schreck and B. Stritzker, *Nucleation and growth of heteroepitaxial diamond films on silicon*, Phys. Status Solidi A **154,** 197 (1996).

77. P. A. Dennig and D. A. Stevenson, *Influence of Substrate Topography On the Nucleation of Diamond Thin-Films*, Appl. Phys. Lett. **59,** 1562 (1991).

78. P. Karve, S. R. Sainkar and S. T. Kshirsagar, *Role of surface features in CVD diamond nucleation on surface- pretreated substrates*, Mater. Lett. **34,** 387 (1998).

79. B. Stoner and J. Glass, *Textured diamond growth on (100) β-SiC via microwave plasma chemical vapor deposition*, Appl. Phys. Lett. **60,** 698 (1992).

80. X. Jiang, C. P. Klages, Z. R., *et al.*, *Epitaxial Diamond Thin-Films On (001) Silicon Substrates*, Appl. Phys. Lett. **62,** 3438 (1993).

81. Y. Ma, T. Tsurumi, N. Shinoda, *et al.*, *Effect of bias enhanced nucleation on the nucleation density of diamond in microwave plasma CVD*, Diam. Relat. Mat. **4,** 1325 (1995).

82. M. Katoh, M. Aoki and H. Kawarada, *Plasma-Enhanced Diamond Nucleation on Si*, Jpn. J. Appl. Phys. Part 2 - Lett. **33,** L194 (1994).

83. M. J. Chiang and M. H. Hon, *Enhanced nucleation of diamond films assisted by positive dc bias*, Thin Solid Films **389,** 68 (2001).

84. R. I. Cherry and T. Whitmore, *Experimental Apparatus for Determining Charge-Exchange between Hydrogen and Hydrocarbon Groups in the Hot-Filament Deposition of Diamond*, Appl. Phys. Lett. **67,** 3040 (1995).

85. Q. Chen and Z. Lin, *Experimental approach to the mechanism of the negative bias enhanced nucleation of diamond on Si via hot filament chemical vapor deposition*, J. Appl. Phys. **80,** 797 (1996).

86. K. Perng, K. S. Liu and I. N. Lin, *Evidence of electron-emission-enhanced nucleation of diamonds in microwave plasma-enhanced chemical vapor deposition*, Appl. Phys. Lett. **79,** 3257 (2001).

87. A. Flöter, G. Schaarschmidt, B. Mainz, *et al.*, *Deposition of Diamond on Patterned Silicon Substrates*, Diam. Relat. Mat. **4,** 930 (1995).

88. X. Jiang, *Effects of ion bombardment on the nucleation and growth of diamond films*, Phys. Rev. B **58,** 7064 (1998).

89. M. Y. Liao, F. G. Qin, J. H. Zhang, *et al.*, *Ion bombardment as the initial stage of diamond film growth*, J. Appl. Phys. **89,** 1983 (2001).

90. J. Yang, X. W. Su, Q. J. Chen, *et al.*, *Si+ Implantation - a Pretreatment Method For Diamond Nucleation On a Si Wafer*, Appl. Phys. Lett. **66,** 3284 (1995).

91. J. Robertson, J. Gerber, S. Sattel, *et al.*, *Mechanism of bias-enhanced nucleation of diamond on Si*, Appl. Phys. Lett. **66,** 3287 (1995).

92. J. Gerber, S. Sattel, H. Ehrhardt, *et al.*, *Investigation of bias enhanced nucleation of diamond on silicon*, J. Appl. Phys. **79,** 4388 (1996).

93. M. Y. Liao, X. M. Meng, X. T. Zhou, *et al.*, *Nanodiamond formation by hot-filament chemical vapor deposition on carbon ions bombarded Si*, J. Cryst. Growth **236,** 85 (2002).

94. Y. Lifshitz, S. R. Kasi and J. W. Rabalais, *Subplantation model for film growth from hyperthermal species: Application to diamond*, Phys. Rev. Lett. **62,** 1290 (1989).

95. S. Uhlmann, T. Frauenheim and Y. Lifshitz, *Molecular-dynamics study of the fundamental processes involved in subplantation of diamondlike carbon*, Phys. Rev. Lett. **81,** 641 (1998).

96. J. Robertson, *The Deposition Mechanism of Diamond-Like a-C and a-C-H*, Diam. Relat. Mat. **3,** 361 (1994).

97. J. Robertson, *Deposition Mechanisms for Promoting Sp(3) Bonding in Diamond-Like Carbon*, Diam. Relat. Mat. **2,** 984 (1993).

98. H. P. Kaukonen and R. M. Nieminen, *Molecular-Dynamics Simulation of the Growth of Diamond-Like Films by Energetic Carbon-Atom Beams*, Phys. Rev. Lett. **68,** 620 (1992).

99. S. Kátai, Z. Tass, G. Hars, *et al.*, *Measurement of ion energy distributions in the bias enhanced nucleation of chemical vapor deposited diamond*, J. Appl. Phys. **86,** 5549 (1999).

100. S. Kátai, A. Kovats, I. Maros, *et al.*, *Ion energy distributions and their evolution during bias- enhanced nucleation of chemical vapor deposition of diamond*, Diam. Relat. Mat. **9,** 317 (2000).

101. Y. Kim and J. Lee, *Formation of highly oriented diamond film on (100) silicon*, Formation of highly oriented diamond film on (100) silicon **81,** 3660 (1997).

102. Y. Kim, Y. Han and J. Lee, *The effects of a negative bias on the nucleation of oriented diamond on Si*, Diam. Rel. Mater. **7,** 96 (1998).

103. S. P. McGinnis, M. A. Kelly, S. B. Hagstrom, *et al.*, *Observation of diamond nanocrystals in carbon films deposited during ion-assisted microwave plasma nucleation pretreatments*, J. Appl. Phys. **79,** 170 (1996).

104. L. Hanley and S. B. Sinnott, *The growth and modification of materials via ion-surface processing*, Surf. Sci. **500,** 500 (2002).

105. S. McGinnis, M. Kelly and S. Hagstroem, *Evidence of an energetic ion*

bombardment mechanism for bias enhanced nucleation of diamond, Appl. Phys. Lett. **66,** 3117 (1995).

106. B. Sheldon, R. Csencsits, J. Rankin, *et al.*, *Bias-enhanced nucleation of diamond during microwave-assisted chemical vapor deposition*, J Appl. Phys. **75,** 5001 (1994).

107. Y. Shigesato, R. E. Boekenhauer and B. W. Sheldon, *Emission-Spectroscopy During Direct-Current-Biased, Microwave- Plasma Chemical-Vapor-Deposition of Diamond*, Appl. Phys. Lett. **63,** 314 (1993).

108. J. C. Angus, H. A. Will and W. S. Stranko, J. Appl. Phys. **39,** 2915 (1968).

109. N. Setaka, *Diamond Synthesis from Vapor-Phase and Its Growth-Process*, J. Mater. Res. **4,** 664 (1989).

110. J. C. Angus, A. Argoitia, R. Gat, *et al.*, *Chemical Vapor-Deposition of Diamond*, Philos. Trans. R. Soc. Lond. Ser. A-Math. Phys. Eng. Sci. **342,** 195 (1993).

111. X. Jiang, K. Schiffmann and C. Klages, *Nucleation and initial growth phase of diamond thin films on (100) silicon*, Phys. Rev. B **50,** 8402 (1994).

112. P. Ascarelli, E. Cappelli and F. Pinzari, *Nearest-neighbor distance distribution of diamond nuclei on substrate surfaces*, Appl. Phys. Lett. **70,** 1697 (1997).

113. K. Perng, K. S. Liu and I. N. Lin, *Study on Bias-Enhanced Nucleation of Diamonds by Simulating the Time Dependence of Bias Current*, J. Appl. Phys. **91,** 3934 (2002).

114. B. Stoner, G. Ma, S. Wolter, *et al.*, *Characterization of bias-enhanced nucleation of diamond on silicon by the in vacuo surface analysis and transmission electron microscopy*, Phys. Rev. B **45,** 11067 (1992).

115. T. Suesada, N. Nakamura, H. Nagasawa, *et al.*, *Initial Growth of Heteroepitaxial Diamond on Si(001) Substrates Via β-SiC Buffer Layer*, Jpn. J. Appl. Phys. Pt. 1 **34,** 4898 (1995).

116. E. Maillard-Schaller, O. M. Kuttel, P. Groning, *et al.*, *Local heteroepitaxy of diamond on silicon (100): A study of the interface structure*, Phys. Rev. B **55,** 15895 (1997).

117. M. Stammler, R. Stockel, L. Ley, *et al.*, *Diamond nucleation on silicon during bias treatment in chemical vapour deposition as analysed by electron microscopy*,

Diam. Relat. Mat. **6,** 747 (1997).

118. R. Stöckel, M. Stammler, K. Janischowsky, *et al.*, *Diamond Nucleation under Bias Conditions*, J. Appl. Phys. **83,** 531 (1998).

119. R. Stöckel, K. Janischowsky, S. Rohmfeld, *et al.*, *Growth of diamond on silicon during the bias pretreatment in chemical vapor deposition of polycrystalline diamond films*, J. Appl. Phys. **79,** 768 (1996).

120. R. Stöckel, K. Janischowsky, S. Rohmfeld, *et al.*, *Diamond growth during bias pretreatment in the microwave CVD of diamond*, Diam. Relat. Mat. **5,** 321 (1996).

121. B. R. Stoner, G. H. Ma, S. D. Wolter, *et al.*, *Epitaxial Nucleation of Diamond On β-SiC Via Bias-Enhanced Microwave Plasma Chemical-Vapor-Deposition*, Diam. Relat. Mat. **2,** 142 (1993).

122. W. L. Wang, G. Sanchez, M. C. Polo, *et al.*, *Nucleation and initial growth of diamond by biased hot filament chemical vapour deposition*, Appl. Phys. A. **65,** 241 (1997).

123. W. L. Wang, K. J. Liao, J. Wang, *et al.*, *Mechanism of diamond nucleation enhancement by electron emission via hot filament chemical vapor deposition*, Diam. Relat. Mat. **8,** 123 (1999).

124. G. Sanchez, W. L. Wang, M. C. Polo, *et al.*, *Nucleation of diamond on silicon by biased HFCVD: a comparative study*, Diam. Relat. Mat. **7,** 200 (1998).

125. M. Schreck, T. Bauer and B. Stritzker, *Optical characterization of the cathode plasma sheath during the biasing step for diamond nucleation on silicon*, Diam. Relat. Mat. **4,** 553 (1995).

126. W. Kulisch, L. Ackermann and B. Sobisch, *On the mechanisms of bias enhanced nucleation of diamond*, Phys. Status Solidi A **154,** 155 (1996).

127. D. K. Milne, P. G. Roberts, P. John, *et al.*, *Epitaxy of Diamond on Silicon*, Diam. Relat. Mat. **4,** 394 (1995).

128. R. Beckmann, B. Sobisch, W. Kulisch, *et al.*, *Investigation of the Bias Nucleation Process in Microwave Plasma-Enhanced Chemical-Vapor-Deposition of Diamond*, Diam. Relat. Mat. **3,** 555 (1994).

129. M. Whitfield, R. Jackman and J. Foord, *Spatially resolved optical emission spectroscopy of the secondary glow observed during biasing of a microwave*

plasma, Vacuum **56,** 15 (2000).

130. M. D. Whitfield, J. S. Foord, J. A. Savage, *et al.*, *Characterisation of the secondary glow region of a biased microwave plasma by optical emission spectroscopy*, Diam. Relat. Mat. **9,** 305 (2000).

131. S. Barrat, S. Saada, I. Dieguez, *et al.*, *Diamond deposition by chemical vapor deposition process: Study of the bias enhanced nucleation step*, J. Appl. Phys. **84,** 1870 (1998).

132. K. H. Thürer, M. Schreck and B. Stritzker, *Limiting processes for diamond epitaxial alignment on silicon*, Phys. Rev. B **57,** 15454 (1998).

133. F. Hörmann, H. Roll, M. Schreck, *et al.*, *Epitaxial Ir layers on $SrTiO_3$ as substrates for diamond nucleation: deposition of the films and modification in the CVD environment*, Diam. Relat. Mat. **9,** 256 (2000).

134. F. Hörmann, H. Y. Peng, T. Bauer, *et al.*, *Flat epitaxial diamond/Ir(001) interface visualized by high resolution transmission electron microscopy*, Surf. Sci. **513,** 525 (2002).

135. A. Sawabe, H. Fukuda, T. Suzuki, *et al.*, *Interface between CVD diamond and iridium films*, Surf. Sci. **467,** L845 (2000).

136. H. L. Shriver and N. M. Rosengaard, *Surface energy and work function of elemental metals*, Phys. Rev. B **46,** 7157 (1992).

137. R. Vargas, T. Goto, W. Zhang, *et al.*, *Epitaxial-Growth of Iridium and Platinum Films On Sapphire By Metalorganic Chemical-Vapor-Deposition*, Appl. Phys. Lett. **65,** 1094 (1994).

138. Y. M. Sun, J. P. Endle, K. Smith, *et al.*, *Iridium film growth with iridium tris-acetylacetonate: oxygen and substrate effects*, Thin Solid Films **346,** 100 (1999).

139. S. K. Dey, J. Goswami, C. G. Wang, *et al.*, *Preparation of iridium films by liquid source metalorganic chemical vapor deposition*, Jpn. J. Appl. Phys. Part 2 - Lett. **38,** L1052 (1999).

140. M. A. El Khakani, M. Chaker and B. Le Drogoff, *Iridium thin films deposited by radio-frequency magnetron sputtering*, J. Vac. Sci. Technol. A-Vac. Surf. Films **16,** 885 (1998).

141. M. A. El Khakani, B. Le Drogoff and M. Chaker, *Effect of the deposition*

temperature on the properties of iridium thin films grown by means of pulsed laser deposition, J. Mater. Res. **14,** 3241 (1999).

142. B. Le Drogoff, M. A. El Khakani, P. R. M. Silva, *et al.*, *Surface properties of pulsed laser deposited Ir, Rh, and $Ir_{0.9}Rh_{0.1}$ thin films for use as microelectrode arrays in electroanalytical heavy metal trace sensors*, Appl. Surf. Sci. **152,** 77 (1999).

143. J. Heiderg, R. Daghighi-Ruhi, H. V. Weyssenhoff, *et al.*, *Laser-stimulated Noble Metal Deposition from Gaseous and Condensed Acetylacetonates*, Mater. Res. Soc. Symp. Proc. **101,** 221 (1998).

144. M. Kawasaki, A. Ohtomo, T. Arakane, *et al.*, *Atomic control of $SrTiO_3$ surface for perfect epitaxy of perovskite oxides*, Appl. Surf. Sci. **107,** 102 (1996).

145. G. Koster, B. L. Kropman, G. Rijnders, *et al.*, *Quasi-ideal strontium titanate crystal surfaces through formation of strontium hydroxide*, Appl. Phys. Lett. **73,** 2920 (1998).

146. M. L. Kronberg, Acta Metall. **5,** 507 (1957).

147. D. Doppalapudi, E. Iliopoulos, S. N. Basu, *et al.*, *Epitaxial growth of gallium nitride thin films on A-plane sapphire by molecular beam epitaxy*, J. Appl. Phys. **85,** 3582 (1999).

148. J. Bai, T. Wang, H. D. Li, *et al.*, *(0001) oriented GaN epilayer grown on (11-20) sapphire by MOCVD*, J. Cryst. Growth **231,** 41 (2001).

149. Y. Kim, K. Lee and J. Lee, *Deposition of heteroepitaxial diamond film on (100) silicon in the dense plasma*, Appl. Phys. Lett. **68,** 756 (1996).

150. X. Jiang and C. P. Klages, *Recent developments in heteroepitaxial nucleation and growth of diamond on silicon*, Phys. Status Solidi A **154,** 175 (1996).

151. S. Wolter, T. Borst, A. Vescan, *et al.*, *The nucleation of highly oriented diamond on silicon via an alternating current substrate bias*, Appl. Phys. Lett. **68,** 3558 (1996).

152. K. P. Kuo and J. Asmussen, *An experimental study of high pressure synthesis of diamond films using a microwave cavity plasma reactor*, Diam. Relat. Mat. **6,** 1097 (1997).

153. W. Rasband, Image/J, ver '*1.28*', National Institutes of Health, (available for

download at http://rsb.info.nih.gov/ij)

154. D. H. Trevena, *The Liquid Phase*. N. Mott and G. R. Noakes, Eds., Wykeham Science Series (Wykeham Publications Ltd., London, 1975).

155. J. P. Hansen and I. R. McDonald, *Theory of Simple Liquids* (Academic Press, London, ed. 2nd, 1986).

156. G. H. A. Cole, *An Introduction to the Statistical Theory of Classical Simple Dense Fluids* (Pergamon Press, Oxford, 1967).

157. C. Ratsch, A. Zangwill, P. Šmilauer, *et al.*, *Saturation and Scaling of Epitaxial Island Densities*, Phys. Rev. Lett. **72,** 3194 (1994).

158. C. Pearson, M. Krueger and E. Ganz, *Direct Tests of Microscopic Growth Models using Hot Scanning Tunneling Microscopy Movies*, Phys. Rev. Lett. **76,** 2306 (1996).

159. J. A. Stroscio and D. T. Pierce, *Scaling of diffussion-mediated island growth in iron-on-iron homoepitaxy*, Phys. Rev. B **49,** 8522 (1994).

160. G. S. Bales and D. C. Chrzan, *Dynamics of Irreversible Island Growth during Submonolayer Epitaxy*, Phys. Rev. B **50,** 6057 (1994).

161. B. Voigtländer, T. Weber, P. Šmilauer, *et al.*, *Transition from Island Growth to Step-Flow Growth for Si/Si(100) Epitaxy*, Phys. Rev. Lett. **78,** 2164 (1997).

162. K. Hayashi, S. Yamanaka, H. Okushi, *et al.*, *Homoepitaxial diamond films with large terraces*, Appl. Phys. Lett. **68,** 1220 (1996).

163. K. Hayashi, S. Yamanaka, H. Watanabe, *et al.*, *Diamond films epitaxially grown by step-flow mode*, J. Cryst. Growth **183,** 338 (1998).

164. R. Hull and J. C. Bean, in *Strained-Layer Superlattices: Materials Science and Technology* T. P. Pearsall, Ed. (Academic Press, Inc., Boston, 1991), vol. 33, p. 1.

165. H. Watanabe, D. Takeuchi, S. Yamanaka, *et al.*, *Homoepitaxial diamond film with an atomically flat surface over a large area*, Diam. Relat. Mat. **8,** 1272 (1999).

166. J. Lindahl, T. Takanen and L. Montelius, *Easy and reproducible method for making sharp tips of Pt/Ir*, J. Vac. Sci. Technol. B **16,** 3077 (1998).

167. A.-P. Li, Unpublished.

168. L. S. Pan, S. Han, D. R. Kania, *et al.*, *Particle - and photoinduced conductivity in type-IIa diamonds*, J. Appl. Phys. **74,** 1086 (1993).

169. M. A. Plano, S. Zhao, C. F. Gardinier, *et al.*, *Thickness Dependence of the Electrical Characteristics of Chemical-Vapor-Deposited Diamond Films*, Appl. Phys. Lett. **64,** 193 (1994).

170. M. Marinelli, E. Milani, A. Paoletti, *et al.*, *High-quality diamond grown by chemical-vapor deposition: Improved collection efficiency in alpha-particle detection*, Appl. Phys. Lett. **75,** 3216 (1999).